UNIVERSITY OF TURKU

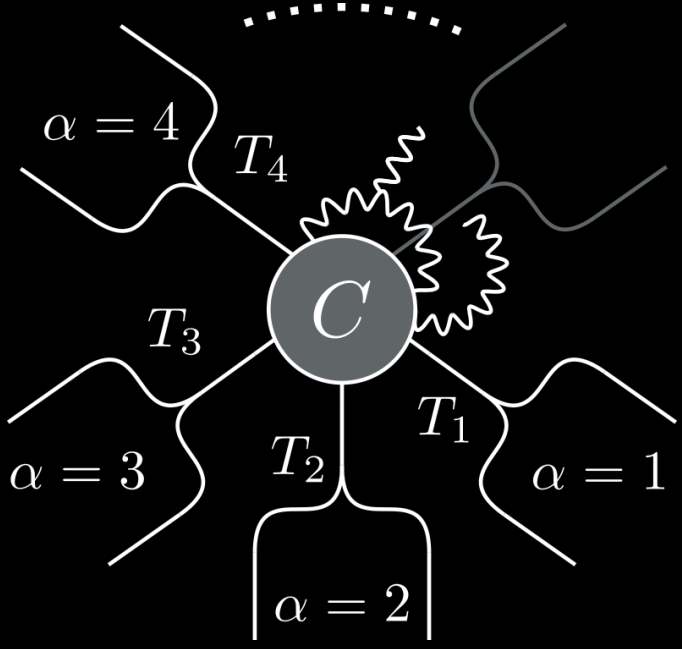

TRANSPORT IN CORRELATED OPEN QUANTUM SYSTEMS

N. Walter Talarico

TURUN YLIOPISTON JULKAISUJA – ANNALES UNIVERSITATIS TURKUENSIS
SARJA – SER. AI OSA – TOM. 640 | ASTRONOMICA – CHEMICA – PHYSICA – MATHEMATICA | TURKU 2021

UNIVERSITY OF TURKU

TRANSPORT IN CORRELATED OPEN QUANTUM SYSTEMS

N. Walter Talarico

TURUN YLIOPISTON JULKAISUJA – ANNALES UNIVERSITATIS TURKUENSIS
SARJA – SER. AI OSA – TOM. 640 | ASTRONOMICA – CHEMICA – PHYSICA – MATHEMATIC | TURKU 2021

University of Turku

Faculty of Science
Department of Physics and Astronomy
Doctoral programme in Physical and Chemical Sciences

Supervised by

Prof. Sabrina Maniscalco
Department of Physics and Astronomy
University of Turku
Finland

Dr. Nicola Lo Gullo
Department of Physics and Astronomy
University of Turku
Finland

Reviewed by

Prof. Christian Flindt
Department of Applied Physics
Aalto University
Finland

Prof. Tony J.G. Apollaro
Department of Physics
University of Malta
Malta

Opponent

Prof. Gianluca Stefanucci
Department of Physics
University of of Rome Tor Vergata
Italy

The originality of this publication has been checked in accordance with the University of Turku quality assurance system using the Turnitin OriginalityCheck service.

Cover: N. Walter Talarico

ISBN 978-951-29-8313-1 (PRINT)
ISBN 978-951-29-8313-1 (PDF)
ISSN 0082-7002 (Print)
ISSN 2343-3175 (Online)
Painosalama Oy, Turku, Finland 2021

Acknowledgements

"It's a dangerous business going out of your door.
You step into the road, and if you don't keep your feet,
there's no knowing where you might be swept off to."
—J.R.R. Tolkien

Almost ten years have already passed since when, as a curious guy, I have "swept off" to the path and started this journey questioning the nature of our reality and seeking for answers about the mechanics that underlie the physical world. Have I found those answers? Of course not. Even a lifetime wouldn't be enough to reveal them, but I have grown up and learned from the sense of wonder and the experiences that an unexpected journey reveals along its path. I have gained new skills and awareness about myself and the outside world. Walking through, at last I have reached an unforgettable destination completing my doctoral degree.

Writing down these pages has truly given me the opportunity to look back and recognize that with hard work and persistence anything in life is possible. None of it has been easy or simple and in particular, during the writing process, I have witnessed exceptional times caused by a global pandemic that has influenced our life in many ways. Luckily, I have never been alone during this journey and I am sincerely indebted to everyone I have had the opportunity to meet and learn from throughout these years.

First of all, I would like to express my gratitude to my supervisors: to Sabrina, for your guidance and support throughout my whole Ph.D., for giving me the possibility to work in such a great environment, for trusting me, for inspiring me with your enthusiastic and determined attitude towards the work. Every single experience that we have shared, from the managing of a European research project to the bike riding in the archipelago, has taught me a lot and given me many different skills that go way beyond the world of Academia, thanks a lot for being such an alternative "Boss".

Many thanks to Nicola, for introducing and guiding me into the world of non-equilibrium Green's functions and the numerical methods and programming,

for sharing with me your never-ending knowledge and for teaching me so much, ranging from technical matters, to more fundamental ones. My path would not have been the same without you, so I guess I can forgive your overstated passion for the “red n’blue colors”.
I would like to thank the pre-examiners of this thesis, Prof. Christian Flindt and Prof. Tony J.G. Apollaro; I was truly impressed by the kindness of their reviews.
The whole PhD project could not have been possible without the financial support from the Center of Excellence Quantum Technology Finland program, for which I am particularly grateful.
I would like to extend my gratitude to Boris, Matteo, Guille, Sina, Riku, Teiko, Tom, Leevi, Oskari, Johannes, Juho, Laura, Cate, Jose, Dario, Michele and all the people that, in one way or another, have walked through the corridor of Theoretical Physics and made my experience more interesting and particular with some chats, discussions, or laughs on bad jokes. Thanks so much to my ex office-mates Francesco, Henri and Mikko, we have initiated the infamous legend of the noisy-room, had a lot of funny moments together and good memories.
Thanks to my family for the unconditional and continuous support, especially with the many “pacchi da giù”, they were essential to face the cold Finnish winters.
Finally, I wish to thank You, Laura, for being there when I needed the most. You have been a great source of encouragement and inspiration. Your love and support have allowed to keep me going.

Contents

Abstract

The problem of the dynamics in open and correlated quantum systems has gained attention in recent years due to the impressive experimental advances that were made in quantum transport in molecular systems. The importance of understanding and controlling molecular electronic and quantum transport will soon lead to the realization of quantum technological devices that can be integrated in the present silicon-based technology to make better and faster circuitry. On a fundamental and theoretical level, one needs to take into account time-dependent processes where self-interactions within the parts of an atomic or nano-scale system and interactions with macroscopic external environments are the main cause for quantitative and qualitative changes on the physical and dynamical properties of the quantum system itself.
This thesis aims at discussing the problem of transport in correlated open quantum systems by using the non-equilibrium Green's function approach for describing in particular the effects of correlations in the charge and heat transport dynamics. Unfortunately, because of the unusual two-times structure of the integral formulation that characterized the theory, nowadays there are no commercial software available to carry out the calculations needed to find its solutions, and thus, dedicated software have to be self implemented and programmed. Hence, in the thesis, we first give an introduction of the overall structure of the theory and then a detailed explanation on how to numerically implement tools for several operations on the non-equilibrium Green's functions, the construction of self-energies, and the solution of the integral equations.
Furthermore, as the formalism allows for studying time-dependent transport in interacting and arbitrary nano-scale systems coupled to wide band and macroscopic leads, we present and discuss several applications when these systems are rapidly brought out-of-equilibrium with the application of electrical and thermal biases. More specifically, we theoretically investigate transport of correlations across quasi-crystalline structures and how charge and heat are carried along nanoscopic junctions that span from quantum dots, quantum nanowires and carbon nanotubes.

Tiivistelmä

Avointen ja korreloituneiden kvanttisysteemien tutkimus on saanut viime vuosina paljon huomiota molekyylisysteemeissä tapahtuvan kvantti-kuljetuksen kokeellisten edistysaskelten ansiosta. Molekulaarisen sähkön- ja kvanttisiirron ymmärtämisen tärkeys on sellaisten kvanttiteknologioiden toteuttaminen, jotka voidaan integroida nykyisiin piipohjaisiin teknologioihin parempien ja nopeampien piirien tuottamiseksi. Perustavanlaatuisella ja teoreettisella tasolla on otettava huomioon aikariippuvia prosesseja, joissa sekä itseisvuorovaikutukset atomi- ja nanokokoisten systeemien sisällä että vuorovaikutukset makroskooppisten ympäristöjen kanssa ovat ensisijainen syy kvanttisysteemin fysikaalisten ja aikariippuvien ominaisuuksien laadullisiin ja määrällisiin muutoksiin.
Tämä väitöskirja käsittelee korreloituneissa avoimissa kvanttisysteemeissä tapahtuvan kvantti-siirron problematiikkaa käyttäen hyödyksi epätasapaino Greenin funktioiden lähestymistapaa kuvaamaan erityisesti korrelaatioiden vaikutusta varaus- ja lämpösiirron aikakehityksessä. Valitettavasti teorian karakterisoivasta integraalimuotoilun kaksiaikarakenteesta johtuen nykyään ei ole tarjolla kaupallisia ohjelmistoja jotka pystyvät suorittamaan laskuja ratkaisujen löytämiseksi. Siksi tätä tarkoitusta varten täytyy itse ohjelmoida siihen räätälöityjä ohjelmistoja. Tästä syystä tämä väitöskirja esittelee ensin johdannon ja teorian pääpiirteisen rakenteen. Sen jälkeen käsitellään yksityiskohtaisesti, kuinka implementoida numeerisesti itseisenergiat, integraalimuotojen ratkaisut ja työkaluja useita operaatioita varten epätasapaino Greenin funktioille.
Sen lisäksi formalismi mahdollistaa aikariippuvan siirron tutkimisen vuorovaikuttavissa ja mielivaltaisissa nanomittakaavan systeemeissä, jotka on kytketty makroskooppisiin ja laajan transmissiovyön johtimiin. Esittelemme ja käsittelemme useita sovelluksia, joissa nämä systeemit saatetaan nopeasti pois tasapainosta käyttäen sähkö- ja lämpö-vinoumaa. Tarkemmin sanottuna tutkimme teoreettisesti kuljetusa ja korrelaatioita kvasikiderakenteita pitkin ja kuinka varaus ja lämpö kulkeutuvat pitkin nanokokoisia liitoskohtia, kuten kvanttipisteitä, kvanttinanojohtimia ja hiilinanoputkia.

List of Publications

This thesis consists of a review of the subject and the following original research articles:

I **A Scalable Numerical Approach to the Solution of the Dyson Equation for the Non-Equilibrium Single-Particle Green's Function**,
N.W. Talarico, S. Maniscalco, N. Lo Gullo, Phys. Status Solidi B **256**, 1800501 (2019)

II **Emergence of anomalous dynamics from the underlying singular continuous spectrum in interacting many-body systems**,
J. Settino, *N.W. Talarico*, F. Cosco, F. Plastina, S. Maniscalco, and N. Lo Gullo, Phys. Rev. B **101**, 144303 (2020)

III **Study of the energy variation in many-body open quantum systems: Role of interactions in the weak and strong coupling regimes**,
N.W. Talarico, S. Maniscalco, and N. Lo Gullo,
Phys. Rev. B **101**, 045103 (2020)

IV **Single-Quantum-Dot Heat Valve**,
B. Dutta, D. Majidi, *N.W. Talarico*, N. Lo Gullo, C. B. Winkelmann, H. Courtois, Phys. Rev. Lett., **125**, 237701 (2020)

V **Spectral properties of correlated quantum wires and carbon nanotubes within the Generalized Kadanoff-Baym Ansatz**,
F. Cosco, *N.W. Talarico*, R. Tuovinen, N. Lo Gullo, arXiv preprint arXiv:2007.08901 (2020)

Other published material

This is a list of the publications produced which have not been chosen as a part of this doctoral thesis

- **Entanglement protection via periodic environment resetting in continuous-time quantum-dynamical processes**,
  T. Bullock, F. Cosco, M. Haddara, S. Hamedani Raja, O. Kerppo, L. Leppäjärvi, O. Siltanen, *N.W. Talarico*, A. De Pasquale, V. Giovannetti, and S. Maniscalco, Phys. Rev. A **98**, 042301 (2018)

Chapter 1

Introduction

Non-equilibrium in broad and simple terms relates to every individual physical system and phenomena that are far from the so called equilibrium, from Latin *aequi* and *libra*, well balanced. The thermodynamic meaning of the latter concept refers to the tendency for an isolated system to increase its entropy, or disorder, when opposing forces or influences acting on it are balanced. Even though everyone of us has learned that this is one of the most fundamental aspects ever conceived in modern physics, we do not have to forget the particular circumstances that lead to this rared and privileged state. Indeed, there are a plethora of physical and in particular biological systems that try to avoid the equilibrium state. As was already suggested by Schrödinger in 1944 [1], the very act of living by eating, drinking, breathing, is the perpetual effort to stave off disorder for as long as we can manage. Beside its extremely importance in biology, the non-equilibrium dynamics are of fundamental interest in various fields of physics, both, theoretically and experimentally. Frequently these dynamics concern the physics of interacting quantum many-body systems, where the fundamental constituents of the system like electrons, atoms or molecules, interact with external environments as well as with each other and easily lead to non-equilibrium situations.

There is a large variety of excitation scenarios that drive a many-body system rapidly out-of-equilibrium. These include excitation by strong laser pulses from infrared to x-ray range in the electromagnetic spectrum [2–7]; pump–probe spectroscopy that has evolved as a powerful experimental tool to probe the time evolution of atoms, molecules and materials [8–11]; electrical and thermal transport in correlated nanoscopic junctions for the realization of quantum technological devices [12–18]. Another relevant experimental platform is represented by correlated atoms in optical lattices for which additional excitation schemes have been developed [19–22]. Some of these techniques include rapid changes of the pair interaction (interaction quench) via Feshbach resonance,

rapid changes of confinement potentials (confinement quench) or periodic modulation of the lattice depth (lattice-modulation spectroscopy). In recent years, all these methods have seen a rapid development via sophisticated and well-designed experimental techniques that have allowed for accurate and precise diagnostic of the time evolution of many-body systems.
Despite such a wide range of applications, the theoretical description of out-of-equilibrium many-body systems still remains a challenging task that requires extensive studies and developments in order to achieve detailed comparisons and explanations with the experimental observations. The theoretical difficulty arises because different and fundamental aspects of the many-body problem need to be included in the description. Some of these are the many-body interactions, the inclusion of external time-dependent fields and the possibility for the system to exchange energy and matter with external environments. To give an insight, due to their mutual interactions, the motion of the constituents of a quantum many-body system is dependent on the motion of all the other components of the system itself. This is a fundamental aspect and makes any calculations to solve the many-body problem almost impossible for large systems. Thus, one has to find different ways and strategies to tackle it. One strategy, that was enough to often predict correctly whether a material is a good conductor or not and that was used to obtain correct characteristics for many systems, is to exclude the complicated effects of the inter-particle interactions and treat the constituents as independent, moving in a mean field which mimics the effect of the many-body interactions. Although the solution of such independent-particle systems has been extensively used and has given fairly good results for a long period, this first order approximation method has also led to wrong predictions. To give an example, certain materials that have shown insulating behavior have been predicted to be conductors from independent-electron calculations. The reason for this limited predictive power lies on the fact that there are several cases where the complicated features and the effects of the many-body interaction need to be more carefully considered. Thus, a reliable theoretical description is important, not only for the vast technological implications that will follow from the understanding and the prediction of nanoscale systems behaviors, but also for the fundamentals of many-body physics itself. As it should be clear by now, the major role for having a proper theoretical description of these systems, is played by the many-body interaction, which not only triggers single particle excitations, but also the emergence of collective excitations behavior such as phonon, plasmon and exciton. The electron-electron interaction term also crucially determines the so-called quasi-particle lifetime of the electronic excitations. As we already mentioned, via absorption and photoemission spectra it is possible to experimentally access the one-particle and collective excitations.
However, as was reported previously, solving the many-body problem directly

for atoms with more than a few electrons goes already beyond the present day computational capabilities.
The theoretical approaches that have been applied most extensively in the field of correlated systems are exact diagonalization (CI) [23–25], density-matrix renormalization group (DMRG) methods [26–28], diagrammatic Monte Carlo [29–31], real-time quantum Monte Carlo (RTQMC) [32, 33], reduced-density-matrix approaches [34–36], and time-dependent density-functional theory (TDDFT) [37–40]. However, each of these methods comes with different fundamental problems and limitations. To give some examples, CI is suitable for small systems because it faces an exponential increase of the computational time with the system size. RTQMC can only treat short evolution times due to the dynamic fermion numerical sign problem. DMRG is restricted to 1D systems and is accurate at strong coupling with notable difficulties to consider moderate and weak coupling. Finally, TDDFT has no dimensional restrictions, but it comes with the limitation that is not able to accurately treat the electronic correlations in a systematic way. Besides, TDDFT simulations usually involve the adiabatic approximation which neglects memory effects that result into unreliable predictions. Nowadays, many theoretical research activities are intensely focused on improving and refining each of these approaches and methods.
Another independent approach to study the dynamics of correlated systems that originates in quantum-field theory, is based on the non-equilibrium Green functions (NEGF) that were introduced by Keldysh [41], Kadanoff and Baym [42]. This method has been extensively applied in many different physical scenarios and it has been extremely successful in predicting some of their characteristics. Among others, this includes small atoms and molecules [43, 44], nuclear physics [45–47], high-energy physics [48–50], laser plasmas [51, 52], semiconductor optics [53, 54] and semiconductor quantum transport [55–58]. Furthermore there are several text-book reviews on the topic [54, 59, 60]. Compared to the other methods, the NEGF approach does not suffer from most of the limitations that we have mentioned above and has achieved remarkable results. It was benchmark against CI simulations for small systems, cold-atom experiments and DMRG data, showing impressive accuracy of many physical observables. Nonetheless, the impressive predictive power of this approach has a price to pay: the NEGF methods are complicated and extremely expensive from the computational point of view (details are given in the next Chapters). The use of reduced quantities, instead of the full and complicated state vector or wave function for every particle, is one of the key ingredients in the theory of non-equilibrium Green's functions. This means that by looking at less complicated quantities, like few-particle correlation functions, i.e., expectation values or ensemble averages of field operators, we are still able to theoretically describe an observable and predict its properties. Furthermore, the whole

theory relies on a time-ordering of these ensemble averages of field operators according to a specific path or contour (Keldysh contour [41]) in a complex two-time plane. This path-ordered technique is the reason why the NEGF approach is directly applicable to non-equilibrium problems and to systems evolving under time-dependent external fields. The last but not least relevant feature of the method is that the properties of the many-particle system are obtained by expansion in powers of the interactions via self-energy insertions. The self-energy describes the effect of the mutual-interaction between the constituents of a quantum many-body system and its degrees of approximation are often responsible for the excellent quantitative agreement with benchmark data or experimental results that one could obtain with the method.
The thesis is organized as follows. In Chapter 2, we summarize the theoretical foundations to describe the physics of many-particles systems and we present a brief introduction into the concepts of the non-equilibrium Green's function theory and Keldysh formalism, including the equations of motion for the NEGF—the Keldysh–Kadanoff–Baym and Dyson equations. This is followed by an overall presentation of the main self-energy approximations that we have used in the original publications included in the thesis. In Chapter 3, we present a list of the useful physical quantities to describe transport properties that one can extract within the NEGF framework. In particular, we discuss the original derivation contained in publication **III** for the expression of the energy-current that flow in a correlated open quantum system. Then in Chapter 4, we discuss the details of the numerical implementation for the solution of the dynamical equations for the single-particle Green's function and we provide a short summary of the structure of a scalable open source software/library that we have developed and that is the content of publication **I**. Finally, in Chapter 5, we present several effects and results that characterize different transport setups and models included in the original research articles **I**–**V**.

Chapter 2

Non-equilibrium Green's function theory

In this chapter, we briefly recall the theoretical foundations to describe the physics of many-particles systems. The aim of this section is to give an overall presentation of the mathematical tools based on the non-equilibrium Green's function theory and Keldysh formalism used in the original publications. Firstly, we introduce the quantum-mechanical model that represents a many-particles system and then the technique based on the non-equilibrium Green's function and the many-body perturbation theory needed to characterize the dynamics of such a system. Our main focus here is not a full and rigorous description of the method, instead we give a general framework and we refer to more extensive and comprehensive reviews for further details [60–63].

2.1 Models for many-body open quantum systems

In order to describe transport of energy and particles in nano-scale devices, we need to construct a quantum-mechanical model that takes into account the relative positions, the energy configurations and the interactions between many identical particles confined in well-defined structures. In the exact quantum theory formulation based on the solution of the time-dependent Schrodinger equation [64, 65], this is absolutely non trivial because of the need to deal directly with the many-particle wave functions. The second quantization or occupation number representation [61–63, 66] can be used to simplify the description in terms of creation and annihilation operators that add or remove particles into/from the system of interest. The statistical mechanics, Fermi (Bose) statistics, are built-in automatically and most importantly, we have a powerful tool to treat systems with variable number of particles, a very fre-

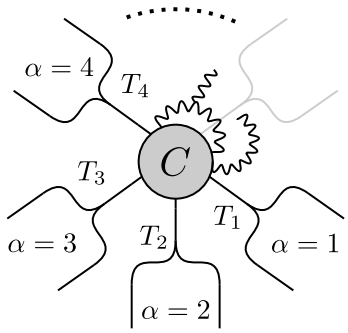

Figure 2.1: Schematic representation of the multiterminal transport model described by Eq. (2.1). A central correlated quantum system (C) tunnel-coupled (T_α) to an arbitrary number of macroscopic leads.

quent situation in non-equilibrium phenomena. A typical quantum transport setup consists of two or more non-interacting macroscopic and metallic electron reservoirs (leads) and a microscopic scattering region (e.g. a quantum dot, quantum wire, or a molecular system) which is attached to these reservoirs and can exchange particles and energy with them. A schematic representation of this model system is shown in Fig. 2.1. The general Hamiltonian describing this transport setup consists of three terms

$$\hat{H}(z) = \hat{H}_C(z) + \sum_{\alpha=1}^{N} \hat{H}_\alpha(z) + \sum_{\alpha=1}^{N} \hat{V}_{\alpha C}(z), \tag{2.1}$$

where z is a generic complex time variable on the Keldysh contour γ [41, 54, 59, 60], Fig. 2.2 [1]. The Hamiltonian in second quantization in terms of creation and annihilation operators for the central correlated region is given by

$$\hat{H}_C(z) = \int d\mathbf{x}_1 \; \hat{\psi}^\dagger(1) h(1) \hat{\psi}(1) + \frac{1}{2} \int d\mathbf{x}_1 d1' \; \hat{\psi}^\dagger(1) \hat{\psi}^\dagger(1') v(1,1') \hat{\psi}(1') \hat{\psi}(1). \tag{2.2}$$

The indices $1 = (\mathbf{x}_1, z_1)$, $1' = (\mathbf{x}_1', z_1')$ are collective indices for the position-spin coordinate $\mathbf{x} = (\mathbf{r}, \sigma)$ and complex-time z. The single-particle Hamiltonian in the central region $h(1)$ contains the kinetic energy and a general

[1] Notice that even though we deal with real-time operators, like the Hamiltonian, we can always express them along the complex-time contour provided that they are the same on the forward and backward branches of the contour $\hat{H}(z = t_\pm) = \hat{H}(t)$, with $t_\pm \in \gamma$

time-dependent external potential. $v(1,2) = \delta_\gamma(z_1 - z_2)v(\mathbf{x}_1, z_1; \mathbf{x}_2, z_2)$ is a generic two-body interaction between pairs of electrons in the scattering region. The latter can be the familiar Coulomb interaction or local interactions where $v(\mathbf{x}, z; \mathbf{x}', z') \sim \delta(\mathbf{x} - \mathbf{x}')$, ubiquitous in model systems used to describe experimental platforms with ultra-cold atomic gases [67]. The fermion-field operators satisfy the usual anti-commutation relations $\{\hat{\psi}^\dagger(\mathbf{x}), \hat{\psi}(\mathbf{x}')\} = \delta(\mathbf{x}-\mathbf{x}')$ and $\{\hat{\psi}^\dagger(\mathbf{x}), \hat{\psi}^\dagger(\mathbf{x}')\} = \{\hat{\psi}(\mathbf{x}), \hat{\psi}(\mathbf{x}')\} = 0$, these relations reflect the antisymmetry property of the many-body wave function and thus its statistics. In an analogous way, the non-interacting particles in the α-th lead are described by

$$\hat{H}_\alpha(z) = \int d\mathbf{x}_1 \hat{\psi}^\dagger_\alpha(1) h_\alpha(1) \hat{\psi}_\alpha(1) \tag{2.3}$$

with $h_\alpha(1)$ the single particle Hamiltonian of the α-th lead and similar anti-commutation relations as before for their fermionic-field operators. The Hamiltonian accounting for the coupling between the interacting region and the leads is chosen to be tunnel-like and given by

$$\hat{V}_{\alpha C}(z) = \int d\mathbf{x}_1 \left(\hat{\psi}^\dagger(1) T_\alpha(1) \hat{\psi}_\alpha(1) + \text{h.c.} \right), \tag{2.4}$$

with $T(1)$ describing the amplitude energy needed for a particle to tunnel across the interacting region and the α-th lead. The representation of the total Hamiltonian in terms of the field operators is a useful and powerful tool to carry out calculations and derivations along the complex-time contour, see Sec. 3.4. Nonetheless, for practical numerical calculations it is convenient to expand the field operators into a suitable single-particle basis. The latter is chosen accordingly to the problem at hand in such a way to retain only the most relevant degrees of freedom for the specific physical scenario considered.

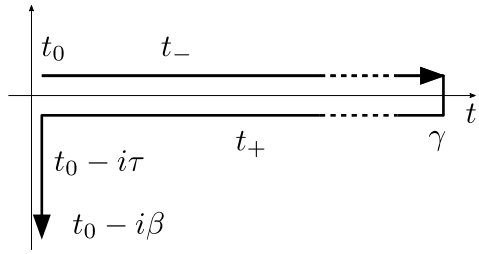

Figure 2.2: Keldysh complex-time contour γ. The arrows denote the time ordering on the contour with the latest time being one on the vertical track. Observables along the forward and backward branches are assumed to be equal $O(z = t_\pm) = O(t)$.

A possible and very general choice is the spin-orbital basis $\varphi_i(\mathbf{x}) = \varphi_i(\mathbf{r})\delta_{\sigma\tau}$, using which we can express the creation and annihilation operators $\hat{d}^\dagger_{i\sigma}, \hat{d}_{i\sigma}$ for the state $i\sigma$ as a linear combination of field operators at different position-spin coordinates

$$\hat{d}^\dagger_{i\sigma} \equiv \int d\mathbf{x}\ \varphi_i(\mathbf{x})\hat{\psi}^\dagger(\mathbf{x}) \tag{2.5}$$

$$\hat{d}_{i\sigma} \equiv \int d\mathbf{x}\ \varphi^*_i(\mathbf{x})\hat{\psi}(\mathbf{x}). \tag{2.6}$$

where the integral is $\int d\mathbf{x} = \sum_\sigma \int d\mathbf{r}$. The operators $\hat{d}^\dagger_{i\sigma}$ and $\hat{d}_{i\sigma}$ inherit the anti-commutation rules from the field operators $\hat{\psi}^\dagger$ and $\hat{\psi}$. Eq. (2.5) and (2.6), together with their anti-commutation relations, lead to the following representation for the Hamiltonian

$$\hat{H}_C(z) = \hat{H}_0(z) + \hat{V}(z) \tag{2.7}$$

$$\hat{H}_0(z) = \sum_{ij,\sigma} h_{ij}(z)\hat{d}^\dagger_{i\sigma}\hat{d}_{j\sigma} \tag{2.8}$$

$$\hat{V}(z) = \frac{1}{2}\sum_{ijkl}\sum_{\sigma\sigma'} v_{ijkl}(z)\hat{d}^\dagger_{i\sigma}\hat{d}^\dagger_{j\sigma'}\hat{d}_{k\sigma'}\hat{d}_{l\sigma} \tag{2.9}$$

$$\hat{H}_\alpha(z) = \sum_{ij\in\alpha,\sigma} h_{\alpha ij}(z)\hat{c}^\dagger_{i\sigma}\hat{c}_{j\sigma} \tag{2.10}$$

$$\hat{V}_{\alpha C}(z) = \sum_{i\in C, j\in\alpha,\sigma}\Big(T_{\alpha ij}(z)\hat{d}^\dagger_{i\sigma}\hat{c}_{j\sigma} + \text{h.c.}\Big) \tag{2.11}$$

where the matrix elements in the spin-orbit basis of the one-body parts are given by

$$h_{ij}(z) = \int d\mathbf{r}\ \varphi^*_i(\mathbf{r})h(\mathbf{r},z)\varphi_j(\mathbf{r}) \tag{2.12}$$

$$h_{\alpha ij}(z) = \int d\mathbf{r}\ \varphi^*_i(\mathbf{r})h_\alpha(\mathbf{r},z)\varphi_j(\mathbf{r}) \tag{2.13}$$

$$T_{\alpha ij}(z) = \int d\mathbf{r}\ \varphi^*_i(\mathbf{r})T_\alpha(\mathbf{r},z)\varphi_j(\mathbf{r}) \tag{2.14}$$

while the two-body matrix elements describing the electron-electron interaction is

$$v_{ijkl}(z) = \int d\mathbf{r}d\mathbf{r}'\ \varphi^*_i(\mathbf{r})\varphi^*_j(\mathbf{r}')v(\mathbf{r},\mathbf{r}',z)\varphi_k(\mathbf{r}')\varphi_l(\mathbf{r}). \tag{2.15}$$

To simplify the model, we have assumed that both the single particle Hamiltonian h and the interaction v are spin independent, even so it is easy to generalize the above expressions in the case where a magnetic field and/or spin orbit coupling is present.

2.2 Dyson equation and two-time evolution

In this section we review for completeness the main elements of the non-equilibrium Green's function theory (NEGF), as well as the key ingredients of the many-body perturbation theory (MBPT) used to treat interactions in weakly interacting fermions and couplings of such a system with external macroscopic reservoirs. The Keldysh Green's function theory [41, 42, 63] includes as limiting cases the zero-temperature Green's function (time-ordered) and the Matsubara formalism which are recovered by specific choices of the contour in the complex-time plane. Furthermore, it retains the formal structure of the many-body perturbation theory extending it to non-equilibrium phenomena. It allows for a systematic study of time-dependent expectation values and steady-state properties when electron-electron (electron-phonon) interaction is present. The correlation effects of the interaction are included via an integral kernel called self-energy that can be methodically constructed via a diagrammatic expansion of selected Feynman diagrams. We start the section by introducing the definition and properties of the NEGF as well as the equations that rule their dynamics on the complex-time contour and then we outline the steps that led to the MBPT in the two-time plane. Our aim is to give a brief characterization and few examples of the most used electronic self-energies approximations which embody both the role of many-body interactions and the coupling with external leads.

2.2.1 Single-particle Green's functions

The starting point in the theory of the non-equilibrium Green's function together with the many-body perturbation expansion is the definition of the single-particle Green's function (SPGF) as the expectation value of the contour-ordered product of the creation and annihilation operators

$$G(1,1') = -i \left\langle \mathcal{T}_\gamma \left[\hat{\psi}_H(1) \hat{\psi}^\dagger_H(1') \right] \right\rangle_0 \tag{2.16}$$

here the subscript H denotes the Heisenberg picture and the indexes $1 = (\mathbf{x}_1, z_1)$ and $1' = (\mathbf{x}'_1, z'_1)$ are collective indexes for position, spin and complex-time. Furthermore, z and z' are a contour time variables and $\mathcal{T}_\gamma$ orders the operators along the Keldysh contour γ by arranging the operators with later contour times to left Fig. 2.2. Similarly, we denote by $h(1)$ the matrix elements of the first quantized Hamiltonian $\hat{h}$ in the position, spin and complex-time indexes. Here the symbol $\langle \dots \rangle_0$ denotes the average over the initial many-body thermal state. By applying $[i\partial_{z_1} - h(z)]$ and using the Heisenberg equations of motion for the field-operators $\hat{\psi}$ and $\hat{\psi}^\dagger$ under the evolution given by $\hat{H}_C(z)$ on the complex-time contour, one obtains the first equation of the Martin-

Schwinger hierarchy (MSH):

$$\Big(i\partial_{z_1} - h(1)\Big)G(1,1') = \delta(1,1') - \int d\bar{1} v(1,\bar{1}) G_2(1,\bar{1};1',\bar{1}^+) \tag{2.17}$$

where $G_2(1,2;1',2') = (-i)^2 \left\langle \mathcal{T}_\gamma \left[\hat{\psi}_H(1)\hat{\psi}_H(2)\hat{\psi}^\dagger_H(2')\hat{\psi}^\dagger_H(1')\right]\right\rangle_0$ is the two-particle Green's function. Here the integral is $\int d\bar{1} = \int d\bar{\mathbf{x}}_1 \int_\gamma d\bar{z}_1$ and $1^+ = (\mathbf{x}_1, z_1 + \delta)$ denotes a time with an infinitesimally small shift δ on the Keldysh contour γ. A similar equation is obtained by acting to the left with the operator $\Big(-i\partial_{z_1'} - h(1')\Big)$. With the contour Heisenberg equations and contour calculus as described above, one can derive the equations of motion for the two and higher particle Green's functions, and find equations which couple the N-particle one to the $(N+1)$-particle Green's function. In many practical situations, see Chap. 3 for more details, the knowledge of the single-particle Green's function is sufficient to describe the physical problem at hand, in this case it is suitable to introduce the so-called single-particle self-energy Σ, which allows one to (formally) decouple the time-evolution of the Green's function from those of the $(N > 1)$-particle Green's functions and obtain a closed equation for the one-particle one. In order to truncate the MSH, the self-energy is implicitly defined as:

$$\int d\bar{1}\Sigma(1,\bar{1})G(\bar{1},1') = -\int d\bar{1} v(1,\bar{1}) G_2(1,\bar{1};1',\bar{1}^+) \tag{2.18}$$

The physical meaning of the self-energy Σ is to introduce an effective function which accounts for the two-particles scattering which are encoded into the two-particles Green's function G_2. Thanks to the definition of Σ with Eq. (2.18) one obtains the following equation on the complex contour for the single-particle Green's functions:

$$\Big(i\partial_{z_1} - h(1)\Big)G(1,1') = \delta(1,1') + \int d\bar{1}\Sigma(1,\bar{1})G(\bar{1},1') \tag{2.19}$$

which has to be solved with the Kubo-Martin-Schwinger (KMS) boundary conditions $G(t_0, z_1') = -G(t_0 - i\beta, z_1')$, following directly from Eq. (2.16) and the cyclic property of the trace. By means of the Langreth and Wilkins rules [60, 68], it is possible to project these equations of motion for the single-particle Green's function onto the real and imaginary time axis. The resulting set of equations for those components are called the Kadanoff-Baym equations [42, 69] and represent, together with the initial conditions, the standard way to completely determine the single-particle Green's functions once a choice for the self-energy is made. The numerical implementation of the solution of such equations has been extensively explored and requires fine and elegant schemes for the two-times propagation [43, 44, 59, 60].

An alternative approach to find the interacting Green's function in Eq. (2.16) is to use the interaction picture and then to expand the evolution operator containing the interaction term $\tilde{V}(z)$,

$$G(1,1') = -i\frac{\sum_{k=0}^{\infty}\frac{(-i)^k}{k!}\int\cdots\int_\gamma\left\langle\mathcal{T}_\gamma\left[\tilde{V}(z_1)\ldots\tilde{V}(z_k)\tilde{\psi}(1)\tilde{\psi}^\dagger(1')\right]\right\rangle_0}{\sum_{k=0}^{\infty}\frac{(-i)^k}{k!}\int\cdots\int_\gamma\left\langle\mathcal{T}_\gamma\left[\tilde{V}(z_1)\ldots\tilde{V}(z_k)\right]\right\rangle_0} \tag{2.20}$$

where the tilde is used to denote operators in the interaction picture. That is, if we are able to compute contour time-ordered products then we have a general and powerful way to obtain the SPGF. This can be done for some particular cases, for example by means of the Wick's theorem [60] we can write down a series expansion for the interacting single-particle Green's function in terms of the non-interacting one $G_0(1,1')$, which satisfies the following equations:

$$\Big(i\partial_{z_1} - h(1)\Big)G_0(1,1') = \delta(1,1') \tag{2.21}$$

$$G_0(1,1')\Big(-i\overleftarrow{\partial}_{z_1'} - h(1')\Big) = \delta(1,1'). \tag{2.22}$$

By collecting the wanted terms of this series expansion and systematically representing them as Feynman diagrams one can built a proper self-energy and obtain the Dyson equation for the SPGF:

$$G(1,1') = G_0(1,1') + \int d\bar{1}\, d\bar{2}\, G_0(1,\bar{1})\Sigma(\bar{1},\bar{2})G(\bar{2},1') \tag{2.23}$$

The Dyson equation is the formal solution of the Martin-Schwinger hierarchy for the one-particle Green's function, as one can easily verify by applying $(i\delta(1,1')\partial_{z_1} - h(1',1))$ to Eq. (2.23) to obtain Eq. (2.19) with the help of Eq. (2.21). Because of that, the Dyson equation is formally equivalent to Eq. (2.19) and it contains the same physical information about the dynamics of the single-particle Green's function through the double time integral on the r.h.s. of Eq. (2.23). The last integration is performed along the Keldysh time-contour γ and thus encompasses information of the statistical physics (vertical track) as well the time-ordered and anti-time ordered dynamics (horizontal branches) (see Fig. 2.2) that the system is subjected to. Moreover, the correlation effects of the interaction are included via the integral kernel represented by the self-energy functional. Before proceeding, we shortly want to recall the main definitions for the functions with time arguments on the real and imaginary branches of the complex-contour γ. The choice of the localized single-particle basis and the field operators representation on this basis (2.5) and (2.6), allow us to write down the basis representation of a generic double

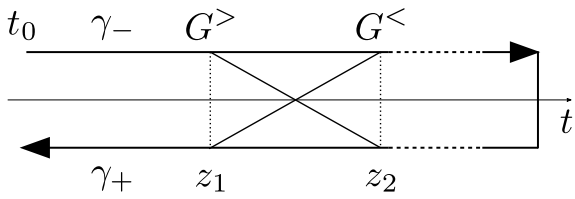

Figure 2.3: Forward and backward branches of the Keldysh complex-time contour $\gamma = \gamma_- \oplus \gamma_+$. Position along the contour of the two-time arguments for the lesser and greater components of the function $G(z_1, z_2)$.

multi-indices quantity as:

$$\begin{aligned} A(1,2) &= A(\mathbf{x}_1 z_1, \mathbf{x}_2 z_2) \\ &= \sum_{ij} \phi_i^*(\mathbf{x}_1)\phi_j(\mathbf{x}_2) A_{ij}(z_1, z_2), \end{aligned} \tag{2.24}$$

as before the indices i,j represent spatial and spin degrees of freedom. In what follows, to lighten the notation, we usually drop the single-particle basis indices when the quantities have the explicit complex-time dependence $A_{ij}(z, z') \equiv A(z, z')$. Any two-time function defined on the contour is said to belong to the Keldysh space and in general such function can be written as

$$A(z, z') = \delta(z, z')A^\delta(z) + \theta(z, z')A^>(z, z') + \theta(z', z)A^<(z, z') \tag{2.25}$$

where $\theta(z, z')$ is the contour Heaviside step function, i.e.:

$$\theta(z, z') = \begin{cases} 1, & \text{for} \quad z > z' \\ 0, & \text{otherwiswe} \end{cases} \tag{2.26}$$

here the symbol $>$ is intended as *later* with respect to the ordering on the contour. The contour delta function is defined as $\delta(z, z') = \partial_z \theta(z, z')$. Examples of quantities like $A(z, z')$ in Eq. (2.25) are of course the Green's function, whose singular part G^δ is zero, and the self-energy, with the time-local part given by the Hartree-Fock self-energy $\Sigma^\delta = \Sigma_{HF}[G]$, see Sec. 2.2.2. The greater $A^>(z, z')$ and lesser $A^<(z, z')$ term respectively denote the correlation parts. From this expression we can define several subordinated functions. It is customary to denote by $z = t_-$ points on the forward branch of the complex-contour, $z = t_+$ point on the backward branch and $z = t_0 - i\tau$ points on the vertical track, Fig. 2.2. The Keldysh components lesser ($<$), greater ($>$), retarded (R), advanced (A), left ($\lceil$), right ($\rceil$) and Matsubara (M) can be

defined accordingly to the different positions of the two-time coordinates on the contour of a generic two-time function [54, 59, 60], see Fig. 2.3,

$$A^M(\tau,\tau') = A(t_0 - i\tau, t_0 - i\tau') \tag{2.27}$$
$$A^{\ulcorner}(\tau,t') = A(t_0 - i\tau, t') \tag{2.28}$$
$$A^{\urcorner}(t,\tau) = A(t, t_0 - i\tau) \tag{2.29}$$
$$A^{\lessgtr}(t,t') = A(t_\mp, t'_\pm) \tag{2.30}$$
$$A^{R/A}(t,t') = A^\delta(t)\delta(t-t') \pm \theta(\pm(t-t'))[A^>(t,t') - A^<(t,t')]. \tag{2.31}$$

It is also useful to recall the symmetry properties between these different real/imaginary time components of a generic two-times function. Those are given in the single-particle basis (for fermions) by:

$$A^M_{ji}(\tau,\tau') = -A^M_{ij}(\tau,\tau')^* \tag{2.32}$$
$$A^{\ulcorner}_{ij}(\tau,t) = A^{\urcorner}_{ji}(t,\beta-\tau)^* \tag{2.33}$$
$$A^A_{ji}(t',t) = A^R_{ij}(t,t')^* \tag{2.34}$$
$$A^{\lessgtr}_{ji}(t',t) = -A^{\lessgtr}_{ij}(t,t')^* \tag{2.35}$$

where $A = G, \Sigma$. The importance of the symmetries in this context is that they allow to reduce both the computational time and the memory required. With the definitions in Eq.s (2.27)−(2.31), the properties in Eq.s (2.32)−(2.35) and with the help of the Langreth rules for the projection of integral of products of two Keldysh functions [60, 68], we can write the equations for the real-time components of the Dyson equation:

$$G^M(\tau,\tau') = \Big[G_0^M + G_0^M \star \Sigma^M \star G^M\Big](\tau,\tau'), \tag{2.36}$$

$$G^{R/A}(t,t') = \Big[G_0^{R/A} + G_0^{R/A} \cdot \Sigma^{R/A} \cdot G^{R/A}\Big](t,t'), \tag{2.37}$$

$$G^{\ulcorner}(\tau,t') = \Big[G_0^{\ulcorner} + G_0^{\ulcorner} \cdot \Sigma^A \cdot G^A + G_0^M \star \Sigma^{\ulcorner} \cdot G^A + G_0^M \cdot \Sigma^M \star G^{\ulcorner}\Big](\tau,t'), \tag{2.38}$$

$$G^{\urcorner}(t,\tau) = \Big[G_0^{\urcorner} + G_0^R \cdot \Sigma^R \cdot G^{\urcorner} + G_0^R \cdot \Sigma^{\urcorner} \star G^M + G_0^{\urcorner} \star \Sigma^M \star G^M\Big](t,\tau), \tag{2.39}$$

$$G^{\lessgtr}(t,t') = \Big[G_0^{\lessgtr} + G_0^R \cdot \Sigma^{\lessgtr} \cdot G^A + G_0^{\lessgtr} \cdot \Sigma^A \cdot G^A + G_0^R \cdot \Sigma^R \cdot G^{\lessgtr} + G_0^{\rceil} \star \Sigma^M \star G^{\lceil} + G_0^R \cdot \Sigma^{\rceil} \star G^{\lceil} + G_0^{\rceil} \star \Sigma^{\lceil} \cdot G^A\Big](t,t'). \tag{2.40}$$

The notations $\cdot$ and $\star$ denote the real-time and imaginary-time convolutions:

$$[A \cdot B](t,t') = \int_{t_0}^{\infty} A(t,\bar{t})B(\bar{t},t')d\bar{t}, \tag{2.41}$$

$$[A \star B](\tau,\tau') = -i\int_{t_0}^{t_0-i\beta} A(\tau,\tau)B(\tau,\tau')d\tau, \tag{2.42}$$

with A, B two generic functions on the contour and where the matrix multiplication among indices of the single-particle basis is assumed. Similar expressions hold for functions with mixed time arguments on horizontal and vertical branches of the contour.
Eq. (2.36) is the only equation which is completely decoupled from all other equations and gives information on the initial state preparation of the system at time t_0. All other equations are coupled and their solution has to be found self-consistently as discussed in the next section. Eqs. (2.38) and (2.39) give the contributions of the initial state to the dynamical properties of the system, whereas the retarded and advanced components, solutions of Eqs. (2.37), contain the spectral characteristics and properties of the system at hand. The solution of Eqs. (2.40) instead, describes the dynamical correlation effects carried by the particle and hole propagators.

Equation (2.23) shows us that by starting from the non-interacting solution we can obtain the full interacting Green's function G at the level of the chosen self-energy approximation Σ via an iterative procedure. This iterative procedure of generating the full interacting Green's function from the non-interacting one is called dressing of the Green's function. With this compact notation that highlights the time structure only is much easier to see the underlying connections between these quantities and to represent them by the corresponding Feynman diagram. The fully connected vertices, the ones that describe propagation-interaction-propagation or similar events and processes, that correspond to the integration variables are implicitly determined by the times coordinates. So equation (2.23) can be shortly represented as

$$G(1,2) = G_0(1,2) + G_0(1,3)\Sigma(3,4)G(4,2) \tag{2.43}$$

with corresponding Feynman diagram as shown in Fig. 2.4.

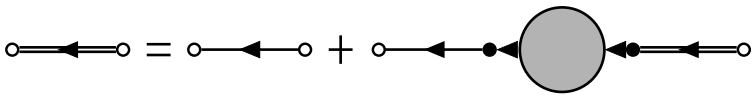

Figure 2.4: Diagrammatic representation of the Dyson equation Eq. (2.23) or equivalently Eq. (2.43). Directed double solid lines represent the non-equilibrium Green's function G, the directed solid line is the non-interacting single-particle Green's function G_0 and the shadow gray circle with ingoing and outgoing lines is the many-body self-energy Σ. Solid black dots indicate inner vertices where summation over all degrees of freedom and integration over contour variables is assumed.

2.2.2 Many-body self-energy

As we mentioned in the previous section, in order to account for the effect of many-body interactions in the dynamics of the single-particle Green's function it is possible to define a self-energy which describes the effect of the whole system at the single particle level. Formally, the self-energy arise either as a way to truncate the Martin-Swinger hierarchy or, in the diagrammatic expansion of the evolution operator, as a way to choose which physical processes are relevant to describe the physical system. In the first case one obtains

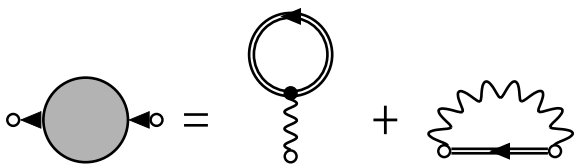

Figure 2.5: Diagrammatic representation of the Hartree-Fock self-energy Eq. (2.45). It is made of the tadpole or Hartree diagram (first term) and the first order exchange diagram (Fock, second term). The wavy line represents the electron-electron interaction.

the Kadanoff-Baym equations, whereas in the second one the Dyson equation or, in a more general framework, the set of Hedin equations [60]. In either case, the choice of the self-energy is, to some extent, left to the needs of the problem addressed, meaning that the choice of the diagrams to be included in the self-energy depends only upon the physical processes which are believed to contribute the most to the specific case at hand. However, there are some general restrictions that need to be consider, specifically those imposed by the macroscopic conservation laws. To guarantee that the latter are preserved, such as conservation of particle, momentum, energy, and angular momentum, the self-energy has to be the functional derivative of a Luttinger-Ward functional $\Phi[G]$ [60, 70, 71]. This last quantity can be easily calculated using standard diagrammatic techniques when the nature of the scattering process (the interaction) is known [60]. The self-energies which are functional derivatives of some Φ functional are call Φ-derivable:

$$\Sigma_{MB}(1,1') = \frac{\delta\Phi[G]}{\delta G(1',1)}. \tag{2.44}$$

In this case the resulting single-particle Green's function is guaranteed to fulfill macroscopic conservation laws. This introduces a non-trivial problem if one attempts to find the interacting Green's function. Because of its Φ-derivable property, the self-energy is a functional of the *interacting* single-particle Green's function itself which in turn can be found only through the knowledge of the self-energy. Therefore, conservation laws are satisfied if and only if a self-consistent procedure is employed. Because of this self-consistent nature of the problem, it is reasonable and understandable to resort on numerical techniques to tackle it, see Sec. 4. The most well-known conserving approximations for the many-body self-energy are the Hartree-Fock (HF), the second Born (2B), the GW, and the T-matrix approximations. In this thesis, we present the first three of these approximations and we give a brief recall of their properties. The first-order approximation for the self-energy, i.e. the HF approximation, has the following functional form

$$\Sigma_{HF}[G](1,1') = -i\delta(1,1')\int d\bar{1}v(1,\bar{1})G(\bar{1},\bar{1}^+) + iG(1,1')v(1^+,1'). \tag{2.45}$$

Its diagrammatic representation is depicted in Fig. 2.5. This approximation describes how a particle moves freely under the influence of an effective potential which depends on all the other particles, that is the HF self-energy includes the effects of the interaction through a mean-field approximation. The HF self-energy require only one integral over the spatial degrees of freedom and not over time due to the delta like structure of $v(t,t')$ in the double time plane. This approximation is mostly used to take into account the mean-field effect like the global shift of the single-particle energies due to the many-body

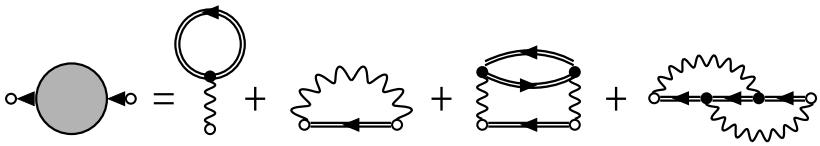

Figure 2.6: Diagrammatic representation of the second Born self-energy Eq. (2.46). Beside the HF terms, it contains the first order bubble diagram (third term) and the second order exchange diagram (forth term).

interaction.
Up to the second-order approximation for the self-energy, the first example which one encounters is the 2B:

$$\Sigma_{2B}[G](1,1') = \Sigma_{HF}[G](1,1') - i^2 G(1,1') \int d\bar{1}d\bar{2} v(1,\bar{1}) G(\bar{1},\bar{2}) G(\bar{2},\bar{1}) v(1',\bar{2}) + i^2 \int d\bar{1}d\bar{2} v(1,\bar{1}) G(1,\bar{2}) G(\bar{2},\bar{1}) G(\bar{2},1') v(1',\bar{2}) \tag{2.46}$$

here, in addition to the time-local part of the self-energy (Σ_{HF}), we have terms up to the second order in the Coulomb interaction $v(z,z') = v(\mathbf{x},\mathbf{x}')\delta(t,t')$. The first term after the HF-part of the self-energy is generally denoted as first order bubble diagram, it describes propagation of a particle (or hole) while interacting with particle hole-pair, i.e., it includes to first order effects of the polarization of the media due to uneven density distribution of particles and holes. The last term is nothing but the second order correction to the Fock term, second term in the r.h.s of Eq. (2.45), see Fig. 2.6. Notice that also the 2B does not require integration over time, once again due to the delta-like structure of the two-body interaction potential.
In the GW approximation the electronic self-energy takes the form

$$\Sigma_{GW}[G](1,1') = \Sigma_H(1,1') + iG(1,1')W(1,1') \tag{2.47}$$

with Σ_H being the Hartree part of the self-energy, the first term of the r.h.s of Eq. (2.45), and where the dynamically screened interaction W satisfies the Dyson equation

$$W(1,1') = v(1,1') + \int d\bar{1}d\bar{2} v(1,\bar{1}) P(\bar{1},\bar{2}) W(\bar{2},1'), \tag{2.48}$$

the polarization is usually approximated in the random-phase approximation (RPA) as $P(z,z') = -iG(z,z')G(z',z)$, see Fig. 2.7. The GW approximation

can be seen as a dynamically screened exchange approximation able to describe the effects of long-range interaction. From the computational point of view it is more complex than the HF or the 2B as it requires to solve the equation for the dressed interaction W, which is a Dyson-like equation and it involves integration in both time and spatial degrees of freedom. Other choices for the polarization diagram are possible [60, 72] but, even if they result in more accurate and precise approximations, they typically make the computation more demanding. In fact, this corresponds to include in the set of equations to be solved a vertex functional which as a consequence leads to a more involved set of equations than the ones including only the Green's function and the self-energy. This set, named Hedin equations, is made of five equations which have to be solved at the same time and self-consistently. The difficulties arise mostly due to the nature of the vertex functional which has in general a tensor structure in the localized base and it is not trivially manageable in the Keldysh space.

2.2.3 Embedding self-energy

For an open interacting system, the self-energy in Eq. (2.23) has to take into account not only the many-body interactions, but also the tunneling of electrons between the central region and the leads. As opposite to the many-body self-energy that needs to be treated with a proper perturbation scheme, the self-energy that accounts for the effects of leads (embedding self-energy) can be treated exactly in the NEGF formalism. The embedding self-energy can be shown to be proportional to the non-interacting lead Green's function, in

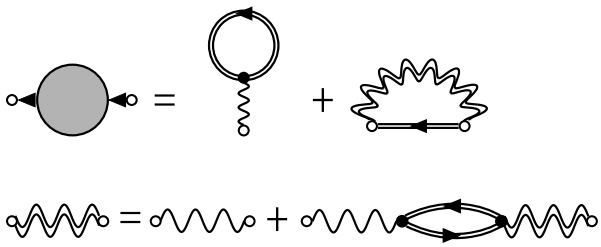

Figure 2.7: Diagrammatic representation of the GW self-energy Eq. (2.47) (top). In this approximation the Fock term is calculated with the dynamically screened interaction W (double wavy solid line). In the random phase approximation the latter quantity satisfies its own Dyson equation Eq. (2.48) (bottom).

the localized single-particle basis we can express this quantity as

$$\Sigma_{emb}(z,z') = \sum_{\alpha} \Sigma_{\alpha,ij}(z,z') = \sum_{\alpha} \sum_{k}^{\mathcal{N}_\alpha} T_{\alpha,ik} g_{k,\alpha}(z,z') T^*_{\alpha,kj} \tag{2.49}$$

here k labels the energy-levels in the leads, whereas i,j label the sites in the central region. Furthermore, $\mathcal{N}_\alpha$ is the number of sites in the lead α (in all the publications we have considered a continuum of states for the leads $\mathcal{N}_\alpha \to \infty$). The lesser and greater real-time components of the non-interacting Green's function of the leads are given by:

$$g^<_{\alpha,k}(t,t') = i f(\epsilon_{\alpha,k}) e^{-i\int_{t'}^{t}(\epsilon_{\alpha,k}-\mu+V_\alpha(\bar{t}))d\bar{t}} \tag{2.50}$$

$$g^>_{\alpha,k}(t,t') = i(f(\epsilon_{\alpha,k})-1) e^{-i\int_{t'}^{t}(\epsilon_{\alpha,k}-\mu+V_\alpha(\bar{t}))d\bar{t}} \tag{2.51}$$

where $V_\alpha(t)$ is the time-dependent applied bias voltage in the lead α, the function $f(\epsilon) = 1/(e^{\beta(\epsilon-\mu)}+1)$ is the Fermi-Dirac distribution function that describes the non-interacting equilibrium electrons of the α-leads with chemical potential μ and inverse temperature $\beta = 1/T$. By introducing the dissipation matrix rate:

$$\Gamma_{\alpha,ij}(\epsilon) = 2\pi \sum_{k}^{\mathcal{N}_\alpha} T_{\alpha,ki}\delta(\epsilon-\epsilon_{\alpha,k}) T^*_{\alpha,ki} \tag{2.52}$$

the expressions for the lesser and greater components of the embedding self-energies read:

$$\Sigma^<_{\alpha,ij}(t,t') = i e^{-i\int_{t'}^{t} V_\alpha(\bar{t})d\bar{t}} \int \frac{d\epsilon}{2\pi} \Gamma_{\alpha,ij}(\epsilon) f(\epsilon) e^{-i(\epsilon-\mu)(t-t')} \tag{2.53}$$

$$\Sigma^>_{\alpha,ij}(t,t') = i e^{-i\int_{t'}^{t} V_\alpha(\bar{t})d\bar{t}} \int \frac{d\epsilon}{2\pi} \Gamma_{\alpha,ij}(\epsilon) (f(\epsilon)-1) e^{-i(\epsilon-\mu)(t-t')} \tag{2.54}$$

Furthermore, the $\lceil,\rceil$ and M component are similarly worked-out by considering the time-arguments on different parts of the Keldysh contour. The calculation of the embedding self-energy is particularly straightforward as it does not depend upon the interacting Green's function of the system and therefore it needs to be calculated only once with the computational effort given solely by the integration over the frequencies. In the original publications, we adopt the wide band limit approximation (WBLA) which assumes that the energy bandwidth of the electronic reservoirs is the largest energy scale and thus the dissipation matrix rate is energy-independent $\Gamma_{\alpha ij}(\varepsilon) = \Gamma_{\alpha ij}$. Moreover, we choose a purely imaginary constant for the dissipation rate, this practically stands in neglecting all possible energy-shifts effects induced by the coupling with the electronic leads.

2.2.4 Inbedding technique

Up until now we have been focused on the SPGF of the microscopic scattering region and on how we could include the influence of correlation effects and couplings to macroscopic external reservoirs on this system. Nonetheless, one could also be interested in the effects that the correlated central system has on the non-interacting leads, thus one could ask the question: is it possible to infer physical quantities of the reservoirs from the knowledge of the molecular Green's function? In other words, is it possible to explore the back-action that the microscopic scattering system has on the macroscopic electronic leads? The answer is affirmative and we now show how this can be achieved by using the inbedding technique [60, 73, 74]. The last method allows us to find the single-particle Green's function for the electronic lead α:

$$G_{\alpha\alpha}(1,1') = -i\left\langle \mathcal{T}_\gamma \hat{c}_\alpha(1)\hat{c}^\dagger_\alpha(1')\right\rangle . \tag{2.55}$$

The equation of motion that describes the time-evolution of this quantity can be easily worked out by using the Heisenberg equations of motion for the creation and annihilation operators [60], the solution is found to satisfy the Dyson equation:

$$G_{\alpha\alpha}(1,1') = g_{\alpha\alpha}(1,1') + \int d\bar{1}d\bar{2} g_{\alpha\alpha}(1,\bar{1})\Sigma^{in}_{\alpha\alpha}(\bar{1},\bar{2})g_{\alpha\alpha}(\bar{2},1') \tag{2.56}$$

with the inbedding self-energy defined in the localized basis of the lead α as

$$\Sigma^{in}_{k\alpha l\alpha}(z,z') = \sum_{ij} T_{k\alpha i} G_{ij}(z,z') T_{jl\alpha}. \tag{2.57}$$

Here $G_{ij}(z,z')$ are the matrix elements of the interacting single-particle Green's function in the localized basis of the central microscopic region that accounts for the effects of the electron-electron (electron-phonon) interaction and the tunnel-coupling with the electronic reservoirs Eq. (2.23). It is worth noticing that the Dyson equation for the lead α Eq. (2.56) does not depend on the SPGF $G_{\alpha\alpha}(1,1')$ itself, this is due to the prior assumption that the macroscopic electronic leads are treated as non-interacting. Analogously to what we have done for the SPGF of the correlated region, we can now use the Langreth rule to project Eq. (2.56) into real-time and write down the components of the electronic lead Green's function

$$G^{R/A}_{\alpha\alpha}(t,t') = g^{R/A}_{\alpha\alpha}(t,t') + \left[g^{R/A}\cdot\Sigma^{R/A}_{in}\cdot g^{R/A}\right]_{\alpha\alpha}(t,t') \tag{2.58}$$

$$G^{\lessgtr}_{\alpha\alpha}(t,t') = g^{\lessgtr}_{\alpha\alpha}(t,t') + \Big[g^{\lessgtr}\cdot\Sigma^{A}_{in}\cdot g^{A} + g^{R}\cdot\Sigma^{\lessgtr}_{in}\cdot g^{A} + g^{R}\cdot\Sigma^{R}_{in}\cdot g^{\lessgtr} + \\ + g^{\rceil}\cdot\Sigma^{\lceil}_{in}\cdot g^{A} + g^{R}\cdot\Sigma^{\rceil}_{in}\star g^{\lceil} + g^{\rceil}\star\Sigma^{M}_{in}\star g^{\lceil}\Big]_{\alpha\alpha}(t,t') \tag{2.59}$$

once again we assume matrix multiplication among indices of the single-particle basis and the time convolutions as in Eq. (2.41). In the next section we will see how to use the inbedding technique of Eq. (2.56) to calculate the variation of energy and consequently the temperature variation of the electronic reservoirs when they are strongly coupled to a microscopic scattering region.

2.3 Generalized Kadanoff-Baym Ansatz

In the previous section we saw that to compute the time-dependent SPGF, either the Dyson equation, see Eq. (2.23), or the Kadanoff-Baym equations, see Eq. (2.19) have to be solved. Both methods, due to their inherent two-time structure, are computationally expensive with a $\mathcal{O}(N_t^3)$ scaling with the simulation duration time N_t (number of time steps). A way to reduce the computational scaling of the NEGF theory is through the so called Generalized Kadanoff-Baym Ansatz (GKBA). In its first formulation [75–79], it lowers the computational cost from cubic to quadratic by making use of the approximation that consists in replacing the two-time correlation propagator $G^{\lessgtr}(t,t')$, with the reduce one-particle density matrix $-iG^{<}(t,t)$ and the retarded propagator. Recently, a second reformulation that maps the GKBA integro-differential equations onto a coupled system of ordinary differential equations has lead to time-linear scaling of the scheme [80–82]. In what follows, we present a brief but self-contained introduction of the first formulation of the GKBA. The approximation starts by rewriting the lesser/greater component of the Dyson equation Eq. (2.40)

$$G^{\lessgtr}(t,t') = iG^{R}(t,t')G^{\lessgtr}(t',t') + \Big[G^{R}\cdot\Sigma^{\lessgtr}\cdot G^{A}\Big](t,t') + \Big[G^{R}\cdot\Sigma^{\lessgtr}\cdot G^{\lessgtr}\Big](t,t') + \\ - iG^{\lessgtr}(t,t)G^{A}(t,t') + \Big[G^{R}\cdot\Sigma^{\lessgtr}\cdot G^{A}\Big](t,t') + \Big[G^{\lessgtr}\cdot\Sigma^{A}\cdot G^{A}\Big](t,t'), \tag{2.60}$$

where we have used the Dyson equation for the retarded/advanced components Eq. (2.37) and the homogeneous differential equation for the non-interacting SPGF Eq. (2.21). Notice that, even if some advanced has been made to include the correlated initial state [83–85], here we disregard all these contributions as they are not relevant for the subject of our discussion. The GKBA is done

by only retaining the non-integral terms in the previous expression,

$$G^{\lessgtr}(t,t') \equiv iG^R(t,t')G^{\lessgtr}(t',t') - iG^{\lessgtr}(t,t)G^A(t,t'). \tag{2.61}$$

Those components enter in the real-time lesser/greater projections of the KBE,

$$\Big(i\partial_t - h(t)\Big)G^{\lessgtr}(t,t') = I^{\lessgtr}(t,t') \tag{2.62}$$

through the so-called collisional integrals:

$$I^{<}(t,t') = [\Sigma^{<}\cdot G^A + \Sigma^R\cdot G^{<}](t,t') \tag{2.63}$$

$$I^{>}(t,t') = [G^{<}\cdot \Sigma^A + G^R\cdot \Sigma^{<}](t,t'). \tag{2.64}$$

The approximation in Eq. (2.61) allows us to decouple the dynamics along the time-diagonal component from the off-diagonal one, see below. Nonetheless, the retarded and advanced propagators, that are untouched by the approximation, are still two-times functions that obey equations of similar complexity as the original KBE (cubic scaling). To bypass this problem and achieve quadratic scaling these last propagators are treated with a different approximation compared to the one of the time-propagation. In the case of a many-body open quantum system the retarded propagator satisfies the inhomogeneous equation

$$\Big(i\partial_t - h(t)\Big)G^R(t,t') = \delta(t,t') + \int d\bar{t}\,(\Sigma^R_{MB} + \Sigma^R_{emb})(t,\bar{t})G^R(\bar{t},t'), \tag{2.65}$$

if we choose the many-body self-energy at the Hartee-Fock level $\Sigma_{MB} \equiv \Sigma_{HF}$ and the embedding one within the wide band limit approximation $\Sigma^R_{emb}(t,t') = -(i/2)\Gamma\delta(t,t')$, with $\Gamma = \sum_\alpha \Gamma_{\alpha ij}$ as defined in Eq. (2.52), thanks to their time-local structure the solution for the retarded and advanced propagators are easily found to be

$$G^{R/A}(t,t') = \mp\theta[\pm(t-t')]\mathcal{T}e^{-i\int_t^{t'} d\bar{t}\,(h_{HF}(\bar{t}) - i\Gamma/2)} \tag{2.66}$$

where $h_{HF} = h + \Sigma_{HF}$. As a result of this approximation, the propagator accounts for the interaction at the mean field level as well as for dissipation induced by the presence of the macroscopic reservoirs. Higher-order correlation effects beyond the Hartree-Fock are not included into the propagator, but they can be considered into the time evolution of the lesser and greater components. The dynamics of the single-particle density matrix $\rho(t) = -iG^{<}(t,t)$, namely the lesser component of the SPGF along the time-diagonal, is given by the equation

$$\frac{d}{dt}\rho(t) + i[h_{HF}(t),\rho(t)] = -(I(t) + h.c), \tag{2.67}$$

with the collisional integral at equal-time defined as

$$I(t) = \int d\bar{t}\,[\Sigma^{>}(t,\bar{t})G^{<}(\bar{t},t') - \Sigma^{<}(t,\bar{t})G^{>}(\bar{t},t')], \tag{2.68}$$

where the exchange self-energy $\Sigma = \Sigma_{MB} + \Sigma_{emb}$ accounts for both the correlation effects beyond mean-field and coupling with the external electronic leads. Summarizing, the GKBA consists in calculating the ansatz in Eq. (2.61) with an initial seed (typically the non-interacting SPGF) and the retarded propagator in Eq. (2.66), then constructing the collisional integral in Eq. (2.68) and finding the evolution of the time-diagonal lesser and greater components Eq. (2.67) that in turn will be used to rebuild the ansatz until self-consistency is reached. Despite the limitations imposed by construction on the retarded propagator, in the original publication **V** we have shown that the GKBA is able to describe well physical quantities that strongly depend on the spectral features of the system at hand.

2.4 Non-equilibrium steady state

As we have already stated in the previous section, to find the solution of the Dyson equation is a demanding task that has a cubic scaling with the simulation time. Beside the GKBA approximation, another way to avoid the excess of computational power is to find the solution of the Dyson equation directly at the non-equilibrium steady-state (NESS). As it should be clear from its definition the NESS, whenever exists, provides only limited time-independent information about the correlated system. Thus it is not useful to study systems where the correlated initial state plays a crucial role and when the relevant physical phenomena are encoded in the short transient dynamics. However, it is of fundamental importance in transport-configurations where transport characteristics and properties like electrical, thermal conductance and other affinities are well defined and measured. The NESS is defined as the long-time limit of the Dyson equation or equivalently of the equations of motion for the SPGF. In this limit initial correlations and initial-state dependences are washed out, two-times functions in the Keldysh space, like the SPGF and the self-energies, depend on the time difference only and the equations linking them are notably simplified.
Whenever a contour-function depends on the time difference only, it possible to define its Fourier transform and conveniently express it in frequency domain

$$A(t-t') = \int \frac{d\omega}{2\pi} e^{-i\omega(t-t')} A(\omega). \tag{2.69}$$

Furthermore, the long-time limit of the convolution integral, see Eq. (2.41), can be expressed in its conventional form; it is enough to change variable under

the integral sign:

$$\begin{aligned} C(t-t') &= \int_{t_0}^{\infty} d\bar{t} A(t-\bar{t}) B(\bar{t}-t') \\ &= \int_{-\infty}^{t-t_0} d\tau A(\tau) B(t-\tau-t') \end{aligned} \tag{2.70}$$

and then taking the long-time limit $t \to \infty$ and renaming $t - t' = t$

$$C(t) = \int_{-\infty}^{\infty} d\tau A(\tau) B(t-\tau). \tag{2.71}$$

By definition, the convolution integral in time becomes a simple algebraic product in frequency domain

$$C(\omega) = A(\omega) B(\omega). \tag{2.72}$$

With those basic elements, we can now express the Dyson equation for the real-time components of the SPGF in frequency space. We starts by another exact reformulation of the Dyson equation of the lesser/greater functions Eq. (2.40) [60] that is convenient to the ends of our discussion:

$$\begin{aligned} G^{\lessgtr}(t,t') = G^R(t,t_0) G_0^{\lessgtr}(t_0,t_0) G^A(t_0,t') + \Big[\Big(G^R \cdot \Sigma^{\lessgtr} + G^{\rceil} \star \Sigma^{\lceil}\Big) \cdot G^A\Big](t,t') + \\ - i\Big[G^R \cdot \Sigma^{\rceil} \star G_0^M + G^{\rceil} \cdot \Sigma^M \star G_0^M\Big](t,t_0) G^A(t_0,t'). \end{aligned} \tag{2.73}$$

As we introduced before, for system out of equilibrium all initial-correlations and initial-state dependences are washed out in the long-time limit, thus all terms in Eq. (2.73) vanish except for the convolution $G^R \cdot \Sigma^{\lessgtr} \cdot G^A$. The latter can be straightforwardly expressed in the frequency domain as

$$G^{\lessgtr}(\omega) = G^R(\omega) \Sigma^{\lessgtr}(\omega) G^A(\omega). \tag{2.74}$$

To close the set of coupled equations needed to find the solution at the NESS, we need an equation in frequency space for the retarded/advanced components of the SPGF, that is provided by the Fourier transform of Eq. (2.37)

$$G^{R/A}(\omega) = G_0^{R/A}(\omega) + G_0^{R/A}(\omega) \Sigma^{R/A}(\omega) G^{R/A}(\omega). \tag{2.75}$$

This result allows us to calculate steady-state quantities without solving the full two-time Dyson equation and accordingly to reduce the computational cost of the simulation to a linear scaling $\mathcal{O}(N_\omega)$ with the number of frequency points N_ω.

Chapter 3

Physical Quantities

In this chapter we present a list of useful physical quantities that one could obtain within the NEGF framework. Specifically, we discuss the time-dependent single-particle quantities that require the knowledge of both the single-particle Green's function and the self-energy. We will show that two-particle quantities that depend on the two-particles Green's function, such as the energy rate flowing in and out of the central correlated region, can still be expressed in terms of the single-particle Green's function provided that the two-particles Green's function is calculated consistently with the approximation done for the self-energy. Moreover, whenever it will be useful, we will present the NESS counterpart of these quantities.

3.1 Occupation number and momentum distribution

The first physical quantity of interest is the occupation number of a given single particle state, which can be computed by means of the lesser Green's function as:

$$n_s(t) = -iG^<_{s,s}(t,t). \tag{3.1}$$

This quantity gives us information on the time-dependent occupation of the state with quantum numbers s. In the case in which the chosen basis is in the position-spin representation, namely $s = \{\mathbf{j}, \sigma\}$ where $\mathbf{j}$ labels the site position in a N-sites lattice in d-dimensions and σ the particle spin, then one can define the momentum distribution with momentum $\mathbf{k}$ as follows

$$m(\mathbf{k}) = -i\frac{1}{N}\sum_{\sigma}\sum_{j_1 j_2} e^{-i(\mathbf{j}_1-\mathbf{j}_2)\cdot\mathbf{k}} G^<_{j_1\sigma,j_2\sigma}(t,t). \tag{3.2}$$

This is particularly relevant in the case of ultracold atomic gases where the momentum distribution is a routinely measured quantity via time-of-flight

techniques.

3.2 Spectral Function

Information on the single particle spectrum are encoded in the spectral function, defined as the Fourier transform of $G^{>} - G^{<}$ with respect to the relative time coordinate $\tau = t - t'$ for a given value of the time $T = (t + t')/2$, i.e.,

$$A(T, \omega) = -\mathrm{Im} \int \frac{d\tau}{2\pi} e^{i\omega\tau} \Omega \left(T + \frac{\tau}{2}, T - \frac{\tau}{2} \right), \tag{3.3}$$

where $\Omega = \mathrm{Tr}_{\bar{C}} \left[G^{>} - G^{<} \right]$ and the trace is over all degrees of freedom not belonging to the central region (system of interest). For value of T sufficiently large, when the transient dynamics becomes negligible, and in the absence of external drivings, the spectral function becomes independent of T, namely $A(T, \omega) \to A(\omega)$. In this case, the density of states (DOS) $D(\omega) = \mathrm{Tr}_C A(\omega)$ displays peaks at the accessible single-particle energies for the central region. The spectral function also contains other information such as the momentum distribution of the system and therefore the single-particle dispersion relation due to its dependence upon the frequencies ω. The spectral function is normalized such that in the non-interacting case $\int_{-\infty}^{\infty} d\omega/(2\pi) A(\omega) = N_{sp}$, where N_{sp} is the number of single particle energy levels [60]. It is worth mentioning that the calculation of the spectral function requires the knowledge of the two-time Green's function and therefore one might believe that the information it carries are not accessible in the context of the GKBA. Actually, as we have seen in Sec. 2.3, this information has to be provided *a priori* via the ansatz on the retarded and advanced components of the Green's function Eq. (2.66). Because of this, and since so far the most used approximation is the GKBA-HF for the retarded propagator (or GKBA-HF+WBLA in the case of open system), we can include in the spectral properties of the correlated region only mean-field effects. Nonetheless, in one of the original publication **V** included in the thesis, we were able to show that the GKBA master equation, computed with an HF+WBLA propagator and a second Born self-energy, is able to capture spectral features which go beyond the mean-field approximation.

3.3 Particle currents

We have seen that, from the knowledge of the single particle Green's function of the central region Eq. (2.16) and its components along the Keldysh contour, we have access to the time-dependent ensemble average of all one-body operators of the central region. We also have access to the total current flowing between

this region and the lead α. The particle current reads

$$I_\alpha(t) = \frac{d}{dt}\left\langle \hat{N}_\alpha(t)\right\rangle = i\left\langle\left[\hat{V}_{C\alpha}(t), \hat{N}_\alpha(t)\right]\right\rangle, \tag{3.4}$$

where $\hat{N}_\alpha(t)$ is the total number of particle operator of the lead α whereas $\hat{V}_{C\alpha}(t)$ is the coupling Hamiltonian between the central region and the leads. One can easily write this expression in terms of the single particle Green's function of the central region and the embedding self-energy of the lead α by means of the equation of motion Eq. (2.19) [54, 60, 86]:

$$I_\alpha(t) = 2Re\left\{Tr\left[\Sigma^<_\alpha \cdot G^A + \Sigma^R_\alpha \cdot G^< + \Sigma^\rceil_\alpha \star G^\lceil\right](t,t)\right\} \tag{3.5}$$

The last term in Eq. (3.5) explicitly accounts for the effects of initial correlations and initial-state dependence. If one assumes that both dependencies are washed out in the limit $t \to \infty$, then for large times we can discard the imaginary-time convolution. Equation (3.5) provides a generalization to the transient time-domain of the Meir–Wingreen formula [56, 58] that in turn was the extension to interacting systems of the well-established Landauer–Büttiker formula [87, 88]. Another important expression for the current can be obtained by replacing the embedding self-energy in Eq. (3.5) with the many-body one:

$$I_{mb}(t) = 2Re\left\{Tr\left[\Sigma^< \cdot G^A + \Sigma^R \cdot G^< + \Sigma^\rceil \star G^\lceil\right](t,t)\right\}. \tag{3.6}$$

This current comes from the interaction term $\hat{V}(t)$ and has to go to zero due to the conserving nature of the approximation of the many-body self-energy. However, as we discussed above, macroscopic conservation laws hold only if self-consistency is implemented, in this case we expect that

$$\sum_\alpha I_\alpha(t) = 0 \tag{3.7}$$

and hence we can make use of Eq. (3.6) as good figure of merit for the convergence of the self-consistence procedure. For the particle currents, it is also true that the current into the lead is equal and opposite to the charge variation in the central system due to that lead, namely $I_\alpha = -I_C^{(\alpha)}$. Here we defined the current into the central region due to the lead α as $\sum_\alpha I_C^{(\alpha)} = i\langle[\hat{H}(z), \hat{N}_C(z)]\rangle_{z=t}$. This relation translates into formal mathematical expression the intuitive concept of the locality of the number operator. Basically, they state that particles flowing out of a lead necessarily enter the central region causing an equally and opposite variation.
Since in most practical situations one is interested in the transport properties when a NESS is reached, we report also here the steady-state counter part

of Eq. (3.5) that can be obtained in the long time limit by Fourier transform the Keldysh's components of the single-particle Green's function and the embedding self-energy

$$I_\alpha = 2Re \int \frac{d\varepsilon}{2\pi} Tr \left[\Sigma_\alpha^<(\varepsilon) G^A(\varepsilon) + \Sigma_\alpha^R(\varepsilon) G^<(\varepsilon) \right]. \tag{3.8}$$

Notice that the last term in Eq. (3.5) has been disregarded due to the initial state dependence of the left and right components.

3.4 Energy currents

As opposite to the charge currents, the energy currents that are present in the transport model considered here are strongly non-local. In other words, it is not true anymore that the incoming energy fluxes into the central region are equal and opposite to the ones flowing out from the metallic leads. This is mostly due to the presence of non-local interactions in the central region, as well as to the existence of a tunneling contacts between the conducting correlated island and the leads. The tunneling or contact regions can absorb and store a finite amount of energy that is not trivial to quantify. In the next sections, we present the details of the original derivation reported in the Publication **III** on how to compute the expression of the energy variation in the contact and in the central correlated region. Our main interest is focused on the relations that occur between all the different contributions to the energy currents in the reservoirs, in the central interacting region and in the tunneling barrier. For such purposes, we evaluate the time derivative of each component of the total Hamiltonian (2.1), which are given by

$$J_\alpha(t) \equiv \frac{d}{dt} \left\langle \hat{H}_\alpha(t) \right\rangle = i \left\langle [\hat{H}(t), \hat{H}_\alpha(t)] \right\rangle + \frac{\partial \langle \hat{H}_\alpha(t) \rangle}{\partial t}, \tag{3.9}$$

$$J_C(t) \equiv \frac{d}{dt} \left\langle \hat{H}_C(t) \right\rangle = i \left\langle [\hat{H}(t), \hat{H}_C(t)] \right\rangle + \frac{\partial \langle \hat{H}_C(t) \rangle}{\partial t}, \tag{3.10}$$

$$\dot{\mathcal{E}}_{C\alpha}(t) \equiv \frac{d}{dt} \left\langle \hat{V}_{C\alpha}(t) \right\rangle = i \left\langle [\hat{H}(t), \hat{V}_{C\alpha}(t)] \right\rangle + \frac{\partial \langle \hat{V}_{C\alpha}(t) \rangle}{\partial t}, \tag{3.11}$$

the last terms in the r.h.s. of these equations are the power injected by the explicit time-dependent drives present in the Hamiltonian. In the following, we disregard those terms as they are not relevant for the overall discussion and they can be easily added back when the shapes of the external time-dependent pulses are known. Besides, the different contributions to the energy currents are linked because of the conservation of the total energy, which is given mathematically by

$$i \left\langle [\hat{H}(t), \hat{H}(t)] \right\rangle = 0 = \sum_\alpha J_\alpha(t) + J_C(t) + \sum_\alpha \dot{\mathcal{E}}_{C\alpha}(t). \tag{3.12}$$

The first energy current we encounter is the rate of change of the energy in the non-interacting electron reservoirs, its expression in terms of the single-particle Green's function and embedding self-energy can be worked out easily in a similar manner to what is done for the particle current [54, 58, 89]

$$J_\alpha(t) = 2Re\left\{ Tr\left[i\frac{d\Sigma_\alpha^<}{dt}\cdot G^A + i\frac{d\Sigma_\alpha^R}{dt}\cdot G^< + i\frac{d\Sigma_\alpha^\rceil}{dt}\star G^\lceil \right](t,t)\right\}. \tag{3.13}$$

The main difference with Eq. (3.5) is the presence of the time-derivative of the embedding self-energy, this is a consequence of the fact that all the terms in the expression for the energy current are weighted by the single particle Hamiltonian of the α-th lead. Eq. (3.13) contains the physical effect of the energy carried by the flowing particles and, as it is clear from its expression, is not a simple manageable quantity due to the presence of the time derivative of the embedding self-energy. However, its NESS counter part has a very handy expression and has been widely used to study transport and thermoelectro effects in different physical systems [89–94]

$$J_\alpha = 2Re\int \frac{d\varepsilon}{2\pi}\,\varepsilon\, Tr\left[\Sigma_\alpha^<(\varepsilon)G^A(\varepsilon) + \Sigma_\alpha^R(\varepsilon)G^<(\varepsilon)\right]. \tag{3.14}$$

Once again the difference between this expression and the one for the charge current, see Eq. (3.8), is the presence of the energy of the α-th lead.

3.4.1 Energy variation of the central region

In this section, we show how to compute the variation of energy in the interacting central island. As we have seen before, the energy variation of the central region is nothing but the Heisenberg equation of motion for the Hamiltonian of the central part of the total system:

$$J_C(t) \equiv \frac{d}{dt}\left\langle \hat{H}_C(t)\right\rangle = i\left\langle [\hat{H}(t), \hat{H}_C(t)]\right\rangle.$$

We will show that this quantity can be recast in terms of the single-particle Green's function, the embedding and the many-body self-energy in a form very similar to the time dependent Meir-Wingreen expression for the particle current [56, 58, 86]. To achieve this, we proceed in steps and we begin by showing how the energy variation can be expressed in terms of single- and two-particle mixed Green's functions, i.e., we prove that the energy variation is indeed a two-particles quantity. Even though the quantities we are interested in are real-time quantities we carry the calculation along the imaginary time contour to lighten the already cumbersome and lengthy expressions. Firstly,

we compute explicitly the commutators entering into the definition of the energy current:

$$
\begin{aligned}
&J_C(t) = i\left\langle[\hat{H}(z_1), \hat{H}_C(z_1)]\right\rangle = i\left\langle[\hat{V}_{C\alpha}(z_1), \hat{H}_C(z_1)]\right\rangle \\
&= \sum_\alpha\Big(-i\int d\mathbf{x}_1\; T(1)h(1)\left\langle\hat{\psi}^\dagger(1)\hat{\psi}_\alpha(1)\right\rangle + i\int d\mathbf{x}_1\; T^*(1)h(1)\left\langle\hat{\psi}^\dagger_\alpha(1)\hat{\psi}(1)\right\rangle + \\
&- \frac{i}{2}\int_\gamma dz_1'\int\int d\mathbf{x}_1 d\mathbf{x}_1'\; T(1')v(1,1')(-i)^2\left\langle\hat{\psi}^\dagger(1)\hat{\psi}^\dagger(1')\hat{\psi}(1)\hat{\psi}_\alpha(1')\right\rangle + \\
&+ \frac{i}{2}\int_\gamma dz_1'\int\int d\mathbf{x}_1 d\mathbf{x}_1'\; T(1)v(1,1')(-i)^2\left\langle\hat{\psi}^\dagger(1)\hat{\psi}^\dagger(1')\hat{\psi}(1')\hat{\psi}_\alpha(1)\right\rangle + \\
&- \frac{i}{2}\int_\gamma dz_1'\int\int d\mathbf{x}_1 d\mathbf{x}_1'\; T^*(1)v(1,1')(-i)^2\left\langle\hat{\psi}^\dagger_\alpha(1)\hat{\psi}^\dagger(1')\hat{\psi}(1')\hat{\psi}(1)\right\rangle + \\
&+ \frac{i}{2}\int_\gamma dz_1'\int\int d\mathbf{x}_1 d\mathbf{x}_1'\; T^*(1')v(1,1')(-i)^2\left\langle\hat{\psi}^\dagger_\alpha(1')\hat{\psi}^\dagger(1)\hat{\psi}(1')\hat{\psi}(1)\right\rangle\Big)
\end{aligned}
\tag{3.15}
$$

where again z is the complex time variable on the path γ in the complex-time plane and $1 \equiv (\mathbf{x}_1, z_1)$, $2 \equiv (\mathbf{x}_2, z_2)$ and $1' \equiv (\mathbf{x}_1', z_1')$ are multi-indexes for position, spin and complex time. At the end of the calculations, we take $z_1 = t$ to project the complex time variable onto the real axis. We can rewrite the first two terms in the following way

$$
\begin{aligned}
&\int d\mathbf{x}_1\; h(1)\left[T^*(1)i\left\langle\hat{\psi}^\dagger_\alpha(1)\hat{\psi}(1)\right\rangle - T(1)i\left\langle\hat{\psi}^\dagger(1)\hat{\psi}_\alpha(1)\right\rangle\right] = \\
&= 2Re\Big\{\int d\mathbf{x}_1\; h(1)T^*(1)G_{C\alpha}(1;1^+)\Big\}
\end{aligned}
\tag{3.16}
$$

where we use the definition of the mixed Green's functions: $G_{C\alpha}(1,1') = -i\left\langle\mathcal{T}_\gamma\hat{\psi}(1)\hat{\psi}^\dagger_\alpha(1')\right\rangle$ and $G_{\alpha C}(1;1') = -i\left\langle\mathcal{T}_\gamma\hat{\psi}_\alpha(1)\hat{\psi}^\dagger(1')\right\rangle$, with $\mathcal{T}_\gamma$ the time-ordering operator over the Keldysh contour γ and where we exploit the property $G_{\alpha C}(1;1') = -[G_{C\alpha}(1';1)]^*$. Moreover $1^+ \equiv (\mathbf{x}_1, z_1^+)$ with z_1^+ being a time infinitesimally greater than z_1 on the Keldysh contour. A similar manipulation can be done in the other four terms arising from the commutator of the interacting Hamiltonian. By a change of the integration variables, and using the relation $\left\langle\hat{\psi}^\dagger(1)\hat{\psi}^\dagger(1')\hat{\psi}(1')\hat{\psi}_\alpha(1)\right\rangle = -\left\langle\hat{\psi}^\dagger(1')\hat{\psi}^\dagger(1)\hat{\psi}(1')\hat{\psi}_\alpha(1)\right\rangle$, the last four terms are equal in pairs, this cancels out the factor 1/2 and we are

left with:

$$
\begin{aligned}
& i\int_\gamma dz_1' \int\int d\mathbf{x}_1 d\mathbf{x}_1'\; T_\alpha^*(1')v(1,1')(-i)^2\left\langle \hat{\psi}_\alpha^\dagger(1')\hat{\psi}^\dagger(1)\hat{\psi}(1')\hat{\psi}(1)\right\rangle + h.c. \\
& = 2Re\Big\{ i\int_\gamma dz_1' \int\int d\mathbf{x}_1 d\mathbf{x}_1'\; v(1,1')T_\alpha^*(1')G^{(2)}_{CCC\alpha}(1',1;1^+,1'^+)\Big\},
\end{aligned}
\tag{3.17}
$$

where we use the definition of the mixed two-particle Green's functions

$$
G^{(2)}_{CCC\alpha}(1,2;3,4) = (-i)^2\left\langle \mathcal{T}_\gamma \hat{\psi}(1)\hat{\psi}(2)\hat{\psi}_\alpha^\dagger(4)\hat{\psi}^\dagger(3)\right\rangle, \tag{3.18}
$$

$$
G^{(2)}_{C\alpha CC}(1,2;3,4) = (-i)^2\left\langle \mathcal{T}_\gamma \hat{\psi}(1)\hat{\psi}_\alpha(2)\hat{\psi}^\dagger(4)\hat{\psi}^\dagger(3)\right\rangle, \tag{3.19}
$$

together with the relation $G^{(2)}_{C\alpha CC}(1,1';1'^+,1^+) = \left[G^{(2)}_{CCC\alpha}(1',1;1^+,1'^+)\right]^*$. By collecting all terms we obtain:

$$
\begin{aligned}
J_C(t) = \sum_\alpha 2Re\Big\{ & \int d\mathbf{x}\; h(1)T^*(1)G_{C\alpha}(1^+) + \\
& + i\int_\gamma dz' \int\int d\mathbf{x}d\mathbf{x}'\; v(1;1')T_\alpha^*(1')G^{(2)}_{CCC\alpha}(1',1;1^+,1'^+)\Big\}.
\end{aligned}
\tag{3.20}
$$

In the following, we demonstrate how to manipulate these expressions in order to recast them in terms of single-particle quantities of the central region. We have seen in Eq. (3.20) that it is possible to express the energy current flowing through the middle interacting part of the total system as the sum of two terms. These terms contain the mixed Green's functions accounting for the propagation of both particles in the central region and in the leads. It is important to realize that a similar situation occurs for the calculation of the particle (charge) current [86]. The usual way to find an expression for the mixed Green's functions $G^{C\alpha}(1;1')$ is based on the equation-of-motion approach [54, 60]. Since the leads are treated as non-interacting, the method allows to write down a closed set of equations and then a general formula for $G^{C\alpha}(1;1')$ in terms of the single particle Green's function. Even though appealing for its conceptual simplicity, the equation-of-motion technique cannot straightforward be applied to the mixed two-particle Green's function $G_2^{CCC\alpha}(1,2;3,4)$ since the analysis and the calculations gets quite involved and a closed set of equations can be found only if one relies on some physical approximations. The latter must be chosen consistently with the approximations used for the single-particle Green's function.
Rather than the equations-of-motion technique we find a general expression

for both, single and two particles mixed Green's functions, by a direct expansion of the S-matrix in the interaction picture with respect to the coupling Hamiltonian [54]. Despite the fact that the derivation is somehow more elaborate for the mixed single-particle Green's function, it is very general and can be extended easily to the mixed n-particle Green's functions. To begin with, we look at the first term of the energy current, namely the one containing the single-particle Hamiltonian $h(1)$. To unfold once more the main idea of this approach, we want to express the contour-ordered mixed single-particle Green's function $G_{C\alpha}(1;1') = -i\left\langle \mathcal{T}_\gamma \hat{\psi}(1)\hat{\psi}^\dagger_\alpha(1')\right\rangle$ in terms of both the contour-ordered single particle Green's function of the particles in the central region $G_{CC}(1;1') = -i\left\langle \mathcal{T}_\gamma \hat{\psi}(1)\hat{\psi}^\dagger(1')\right\rangle$, and the one in the leads $g_\alpha(1;1') = -i\left\langle \mathcal{T}_\gamma \hat{\psi}_\alpha(1)\hat{\psi}^\dagger_\alpha(1')\right\rangle$.
The derivation follows by writing the Green's function $G_{C\alpha}(1;1')$ in terms of the interaction-picture operators (denoted by a tilde) with respect to the free Hamiltonians $\hat{H}_C$ and $\hat{H}_\alpha$ of both the central region and the lead α . Accordingly, the evolution operator is expressed in terms of the coupling Hamiltonian $\tilde{V}_{C\alpha}$ in the interaction picture. Thus, in this picture the mixed single-particle Green's function can be written as:

$$G_{C\alpha}(1;1') = -i\left\langle \mathcal{T}_\gamma \hat{\psi}(1)\hat{\psi}^\dagger_\alpha(1')\right\rangle = -i\left\langle \mathcal{T}_\gamma \tilde{\psi}(1)\tilde{\psi}^\dagger_\alpha(1')S\right\rangle, \tag{3.21}$$

where we introduce the S-matrix as:

$$S = \sum_{k=0}^{\infty}\frac{(-i)^k}{k!}\int_\gamma d\bar{z}_1\cdots\int_\gamma d\bar{z}_k \tilde{V}_{C\alpha}(\bar{1})\ldots\tilde{V}_{C\alpha}(\bar{k}). \tag{3.22}$$

By inserting the explicit form of the S-matrix into Eq. (3.21) we obtain

$$\begin{aligned} G_{C\alpha}(1;1') = -i\Big\langle \mathcal{T}_\gamma \tilde{\psi}(1)\tilde{\psi}^\dagger_\alpha(1')\sum_{k=0}^{\infty}\frac{(-i)^k}{k!}\times \\ \times\int_\gamma\int d\bar{z}_1 d\bar{\mathbf{x}}_1\left(\tilde{\psi}^\dagger(\bar{1})T(\bar{1})\tilde{\psi}_\alpha(\bar{1}) + h.c.\right)\times\cdots\times\int_\gamma d\bar{z}_k\tilde{V}_{C\alpha}(\bar{k})\Big\rangle \\ = \int d\bar{1}\sum_{k=0}^{\infty}\frac{(-i)^k}{k!}(-i)\left\langle \mathcal{T}_\gamma\tilde{\psi}_\alpha(\bar{1})\tilde{\psi}^\dagger_\alpha(1')\right\rangle T(\bar{1})\times \\ \times\left\langle \mathcal{T}_\gamma\tilde{\psi}(1)\tilde{\psi}^\dagger(\bar{1})\times\cdots\times\int_\gamma d\bar{z}_k\tilde{V}_{C\alpha}(\bar{k})\right\rangle + (k-1 \text{ remaining terms}) \end{aligned} \tag{3.23}$$

The crucial element in the second step of the calculation is the assumption that the leads are non-interacting, this allows us to use the Wick's theorem for the α-operators. Besides, in the interaction picture the operators ψ and ψ_α

are independent and thus we can factorize the expectations values. Finally, by relabeling all integration variables in the remaining $k-1$ terms we notice that all these terms are equal and hence we get a factor k, therefore:

$$\begin{aligned} G_{C\alpha}(1;1') &= \int d\bar{1} T_\alpha(\bar{1})(-i)\left\langle \mathcal{T}_\gamma \tilde{\psi}_\alpha(\bar{1})\tilde{\psi}^\dagger_\alpha(1')\right\rangle \times \\ &\times (-i)\left\langle \mathcal{T}_\gamma \tilde{\psi}(1)\tilde{\psi}^\dagger(\bar{1})\sum_{k=0}^{\infty}\frac{(-i)^{k-1}}{(k-1)!}\prod_{p=1}^{k}\int_\gamma d\bar{z}_p \tilde{V}_{C\alpha}(\bar{p})\right\rangle \\ &= \int d\bar{1}\; G(1;\bar{1})T_\alpha(\bar{1})g_\alpha(\bar{1};1'), \end{aligned} \tag{3.24}$$

where in the last line we use $\hat{\psi}_\alpha(1) = \tilde{\psi}_\alpha(1)$, and restore the S-matrix expansion for the single particle Green's function. The first term in Eq.(3.20) can be rewritten as:

$$\begin{aligned} &\sum_\alpha 2Re\Big\{\int d\mathbf{x}_1 h(1)T^*_\alpha(1)G_{C\alpha}(1;1^+)\Big\} = \\ &= \sum_\alpha 2Re\Big\{\int d\mathbf{x}_1 d\bar{1}\; h(1)G(1;\bar{1})\Sigma_\alpha(\bar{1};1^+)\Big\}, \end{aligned} \tag{3.25}$$

where we use the definition of the embedding self-energy as in Eq. (2.49) $\Sigma_\alpha(1;2) = T_\alpha(1)g_\alpha(1;2)T^*_\alpha(2)$. The second term of Eq.(3.20), containing the mixed two-particle Green's function $G^{(2)}_{CCC\alpha}$, can be manipulated in a similar manner and thus can be rewritten in terms of the contour-ordered two-particle Green's function of the central interacting region $G^{(2)}$:

$$\begin{aligned} G^{(2)}_{CCC\alpha}(1',1;1^+,1'^+) &= (-i)^2\left\langle \mathcal{T}_\gamma \hat{\psi}(1')\hat{\psi}(1)\hat{\psi}^\dagger_\alpha(1'^+)\hat{\psi}^\dagger(1^+)\right\rangle \\ &= (-i)^2\left\langle \mathcal{T}_\gamma \tilde{\psi}(1')\tilde{\psi}(1)\tilde{\psi}^\dagger_\alpha(1'^+)\tilde{\psi}^\dagger(1^+)S\right\rangle \\ &= (-i)^2\Big\langle \mathcal{T}_\gamma \tilde{\psi}(1')\tilde{\psi}(1)\tilde{\psi}^\dagger_\alpha(1'^+)\tilde{\psi}^\dagger(1^+)\times \\ &\times \sum_{k=0}^{\infty}\frac{(-i)^k}{k!}\int_\gamma\int d\bar{1}\left(\tilde{\psi}^\dagger(\bar{1})T(\bar{1})\tilde{\psi}_\alpha(\bar{1}) + h.c.\right)\times\cdots\times\int_\gamma d\bar{z}_k\tilde{V}_{C\alpha}(\bar{k})\Big\rangle \\ &= \int d\bar{1}\;(-i)^2\left\langle \mathcal{T}_\gamma \tilde{\psi}(1')\tilde{\psi}(1)\tilde{\psi}^\dagger(\bar{1})\tilde{\psi}^\dagger(1^+)\sum_{k=0}^{\infty}\frac{(-i)^k}{k!}\prod_{p=1}^{k}\int_\gamma dz_p\tilde{V}_{C\alpha}(\bar{p})\right\rangle \times \\ &\times (-i)\left\langle \mathcal{T}_\gamma \tilde{\psi}_\alpha(\bar{1})\tilde{\psi}^\dagger_\alpha(1'^+)\right\rangle T(\bar{1}) \\ &= \int d\bar{1}\; G^{(2)}(1',1;1^+,\bar{1})T(\bar{1})g_\alpha(\bar{1};1'^+) \end{aligned} \tag{3.26}$$

where in the last step we recognize the series expansion in the interaction picture of the two-particle Green's function of the central region and the single-particle Green's function of the lead α. Inserting this result into the second term of Eq. (3.20) we obtain:

$$\begin{aligned} & i\sum_{\alpha}\int d\mathbf{x}'d1\; v(1',1)T^{*}(1')G^{(2)}_{CCC\alpha}(1',1;1^{+},1'^{+}) = \\ & = i\sum_{\alpha}\int d\mathbf{x}'d1d\bar{1}\; v(1',1)T^{*}(1')G^{(2)}(1',1;1^{+},\bar{1})T(\bar{1})g_{\alpha\alpha}(\bar{1};1'^{+}) \\ & = -i\sum_{\alpha}\int d\mathbf{x}'d1d\bar{1}\; v(1',1)G^{(2)}(1',1;\bar{1},1^{+})T(\bar{1})g_{\alpha}(\bar{1};1'^{+})T^{*}(1') \\ & = \sum_{\alpha}\int d\mathbf{x}'d1d\bar{1}\; \Sigma(1';1)G(1;\bar{1})\Sigma_{\alpha}(\bar{1};1'^{+}) \end{aligned} \tag{3.27}$$

where we use $v(1,1') = v(1',1)$, the symmetry relations of the two-particle Green's function $G^{(2)}(1,2;3,4) = -G^{(2)}(1,2;4,3)$ and the definition of the embedding self-energy $\Sigma_{\alpha}(1;2)$. The fundamental step in obtaining the result above is to use the relation linking the two-particle Green's function in the interacting region with the many-body self-energy Eq. (2.18):

$$\int d\bar{1}\; v(1,\bar{1})G^{(2)}(1,\bar{1};1',\bar{1}^{+}) = i\int d\bar{1}\; \Sigma(1,\bar{1})G(\bar{1},1'), \tag{3.28}$$

which is nothing but the relation which defines the many-body self-energy itself. Now we have all the ingredients to write down the final expression in terms of the currents, which combined with Eq. (3.10) gives:

$$\begin{aligned} & J_{C}(t) = \sum_{\alpha} J_{C}^{(\alpha)}(t) \\ & \equiv \sum_{\alpha} 2Re\Big\{\int d\mathbf{x}_1 d\bar{1}d\bar{2}\Big[h(1)\delta(1,\bar{1}) + \Sigma(1;\bar{1})\Big]G(\bar{1};\bar{2})\Sigma_{\alpha}(\bar{2},1^{+})\Big\}_{z_1=t}. \end{aligned} \tag{3.29}$$

To verify the correctness of our derivation, we have compared the expression for the variation of the energy Eq. (3.29) with the derivative of the total energy that in the NEGF formalism reads:

$$\frac{d}{dt}\mathcal{E}_{C}(t) = \frac{d}{dz_1}\left[i\int d\mathbf{x}_1 d\bar{1}\;\left[h(1)\delta(1,\bar{1}) + \frac{1}{2}\Sigma(1;\bar{1})\right]G(\bar{1};1^{+})\right]\Big|_{z_1=t}. \tag{3.30}$$

Even though at first glance these last two equations look similar, a careful reader will notice a fundamental and non trivial difference: Eq. (3.29) takes into account how each individual lead influences the energy transport in the

central correlated region and thus gives information on how the energy variation changes due to the different leads's contributions. On the contrary, Eq. (3.30) accounts for the rate of the total energy that cannot distinguish from the various weights coming from the different leads.

3.4.2 Energy variation of the contact region

Here we show how to compute the variation of energy in the contact region. Instead of considering directly the commutator Eq. (3.11), we exploit some useful identities that make the calculation faster and straightforward. The average variation of energy in the tunneling region then reads:

$$\begin{aligned}\frac{d}{dt}\langle \hat{V}_{C\alpha}(t)\rangle &= 2Re\left\{-i\int d\mathbf{x}_1\; T^*_\alpha(1)\frac{d}{dz_1}G_{C\alpha}(1;1^+)\right\}_{z_1=t}\\ &= 2Re\left\{\int d\mathbf{x}_1 d\bar{1}\; G(1;\bar{1})\Sigma_\alpha(\bar{1};1^+)h_\alpha(1)\right\}_{z_1=t}+\\ &- 2Re\left\{\int d\mathbf{x}_1 d\bar{1}d\bar{2}\Big[h(1)\delta(1,\bar{1})+\Sigma(1;\bar{1})\Big]G(\bar{1};\bar{2})\Sigma_\alpha(\bar{2},1^+)\right\}_{z_1=t}+\\ &- 2Re\left\{\int d\mathbf{x}_1 d\bar{1}d\bar{2}\;\Sigma_{emb}(1;\bar{1})G(\bar{1};\bar{2})\Sigma_\alpha(\bar{2},1^+)\right\}_{z_1=t},\end{aligned} \tag{3.31}$$

where we use Eq. (3.24) together with the equation of motion for the single particle Green's functions in the central region and in the leads:

$$i\frac{d}{dz}G(1;1') = \delta(1,1') + h(1)G(1;1') + \int d\bar{1}\;\left(\Sigma(1;\bar{1})+\Sigma_{emb}(1;\bar{1})\right)G(\bar{1};1') \tag{3.32}$$

$$i\frac{d}{dz'}g_\alpha(1;1') = -\delta(1,1') - g_\alpha(1;1')h_\alpha(1'), \tag{3.33}$$

and where $\Sigma_{emb}(1;1') = \sum_\beta \Sigma_\beta(1;1')$. It is easy to recognize the nature of the different contributions: the first term is nothing but the opposite of the variation of the energy of the lead α, $J_\alpha(t) = \frac{d}{dt}\langle \hat{H}_\alpha(t)\rangle$ Eq. (3.13). The second term is $-J_C^{(\alpha)}(t)$, see Eq. (3.29), namely the opposite of the variation of the energy on the central region due to the coupling with the lead α. The last term describes the direct coupling between the lead α and all the others leads. This is a very interesting and peculiar situation, indeed we have a scenario where the coupling between the leads is mediated by the central region and therefore of the fourth order in the coupling between the central region and the leads. To see it explicitly, we consider the mixed single particle Green's

function $G_{\beta\alpha}(1;1') \equiv -i\left\langle \mathcal{T}_\gamma \hat{\psi}_\beta(1)\hat{\psi}^\dagger_\alpha(1')\right\rangle$ and use once again the S-matrix expansion:

$$\begin{aligned} G_{\beta\alpha}(1;1') \equiv & \int d\bar{1}d\bar{2}\ (-i)\left\langle \mathcal{T}_\gamma \tilde{\psi}_\beta(1)\tilde{\psi}^\dagger_\beta(\bar{1})\right\rangle T^*_\beta(\bar{1})\ T_\alpha(\bar{2})(-i)\left\langle \mathcal{T}_\gamma \tilde{\psi}_\alpha(\bar{2})\tilde{\psi}^\dagger_\alpha(1')\right\rangle \times \\ & \times (-i)\left\langle \mathcal{T}_\gamma \tilde{\psi}(\bar{1})\tilde{\psi}^\dagger(\bar{2})\sum_{k=0}^{\infty}\frac{(-i)^k}{k!}\prod_{p=1}^{k}\int_\gamma dz_p \tilde{H}_T(\bar{p})\right\rangle \\ & = \int d\bar{1}d\bar{2}\ g_\beta(1;\bar{1})T^*_\beta(\bar{1})G(\bar{1};\bar{2})T_\alpha(\bar{2})g_\alpha(\bar{2};1'). \end{aligned} \tag{3.34}$$

Physically this term represents exactly the scattering of a particle (or a hole) from the lead α to the lead β through the central region. It is now easy to see that the third term in Eq. (3.31) can be written as:

$$\begin{aligned} & \int d\mathbf{x}_1 d\bar{1}d\bar{2}\ \Sigma_{emb}(1;\bar{1})G(\bar{1};\bar{2})\Sigma_\alpha(\bar{2},1^+) = \\ & = \int d\mathbf{x}_1 d\bar{1}d\bar{2}\ \sum_\beta T_\beta(1)g_\beta(1;\bar{1})T^*_\beta(\bar{1})\ G(\bar{1};\bar{2})\ T_\alpha(\bar{2})g_\alpha(\bar{2};1^+)T^*_\alpha(1) \\ & = \int d\mathbf{x}_1 \sum_\beta T_\beta(1)G_{\beta\alpha}(1;1^+)T^*_\alpha(1). \end{aligned} \tag{3.35}$$

It is simple to check that the term $\beta = \alpha$ does not contribute since it is purely imaginary. Finally, we can recast Eq. (3.31) as

$$\dot{\mathcal{E}}_{C\alpha}(t) = \frac{d}{dt}\langle \hat{V}_{C\alpha}(t)\rangle = -J_\alpha(t) - J^{(\alpha)}_C(t) - \Delta J_\alpha(t), \tag{3.36}$$

where $\Delta J_\alpha(t) = \sum_{\beta\neq\alpha}\int d\mathbf{x}_1 T_\beta(1)G_{\beta\alpha}(1;1^+)T^*_\alpha(1)$. Accordingly to authors of Ref. [95], it has been shown that the DC component of Eq. (3.36) is $\dot{\mathcal{E}}_{C\alpha}(t) = 0$ and thus

$$J_\alpha(t) = -J^{(\alpha)}_C(t) - \Delta J_\alpha(t). \tag{3.37}$$

This interesting result tells us that the variation of the energy of the α-th lead is not necessarily accompanied by an equal and opposite change in the energy of the central region. The difference between the two is given by the term $\Delta J_\alpha(t)$, which arises from the direct propagation of particles from any other of the leads, let us say β, to the lead α via virtual scattering through the central region. This interpretation is supported by the physical meaning of Eq. (3.34), it represents the propagation of a particle from one lead to another through the central system. The expression $\Sigma_{\beta\alpha}(1;1') = T^*_\beta(1)G(1;1')T_\alpha(1')$ is the

inbedding self-energy of Eq. (2.57) introduced in Sec. 2.2.4 and accounts for the back-action that the correlated island has onto the non-interacting leads. This term is usually either negligible or zero altogether. In the weak coupling limit this term is vanishingly small due to the fact that it is of fourth order in the coupling between the central region and the leads. Moreover, it also vanishes when the two integrals in the expression for $G_{\beta\alpha}(1;1')$ have different spatial supports, namely when $T_\alpha(1)$ and $T_\beta(1')$ for $\alpha \neq \beta$ are non-zero on different spatial regions and therefore their product vanishes.
Nonetheless, it is possible to envisage situations in which this term gives a non-vanishing contribution: short quantum wires (mean free path comparable with the size of the wire), more than one lead coupled to the same spatial region or spatially extended coupling between the leads and the central region. As an example where this term is not negligible, we have studied its effect in the original article **III** in an interacting quantum dot in the Kondo regime.

3.5 Effective electronic leads temperatures

In this section we describe how to use the inbedding technique introduced in Sec. 2.2.4 to extract physical information about the macroscopic electronic leads. In particular, we are interested in the variations of temperature and chemical-potential that the metallic reservoirs experience when they are in contact with the correlated region. In other words, if we start from an initial equilibrium state for the mode k in the leads α described by a Fermi-Dirac distribution $f(\varepsilon, \mu_{k\alpha}, T_{k\alpha}) = 1/(e^{(\varepsilon-\mu_{k\alpha})/k_b T_{k\alpha}} + 1)$, with initial temperature $T_{k\alpha}$ and chemical-potential $\mu_{k\alpha}$, what is the effects of the back-action that the presence of the interacting region has on this distribution? The question is conceptually challenging and surely does not have a commonly agreed answer in the scientific community. The reason is rooted on the simple observation that, after the interaction with the central region, the macroscopic lead would reach a non-equilibrium state and thus would not posses any of the properties that characterize the thermodynamic equilibrium. One possible solution to solve this conundrum is to resort to the so called hot-electron assumption. This assumption presumes that recombination and relaxation processes in the lead distribution happen very quickly due to a longer particles dispersion time compared to the interaction time in the correlated region. In what follows, we will see how combining the hot-electron assumption and the inbedding technique it is possible to extract the effective electronic temperatures of metallic reservoirs in typical transport configuration. From the lesser component of the SPGF of the lead α Eq. (2.59), we can extract some relevant quantities of the electronic leads such as the average number of particles and energy of the

mode k in the contact α under non-equilibrium steady-state condition:

$$N_{k\alpha} = -i \int \frac{d\varepsilon}{2\pi} G^{<}_{k\alpha}(\varepsilon), \tag{3.38a}$$

$$E_{k\alpha} = -i \int \frac{d\varepsilon}{2\pi} \varepsilon G^{<}_{k\alpha}(\varepsilon), \tag{3.38b}$$

with $G^{<}_{k\alpha}(\varepsilon)$ the Fourier transform of $G^{<}_{k\alpha}(t,t')$. Since the mean electron leakage-time from the leads is longer than the electron-electron scattering-time in the central system, it is valid to assume a fast relaxation in the leads distributions. In such a way, it is reasonable to consider a quasiequilibrium Fermi-Dirac distribution for the leads $f(\varepsilon, \mu'_{k\alpha}, T'_{k\alpha}) = 1/(e^{(\varepsilon-\mu'_{k\alpha})/k_b T'_{k\alpha}} + 1)$, with well-defined electronic temperature and chemical potential $T'_{k\alpha}$ and $\mu'_{k\alpha}$. Thus, with the constrains imposed by Eq. (3.38) and the hypothesis of the quasiequilibrium distributions, we can construct the following non-linear system of equations:

$$N_{k\alpha} \equiv \int \frac{d\varepsilon}{2\pi} f(\varepsilon, \mu'_{k\alpha}, T'_{k\alpha}), \tag{3.39a}$$

$$E_{k\alpha} \equiv \int \frac{d\varepsilon}{2\pi} \varepsilon f(\varepsilon, \mu'_{k\alpha}, T'_{k\alpha}). \tag{3.39b}$$

The solutions of these equations are the new temperatures and chemical potentials of the leads due to the presence of the correlated scattering region. In the publication **IV** included in the thesis, we have used this method to simulate and predict the lead electronic temperatures in a quantum dot junction and we have obtained a remarkable agreement with the measured one. This confirms the fact that, even if the hot-electron assumption imposes a strong hypothesis on the relaxation process in the metallic leads, it is possible to envisage physical implementations where these effects are present and can be measured.

Chapter 4

Numerical implementation

In this chapter we discuss the details of the numerical implementation for the self-consistent solution of the Dyson equations for the real-time components of the single-particle Green's function Eqs. (2.36)-(2.40). The main idea of this chapter is to give the reader a brief overview of the numerical procedures underlying the solution of these equations on the Keldysh contour. In particular, we present a detailed method based on the numerical *inversion* scheme on the full two-time plane. As we have already stated, finding the solution through this procedure is completely equivalent to find the solution of the most standard Kadanoff-Baym equations [42, 69], see Eq. (2.19), employing well tested two-times propagation schemes (time-stepping technique) [43, 44, 59, 60].
We start the discussion by reviewing the numerical representation on the discretized contour time-interval of all fundamental quantities and their relations to the NEGF formalism. We then underline the main steps to implement the self-consistent scheme as discussed in Sec. 2.2.1, and finally we show how a proper distributed-memory parallelization over the space/momentum degrees of freedom allows for large-scale simulations. Furthermore, we provide a short summary of the structure of our open source software/library, currently under development, which implements tools for basic operations on the non-equilibrium Green's functions, the construction of the self-energies, and for the solution of integral equations involving contour Green's functions [96, 97].

4.1 Discretization of the contour time arguments

To solve numerically the system of Dyson equations (SyDEs) Eqs. (2.36)-(2.40), we need to discretize the time intervals on both the horizontal $t \in [t_0, t_f]$ and vertical $\tau \in [0, \beta]$ branches of the contour. We choose to divide the real axis into (N_t+1) equidistant point $t \to t_n = ndt$, $n = 0, \ldots, N_t$, whereas we use the following samples for the Matsubara branch $\tau \to \tau_n = nd\tau$, $n = 0, \ldots, N_\tau$,

with $\tau_{N_\tau} = \beta^{-1}$. The numerical representation of a generic function $A(t,t')$ appearing in the system of Dyson equations has a matrix structure that comes from the finite-dimensional single-particle basis made of N_s orbitals for the discrete representation of the spatial-spin (or momentum) degrees of freedom, as well as it acquires an extra matrix form due to the time discretization: $A(t,t') \to A(t_n,t'_n) \equiv A_{nn'}$ (similarly for functions with time arguments on the vertical axis and mixed time arguments). The overall or *global* structure of a generic two-time function can be thought as $N_t \times N_t$ matrix partitioned in blocks having spatial dimension $N_s \times N_s$:

$$A = \begin{bmatrix} A_{11} & A_{12} & \cdots & A_{1N_t} \\ A_{21} & A_{22} & \cdots & A_{2N_t} \\ \vdots & \vdots & \ddots & \vdots \\ A_{N_t1} & A_{N_t2} & \cdots & A_{N_tN_t} \end{bmatrix} \qquad A_{ij} = \begin{bmatrix} a_{11} & a_{12} & \cdots & a_{1N_s} \\ a_{21} & a_{22} & \cdots & a_{2N_s} \\ \vdots & \vdots & \ddots & \vdots \\ a_{N_s1} & a_{N_s2} & \cdots & a_{N_sN_s} \end{bmatrix}. \tag{4.1}$$

Thus, due to the basis and discrete time representation of the non-equilibrium Green's functions and all other quantities entering the SyDEs, the objects to be handled are in general time-dependent matrices which allows for a numerically straightforward implementation. The system of Dyson Eqs. (2.36)-(2.40) are Volterra integral equations of the second kind. After discretization they become a system of algebraic equations which can be solved by means of standard linear algebra operations [98]. The discretized system of Dyson's equations (DiSyDEs) reads:

$$G^M(\tau_n,\tau'_n) = \Big[G_0^M + G_0^M \star \Sigma^M \star G^M\Big](\tau_n,\tau'_n), \tag{4.2}$$

$$G^{R/A}(t_n,t'_n) = \Big[G_0^{R/A} + G_0^{R/A} \cdot \Sigma^{R/A} \cdot G^{R/A}\Big](t_n,t'_n), \tag{4.3}$$

$$G^{\ulcorner}(\tau_n,t'_n) = \Big[G_0^{\ulcorner} + G_0^{\ulcorner} \cdot \Sigma^A \cdot G^A + G_0^M \star \Sigma^{\ulcorner} \cdot G^A + G_0^M \cdot \Sigma^M \star G^{\ulcorner}\Big](\tau_n,t'_n), \tag{4.4}$$

$$G^{\urcorner}(t_n,\tau_n) = \Big[G_0^{\urcorner} + G_0^R \cdot \Sigma^R \cdot G^{\urcorner} + G_0^R \cdot \Sigma^{\urcorner} \star G^M + G_0^{\urcorner} \star \Sigma^M \star G^M\Big](t_n,\tau_n), \tag{4.5}$$

$$\begin{aligned} G^{\lessgtr}(t_n,t'_n) = \Big[&G_0^{\lessgtr} + G_0^R \cdot \Sigma^{\lessgtr} \cdot G^A + G_0^{\lessgtr} \cdot \Sigma^A \cdot G^A + G_0^R \cdot \Sigma^R \cdot G^{\lessgtr} \\ &+ G_0^{\urcorner} \star \Sigma^M \star G^{\ulcorner} + G_0^R \cdot \Sigma^{\urcorner} \star G^{\ulcorner} + G_0^{\urcorner} \star \Sigma^{\ulcorner} \cdot G^A\Big](t_n,t'_n) \end{aligned} \tag{4.6}$$

where the $\cdot$ and $\star$ symbols are the numerical representation of the time integral convolution:

$$[A \cdot B](t_n, t'_m) = \sum_{p=0}^{N_t-1} w_p \, A(t_n, t_p) B(t_p, t'_m), \tag{4.7}$$

$$[A \star B](\tau_n, \tau'_m) = -i \sum_{\rho=0}^{N_\tau-1} \omega_\rho \, A(\tau_n, \tau_\rho) B(\tau_\rho, \tau'_m). \tag{4.8}$$

The weights w_p and ω_p depend on both the type of grid chosen and the numerical scheme used for the integration. For instance for the standard Riemann integration, we have $w_p = t_f/N_t$ and $\omega_\rho = \beta/N_\tau$. Other choices are of course possible and allow us to exploit different numerical integration methods to reduce the error of the simulations, analogously to what it is done in the case of integro-differential equations (KBE) by choosing higher order integration schemes [98]. Furthermore, the accuracy of the numerical model can always be improved by carefully choosing the number of points in the contour time-intervals N_t and N_τ and their constant time steps dt, $d\tau$, according to the problem at hand. For instance, for a continuously driven system it might be the case that there is no stationarity on the time scale of interest and therefore, the choice of the time step is based on a good resolution of the time-dependent drive itself. For a periodic drive this means that the time grid spacing has to be dense enough to resolve the oscillations in the drive.
Other important elements that need to be represented on the discretize time-interval for the numerical implementation of the NEGF are the identity operators acting on the horizontal and vertical branches of the contour

$$[\mathrm{Id}_\tau \cdot A](t, t') = A(t, t'), \tag{4.9}$$

$$[\mathrm{Id}_t \star A](\tau, \tau') = A(\tau, \tau'). \tag{4.10}$$

Using the above definitions for the numerical time-convolution operations of Eq. (4.7) and (4.8), it is straightforward to check that the numerical version of the identity operators are

$$\mathrm{Id}_t \to \delta_{ss'}\delta_{nm}/w_n \tag{4.11}$$

$$\mathrm{Id}_\tau \to i\delta_{ss'}\delta_{\rho\eta}/\omega_\rho \tag{4.12}$$

where $\delta_{ss'}$ is the Kronecker delta on the spatial(momentum)/spin indexes and δ_{nm} and $\delta_{\rho\eta}$ are Kronecker delta on the time grids indexes. Now, by applying those discretization scheme to a generic Volterra integral equation with unknown A, kernel B and source term C, we can rewrite this equation in the

following way:

$$C_{ij}(t_n, t_m) = A_{ij}(t_n, t_m) - \Big[C \cdot B \cdot A\Big]_{ij}(t_n, t_m) \tag{4.13}$$

$$= A_{ij}(t_n, t_m) - \sum_{rs} \sum_{p,q=0}^{N_t-1} w_p w_q C_{is}(t_n, t_p) B_{sr}(t_p, t_q) A_{rj}(t_q, t_m) \tag{4.14}$$

$$= \sum_{r} \sum_{q=0}^{N_t-1} \left[\delta_{ir}\delta_{nq} - \sum_{s} \sum_{p=0}^{N_t-1} w_p w_q C_{is}(t_n, t_p) B_{sr}(t_p, t_q) \right] A_{rj}(t_q, t_m) \tag{4.15}$$

combining into a multi-indexes $R = \{r, n\}$ the orbital index r and the discrete time index q, we can recast it into the following matrix equation

$$C_{PQ} = \sum_{R} K_{PR} A_{RQ}, \tag{4.16}$$

with the matrix K defined as

$$K_{ir}(t_n, t_q) = \delta_{ir}\delta_{nq} - \sum_{s} \sum_{p=0}^{N_t-1} w_p w_q C_{is}(t_n, t_p) B_{sr}(t_p, t_q). \tag{4.17}$$

Eq. (4.16) is nothing but a collection of $N_s N_t$ algebraic equations whose solution can be found numerically.

4.2 Self-consistent solution of the Dyson equation

After discretization of the time variables, the original SyDEs is mapped onto an algebraic problem which can be solved by means of standard algebraic operations such as matrix multiplications and inversions. We have seen that self-consistency is required to find a solution which respects macroscopic conservation laws. This implies that the self-energy is a functional of the Green's functions itself, see Sec. 2.2.2. Therefore, the solution of the DiSyDEs has to be found self-consistently due to the presence of the kernel self-energy as functional of the SPGF. This means that we have to perform an iteration cycle starting form an initial seed for the Green's function $G(t, t') = G_0(t, t')$, that is needed to calculate the initial components of the many-body self-energy $\Sigma_{MB}[G_0](t, t')$. With this self-energy the DiSyDEs is solved for the components of the interacting Green's function $G(t, t')$. Then new components of the self-energy are computed, and the process is repeated until convergence. Since the Matsubara and the retarded/advanced components of the Green's function are decoupled from all other equations, the solution of the DiSyDEs

is then performed into two main steps: 1) solve self-consistently the Matsubara and the retarded/advanced Dyson equations, 2) solve self-consistently the Dyson equation for all other components.
The self-consistent solution to the Mastubara Dyson Equation at $l+1$ iteration can be written as:

$$G^{M(l+1)}(\tau_n, \tau'_n) = \left[R^{M(l)} \star G_0^M\right](\tau_n, \tau'_n), \tag{4.18}$$

$$R^{M(l)}(\tau_n, \tau'_n) = \left[\left(\mathrm{Id}_\tau - G_0^M \star \Sigma^{M(l)}\right)^{-1}\right](\tau_n, \tau'_n), \tag{4.19}$$

with the resolvent matrix $R^{M(l)}(\tau_n, \tau'_n)$ defined as the inverse of the identity minus the kernel matrix, such that the following relation is satisfied:

$$R^{M(l)} \star \left(\mathrm{Id}_\tau - G_0^M \star \Sigma^{M(l)}\right) = \mathrm{Id}_\tau.$$

Thus, the solution of the Matsubara Green's function requires a matrix inversion at the iteration step l to find the resolvent $R^{M(l)}$. Because the latter depends on the Matsubara self-energy that needs to be updated during the iterative cycle, the inversion has to be done at each iteration step. Analogously to what is done for the Matsubara component, we can find the self-consistent solution of the retarded/advanced equation from:

$$G^{R/A(l+1)}(t_n, t'_n) = \left[R^{R/A(l)} \cdot G_0^{R/A}\right](t_n, t'_n), \tag{4.20}$$

$$R^{R/A(l)}(t_n, t'_n) = \left[\left(\mathrm{Id}_t - G_0^{R/A} \cdot \Sigma^{R/A(l)}\right)^{-1}\right](t_n, t'_n), \tag{4.21}$$

where we have defined the retarded/advanced resolvent to satisfy

$$R^{R/A(l)} \cdot \left(\mathrm{Id}_t - G_0^{R/A} \cdot \Sigma^{R/A(l)}\right) = \mathrm{Id}_t. \tag{4.22}$$

Once the Matsubara and the retarded/advanced components of the interacting SPGF and self-energy are found, they can be used as input in the other equations to calculate self-consistently the remaining components. Although this procedure may appear very simple, few words are in order to clarify some subtle points that one could encounter. Indeed, for the left/right and lesser/greater components at the iteration step $l+1$, one might be tempted to think that all the quantities on which they depend in the r.h.s. of the equations are taken to the current iteration step l. This is found to be an erroneous and inaccurate choice and can lead to the violation of the symmetries properties for the lesser/greater and left/right components of the Green's functions Eq.s (2.35) and (2.33) .
To show this statement explicitly, for simplicity we consider the case in which the dynamical influence of the initial state can be neglected. This translates

in dropping all the functions with at least one time on the vertical time axis and focusing only on the dependence that the lesser/greater components have on the retarded/advanced one. To further lighten the notation we temporarily omit the time-dependence of all the quantities involved in the calculation. Accordingly, the equation to find the lesser/greater Green's function at the iteration step $l+1$ reads:

$$G^{\lessgtr(l+1)} = G_0^{\lessgtr} + G_0^R \cdot \Sigma^{\lessgtr(l)} \cdot G^{A(p)} + G_0^{\lessgtr} \cdot \Sigma^{A(l)} \cdot G^{A(p)} + G_0^R \cdot \Sigma^{R(l)} \cdot G^{\lessgtr(l+1)}. \tag{4.23}$$

At this stage, because in principle we have granted both information, we assume that the iteration index p for the advanced SPGF can be either the current $p = l$ or the next $p = l+1$ iteration step. We will come back shortly to this point. For now, we rewrite the self-consistent solution of the above equations moving all the terms containing $G^{\lessgtr(l+1)}$ to the l.h.s.

$$\begin{aligned} &\left(\mathrm{Id}_t - G_0^{R/A} \cdot \Sigma^{R/A(l)}\right) \cdot G^{\lessgtr(l+1)} = \\ &= G_0^{\lessgtr} \cdot \left(\mathrm{Id}_t + \Sigma^{A(l)} \cdot G^{A(p)}\right) + G_0^R \cdot \Sigma^{\lessgtr(l)} \cdot G^{A(p)}. \end{aligned} \tag{4.24}$$

Then using the identity for the retarded resolvent Eq. (4.22), we get:

$$G^{\lessgtr(l+1)} = R^{R(l)} \cdot \left[G_0^{\lessgtr} \cdot \left(\mathrm{Id}_t + \Sigma^{A(l)} \cdot G^{A(p)}\right) + G_0^R \cdot \Sigma^{\lessgtr(l)} \cdot G^{A(p)}\right]. \tag{4.25}$$

Now, if we fix the iteration index $p = l$, we are left with the following expression

$$G^{\lessgtr(l+1)} = R^{R(l)} \cdot G_0^{\lessgtr} \cdot \left(\mathrm{Id}_t + \Sigma^{A(l)} \cdot G^{A(l)}\right) + G^{R(l+1)} \cdot \Sigma^{\lessgtr(l)} \cdot G^{A(l)}, \tag{4.26}$$

where we have used the solution of the retarded component Eq. (4.20). From the previous expression it is clear that one would need to use simultaneously the new spectrum of the system to evolve forward (encoded in $G^{R(l+1)}$) and the old spectrum to evolve backward in time (encoded in $G^{A(l)}$). This of course would lead to wrong predictions, especially during the first iteration steps where the spectrum of the interacting system is expected to experience notable changes. Moreover and most importantly, this solution results in a violation of the symmetries of the lesser and greater Green's functions due to the asymmetry in the forward and backward propagation.
In order to be consistent *at each* iteration step we have to use in Eq. (4.25) $p = l+1$, in doing so, we can easily recognize in the expression

$$\left(\mathrm{Id}_t + \Sigma^{A(l)} \cdot G^{A(l+1)}\right) = R^{A(l)}$$

the formal solution of the advanced resolvent [1] which allows us to recast the solution for the lesser/greater Green's functions into a simple and elegant form:

$$G^{\lessgtr(l+1)}(t_n, t'_n) = \Big[R^{R(l)} \cdot G_0^{\lessgtr} \cdot R^{A(l)} + G^{R(l+1)} \cdot \Sigma^{\lessgtr(l)} \cdot G^{A(l+1)}\Big](t_n, t'_n). \tag{4.27}$$

Hence, in the particular case where the initial state does not influence the dynamics, the solution of the Dyson equation for the lesser and greater Green's functions requires only the knowledge of the retarded resolvent $R^{R(l)}$ at the current iteration step. As we already mentioned, the computational effort for this task is converted in finding the inverse of a matrix at each iteration step. There is no need to worry about the advanced component since the latter one can be easily computed using the symmetry relations linking it to the retarded one, see Eq (2.34). Nonetheless, when the Matsubara component is present, the same line of reasoning applies, namely one can calculate self-consistently all the other components by using the solutions and the resolvent of the Matsubara and retarded equations. The main difference compared to the case we have analyzed above is that one has to perform an extra inversion to find the Matsubara solution. The self-consistent scheme described above is repeated until convergence is reached. The convergence of a generic matrix at hand A can be established for example by taking the norm over all orbitals and all grid points between two successive iteration, i.e.

$$\Delta A = \left\| A^{(l+1)} - A^{(l)} \right\| := \sum_{rs} \sum_{n,m=0}^{N_t-1} \left| A_{rs}^{(l+1)}(t_n, t_m) - A_{rs}^{(l)}(t_n, t_m) \right|. \tag{4.28}$$

In particular, we use the definition of the norm, Eq. (4.28), to check that the MB current in Eq. (3.6) becomes smaller than a given threshold between two successive iteration and consequently truncate the iterative procedure.
One last point to address for the implementation of the self-consistency, is which Green's functions are used to calculated the new self-energy. In general, one could use simply the Green's functions calculated at the previous iteration or rely on a mixing scheme that mixes the Green's functions at the current and earlier iterations with ad hoc chosen weights [99–101]. Due to the considerable amount of memory required for the mixing procedure, we avoid to use it for the full two-time simulations. We only use this implementation in the numerical scheme that finds the solution at the non-equilibrium steady-state. The self-consistent iteration scheme for the solution of the DiSyDEs is summarized in the flowchart of Fig. 4.1.

[1] To verify the correctness of this expression, it is enough to use it in the advanced solution Eq. (4.20) to recast the advanced Dyson equation.

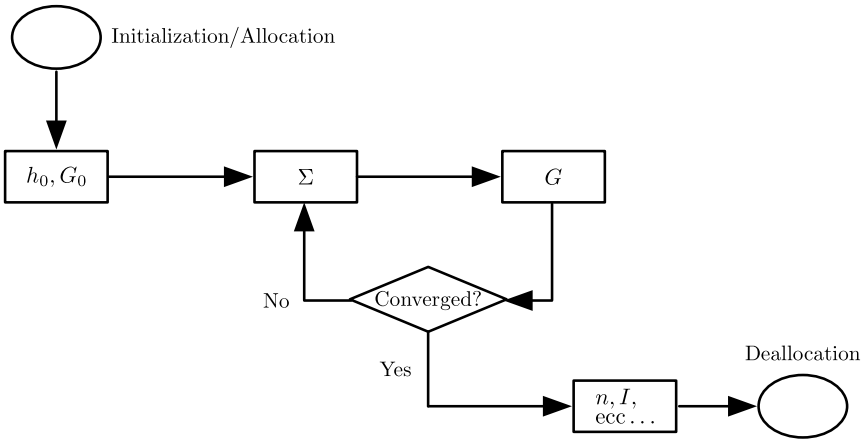

Figure 4.1: Self-consistent iteration algorithm for the solution of the discretized system of Dyson's equations. After the allocation of the $N_s N_t \times N_s N_t$ matrix we compute the single-particle Hamiltonian to construct the non-interacting Green's function. This is used as a seed for the calculation of the MB self-energy that enters the self-consistent cycle. Once the convergence test is passed, we can proceed with the calculation of the physical quantities.

4.3 Parallelization

We have seen that, in order to solve numerically the discretized system of Dyson equations (DiSyDEs), see Eq.s 4.2-4.6, we have to store several matrices whose total size is given by $N_s N_t \times N_s N_t$, with N_s the number of spatial and spin (or momentum and spin) points and $N_t(N_\tau)$ the samples in which the real (imaginary) time-interval is divided into. Typical values of these parameters depend heavily on the type of system that one wants to study. To give an example, we can consider a small chain composed of four sites $N_s = 4$ and characterized by high frequency correlation effects that require a very fine time-grid with $N_t = 10^4$ points to be described. Since each matrix has as entries double-precision complex numbers (a pair of double-precision real numbers), one would need a memory of $25.6\,GB$ to store a single matrix required to study this system. In order to handle such dense and memory consuming matrices, it is wise to resort on parallel computing so that one could distribute *chunks* of matrices across several processes that are able to perform simultaneous calculations on them. The structure of the DiSyDEs as a linear algebra problem also suggests to exploit already existing, well tested and widely used numerical libraries for matrix operations. It is known that a matrix-matrix multiplication performed with a sequential naive algorithm would require a

scaling of the order $\mathcal{O}(N^3)$ with N the total dimension of the matrix. Parallel computation allows one to exploit more refined schemes which help in lowering the scaling with the matrix size to $\mathcal{O}(N^\alpha)$ with $2 < \alpha < 3$.
A fundamental aspect in dealing with any parallel algorithms is to minimize communication between the different processes to avoid transmission bottlenecks which would spoil any advantages that arise from the simultaneous calculations. To minimize and avoid disadvantageous communications, one possible turn around is to cleverly choose the size of the chunks of the matrix to be distributed across the several processes. Indeed, we have paid particular attention to the computation of the self-energies, since this is notoriously the typical *hot spot* limiting the algorithmic efficiency in any numerical implementations for the solution of the KBEs, GKBA and Dyson's equation. It is pivotal to realize that all the self-energies discussed in Sec. 2.2.2 are numerically calculated from algebraic operations among matrices with *fixed* time arguments. Therefore, for a given pair of times (t, t'), (t, τ), (τ, t'), (τ, τ'), the operations needed for their calculations are sums over spatial (momentum) and spin indexes. It is also important to notice that this still applies in the case of the *GW* self-energy, where the extra computational effort comes from the additional matrix-inversion for the dressed interaction rather then the non-local time structure itself. A similar example is the one of the T-matrix approximation for the self-energy, where again an extra inversion is required in order to solve the Bethe-Salpeter equations for the two-particle scattering amplitude [102]. Thus, it is reasonable to divide the global matrix of dimension $N_s N_t \times N_s N_t$ into chunks or blocks which correspond exactly to the full spatial (or momentum) dimension $N_s \times N_s$ and to distribute them across the different processes. This refers to a situation where, for a given pair of time coordinates, each process possesses all the pieces to update the matrix elements of a corresponding global matrix (self-energy, Green's function, ecc...) without the need to communicate with any other processes during the calculation. In other words, the computation and the assignment of the different chunks of the self-energies can be performed locally by each process lowering the communication requirements and speeding-up the calculation.
To deal with parallel computing, we have used the standard Message Passage Interface protocol (MPI) to handle the distribution and creation of a processes-grid together with the Scalable Linear Algebra Package (ScaLAPACK) to perform matrix operations and the Basic Linear Algebra Communication Subprograms (BLACS) to treat communications between processes. The choice to use such standard protocol schemes and well-established routines comes from the fact that the ScaLAPACK libraries together with the BLACS offer a user-friendly interface to exploit efficiently the MPI capabilities, together with the possibilities to take advantages of well-tested and optimized routines to perform algebraic operations and communication tasks. Indeed, for standard

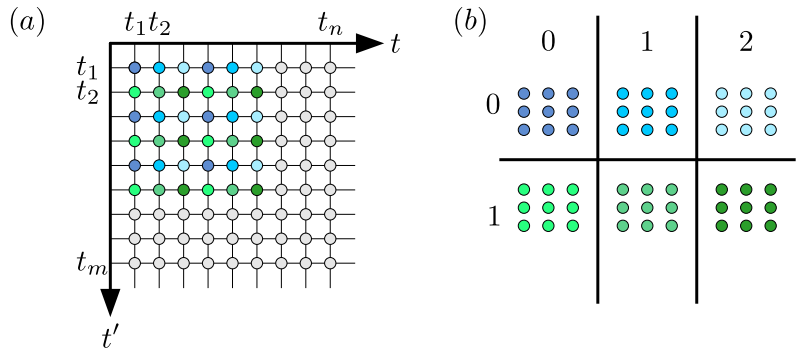

Figure 4.2: (a) View of a $N_s N_t \times N_s N_t$ global matrix in the two-time plane with spatial blocks of dimension $N_s \times N_s$ (dots). (b) Distribution of the spatial blocks for the first pairs of times coordinates according to the 2-dimensional block-cyclic distribution scheme (2DBCD) into a $p_r \times p_c = 2 \times 3$ processes grid generated by using a row-major ordering of the processes (RMOP).

matrix operations such as matrix-matrix or matrix-vector multiplication and matrix inversion, we rely on the improved ScaLAPACK subroutines which are designed exactly for this purpose.
The initialization of p processes into a processes-grid of dimension $p_r \times p_c$ is done by using a row-major ordering of the processes (RMOP), while the distribution of the spacial blocks of the global matrices into this grid is done via a 2-dimensional block-cyclic distribution scheme (2DBCD). Fig. 4.2 panel (a) shows the global structure of a matrix in the two-time plane with spatial blocks of dimension $N_s \times N_s$ (dots), panel (b) illustrates how these spatial chunks for the first pairs of times coordinates are distributed according to the 2DBCD protocol into $p_r \times p_c = 2 \times 3$ processes-grid.

4.4 Overview of the `NEGFs` numerical library

In the previous section we have seen how the NEGF formalism is well suited for a numerical implementation which helps us to find the solutions of several non-equilibrium phenomena. Unfortunately, due to the uncommon two-times structure of the integral equations there are no commercial software presently available to perform the tasks needed to find those solutions, and hence, dedicated software has to be self implemented and programmed. We have developed an open source and scalable library that implements tools for several operations on the non-equilibrium Green's functions, the construction of self-energies, and for the solution of the integral equations involving

contour functions [96, 97]. The NEGFs numerical library contains different routines written in the Fortran 90 programming language that allow the users to implement customized programs for the solution of various physical systems. These routines are categorized according to their core functionalities and they are distinguished between: utilities, initialization, solver and data functions. The utilities subroutines are exploited to handle the initialization of the processes-grid and the allocation of the global matrices through standard MPI and BLACS functions. The routines `sl init`, `mpi comm size` and `blacs gridinfo` are used for the implementation of the RMOP and 2DBCD schemes explained in the previous section. For the initialization stage, we have implemented the `tbham`, `diagsy` and `freeg` subroutines that are optimized and designed for the creation of the single-particle Hamiltonian, its diagonalization and the construction of the components of the non-equilibrium Green's functions. At this level, one could also build the embedding self-energy for the inclusion of the effects that come from the presence of external macroscopic baths Sec. 2.2.3. This is done by calling the subroutine `fmcembslfen` which construct this self-energy starting from the characteristic parameters of the external fermionic leads such us temperature and chemical potential. Once the initialization phase is completed, the users can choose the degree of approximation with whom they want to study the physical systems by using the subroutines `hfself`, `sndbrn` and `GW` for the creation of the different MB self-energies, see Sec. 2.2.2. These functions are called inside the iteration loop for the implementation of the self-consistent cycle where they are used together with the main routine `dyson` for the solution of the integral equations Eq.s (4.2)-(4.6). During the cycle the data subroutine `mcurr` is called to calculate the MB current as explained in Sec. 3.3, Eq. (3.6) and also to check rather that the self-consistent loop has reached convergence or not. This in practice means that the iteration will continue until the value of the MB current is smaller than a given threshold number. After the self-consistent cycle has reached the required convergence threshold, one can calculate the relevant physical quantities from ad-hoc data subroutines such as `mcurr`, `ecurr`, `occnum` and `dos`. As the nomenclature suggests, these routines provide algorithms to compute the corresponding dynamical quantities presented in Chapter 3. We have used the NEGFs numerical library and the above program architecture to study all the different physical systems presented in the original research articles collected in this thesis. Though, being the software still under development, it comes with some limitations that is worth to highlight. In particular, since we have focused our study mostly on transport setup configurations and initially uncorrelated systems, we did not have the need to computes the Matsubara, left and right components of the non-equilibrium Green's functions. Thus, all the routines related to these particular tasks are implemented but not tested. Further details of the NEGFs

numerical library will be soon available trough an extended documentation of the routines capabilities and functionalities at the online repository [96, 97].

Chapter 5

Results

In this chapter we present a selection of effects and results of the quantum transport problems that we have studied in the original research articles **I**−**V** included in the thesis. Our aim is to present an overview of the results obtained during the PhD thesis and, at the same time, to help the reader understand some of the interesting physical phenomena that characterize different transport setups and models. First of all, we describe how the spreading of correlations in a close and interacting system is affected by a non-trivial interplay between the many-body interaction and the underlying energy landscape geometry that characterize quasi-crystalline structures.
Secondly, we test the consequences of the expressions for the variation of energy in correlated open quantum systems derived in Sec. 3.4 by considering an interacting single-level quantum system coupled between two electronic reservoirs. Then, using the non-interacting version of the same model, we show how it is possible to predict the outcome of a cutting edge thermometry experiment that allows the measurement of the electronic lead temperature.
Finally, we present transport spectroscopy results obtained within the stationary solution of the Generalized Kadanoff-Baym Ansatz master equation applied to the prototypical transport setup where two leads, considered in the wide band limit approximation, are connected through a central region. The latter is taken to be either a one-dimensional quantum wire or a two-dimensional carbon nanotube, with the fermionic particles that experience a repulsive interaction treated within the second order Born approximation.

5.1 Anomalous transport in quasiperiodic geometries

The discovery and the production of stable samples of quasi-crystalline materials has triggered theoretical investigations to clarify the origin of their

unusual physical properties [103–105]. The increase of their resistivity, for example, was soon understood to be intimately related to the singular continuous (SC) nature of the single-particle energy spectrum (SPES) [106], whose scaling properties determine anomalous transport and diffusion [107–110]. An essential physical model which describes particle hopping in a one-dimensional quasi-periodic lattice and where the nature of the spectrum plays a pivotal role is the Aubry-André model (AAM). It displays a metal-to-insulator transition [111–113], with the spectrum being absolutely continuous (AC) and pure point (PP) in the metal and insulating phases, respectively. At the transition point between these two phases, the model exhibits a purely singular continuous energy spectrum. The model has been recently realized within the experimental platform of ultra-cold atomic gases loaded in bi-chromatic optical lattices [114–116]. This experiment revealed a dynamical slowing down of correlations due to a non-trivial interplay of quasi-periodicity and interparticle interaction. Inspired by these results on cold-gases, we provide an explanation based on the nature of the single-particle energy spectrum of the observed dynamical slowing down in an interacting gas loaded in an incommensurate bi-chromatic potential. How the many-body interactions affect the properties of SC spectra has been studied in the seminal work in Ref. [117]. There the authors, treating the interactions at the mean-field level, conclude that the SC SPES would be completely washed out by the presence of these interactions. We go beyond their considerations by including correlation effects via the second-order Born approximation, see Sec. 2.2.2 and showing that the singular continuous spectra are robust even when many-body interactions are considered.

We consider a gas made of spin-1/2 particles in one dimension, described by the Fermi-Hubbard model:

$$\hat{H} = \sum_{n,\sigma} \epsilon_n \hat{c}^\dagger_{n,\sigma} \hat{c}_{n,\sigma} - \frac{J}{2} \left(\hat{c}^\dagger_{n+1,\sigma} \hat{c}_{n,\sigma} + \text{h.c.} \right) + U \, \hat{n}_{n,\uparrow} \hat{n}_{n,\downarrow}, \tag{5.1}$$

here $\hat{c}^\dagger_{n,\sigma}(\hat{c}_{n,\sigma})$ are fermionic creation (annihilation) operators at site n with spin σ and $\hat{n}_{n,\sigma} = \hat{c}^\dagger_{n,\sigma}\hat{c}_{n,\sigma}$ is the corresponding number operator. J represents the hopping strength (which we set as reference energy), ϵ_n is the onsite energy and U describes the on-site interaction between particles with different spin in the s-wave approximation. The interacting Aubry-André model (AAM) is obtained by setting $\epsilon_n = \lambda \cos(2\pi\tau n)$ with $\tau = \left(\sqrt{5}+1\right)/2$ being the golden mean and λ the amplitude of the quasiperiodic potential. We choose also to work with open boundary conditions to avoid enforcing any artificial periodicity. It is well known that in the non-interacting case $U = 0$ this model witnesses a metal-to-insulator transition at $\lambda = 1$, in particular, in the thermodynamic limit, one finds that for $\lambda < 1$ the eigenstates are completely delocalized,

whereas for $\lambda > 1$ all eigenstates are exponentially localized [111–113]. For the initial state of the system, we consider two particles with opposite spins at each even site of the chain, whereas the odd sites are left entirely empty. This can also be seen as the ground state of the non-interacting Hamiltonian with a shallower amplitude for the on-site potential at even sites. At time t=0 we assume that a sudden quench of the interaction and of the on-site potential is performed and the Hamiltonian $\hat{H}$ can be used to describe the dynamics of the system. In the case of a quantum walk in aperiodic lattices [110], it has already been shown that the dynamical behavior of the system is essentially independent of the choice of the initial state, provided that the latter is spread among most of the delocalized eigenstates. This ensure that the system would explore most of the single particle spectrum during the time evolution. To study the dynamical properties of this system we apply the numerical scheme discussed in the previous sections and specifically we focus on the information encoded in the lesser components of the single particle Green's function. The correlation effects that arise from the interaction between particles with opposite spin is treated at the second Born level, see Sec. 2.2.2.

5.1.1 Anomalous diffusion induced by the energy landscape potential

The spreading of correlations in non-interacting systems characterized by an *absolutely continuous* (AC) single-particle energy spectrum are ballistic in nature, with a maximum velocity which is limited by the Lieb-Robinson bound [118] and dependent on the initial state and the energy spectrum itself. For systems that possess a *pure point* (PP) single-particle energy spectrum instead, the spreading is fully suppressed by localization effects that make the correlations to take place only in a finite region, the size of this region is proportional to the localization length and vanishes in the thermodynamic limit. As it was suggested in Ref. [102], we use the variance $\sigma(t)$ of the probability

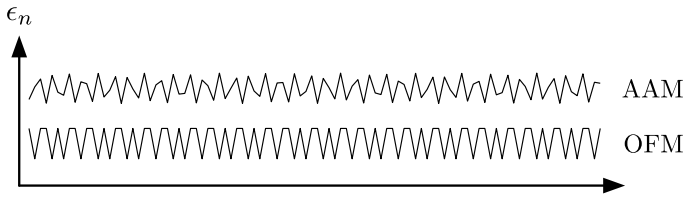

Figure 5.1: Quasiperiodic on site energy landscape potential for the Aubry-André (AAM) and the Fibonacci model (OFM).

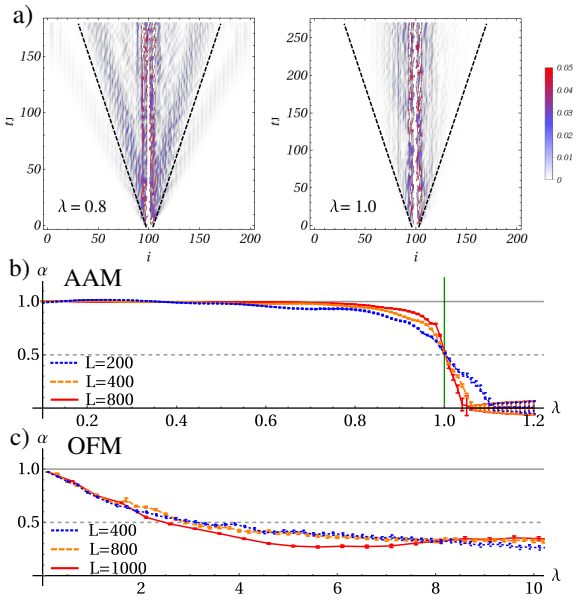

Figure 5.2: (Color online). **a)** Spreading of the single-particle correlations in the Aubry-André model quantified by the time-dependent probability distribution $P_i(t) = |G^{<}_{i_0 i}(0;t)|^2$, with $i_0 = 100$ and for two values of the on-site potential λ. Panels **b)** and **c)** show the exponent of the power law $\sigma(t) \propto t^{\alpha}$ as a function of the on-site potential strength λ and for different system sizes N for the Aubry-André (AAM) and on-site Fibonacci (OFM) model respectively. The vertical green line at $\lambda = 1$ in panel **b)** shows the metal-to-insulator transition point of the AAM, in the thermodynamic limit. Solid and dashed horizontal lines highlight the values of the exponent $\alpha_B = 1$, $\alpha_D = 0.5$ expected for ballistic and diffusive spreading.

distribution:

$$P_i(t) = |G^{<}_{i_0,i}(0;t)|^2 \tag{5.2}$$

to quantify the spreading of the correlations in a non-interacting system with an underlying quasiperiodic potential. Since we treat the non-interacting case $U = 0$, the spin degree of freedom can be disregard and we are free to consider spinless fermions for this analysis. Fig. 5.2 panel **a)** shows the time-dependent probability distribution, Eq. (5.2), of the AAM into two different phases of the system that are characterized by two values of the amplitude potential λ, in particular we have the delocalized phase at $\lambda = 0.8$ and the critical phase at the transition point $\lambda = 1$.
The anomalous propagation of correlations can be quantified by looking at the

exponent of the power-law that the variance of the probability distribution follows at long times, in other words by assuming a power-law behavior at long time $Jt \gg 1$ for the variance $\sigma(t) \propto t^{\alpha}$ of the time-dependent probability $P_i(t)$, we can infer the nature of the dynamics of correlations by studying the exponent α of the power-law decay for different system sizes and different values of the amplitude potential λ. As we can see from Fig. 5.2 panel **b)**, the expansion of correlations is ballistic ($\alpha = 1$) for $\lambda < 1$, whereas it is heavily suppressed for $\lambda > 1$ in the thermodynamic limit. The residual expansion for $\lambda > 1$ comes from the tails (present because of the finite size of the system) of the exponentially localized eigenstates. At $\lambda = 1$ the exponent drops to $\alpha \approx 1/2$, thus indicating a clear deviation from both the ballistic and the localized behavior. To better understand the dynamical-correlations features of the AAM, we compare them with those of the on-site Fibonacci model (OFM), that is obtained by setting $\epsilon_n = \lambda(\lfloor (n+1)/\tau \rfloor - \lfloor n/\tau \rfloor)$ in Eq. (5.1). The OFM does not show any phase transition and it is known to exhibit a purely *singular continuous* (SC) energy spectrum [119] that is induced by its underlying quasiperiodic geometry [120, 121]. The exponent of the power-law for the variance of the probability Eq. (5.2) in the OFM is shown in Fig. 5.2 panel **c)**, where one can recognize a deviation from the ballistic spreading of correlations for any values of the amplitude potential λ. The almost diffusive propagation in the OFM is a characteristic behavior that is shared by other aperiodic structures [122, 123] and it is related to the critical nature of the eigenfunctions together with the SC nature of the spectrum [108, 110, 119]. The above analysis suggests that the AAM at the transition point ($\lambda = 1$) shares with the OFM the SC nature of the single-particle energy spectrum, which is responsible of the deviation from either the simple ballistic propagation or the full localization of the dynamics of correlations.

5.1.2 Interplay between geometry and interaction

In non-interacting systems, we have seen how the presence of an underlying quasiperiodic potential induces anomalous diffusion. Thus, it is reasonable to wonder how these dynamical features caused by a non-trivial geometry may be altered by the inclusion of a many-body interaction. To examine this matter, we apply the machinery of the non-equilibrium Green's functions and treat the interaction at the second order in the perturbation theory to look at the dynamics of a many-body interacting system described by the Hamiltonian in Eq. (5.1) for both the AAM and the OFM. It is well understood that the presence of density-density type interactions can alter in a remarkable way the transport properties of a system. Indeed, in weakly interacting systems in the ergodic phase, where the single-particle eigenfunctions are de-

localized, the spreading of correlations can drastically change from ballistic to diffusive [19, 102]; moreover, for systems that are in the non-ergodic localized phase, the interactions may help the system to acquire a finite diffusivity, by wiping out the confinement properties.
For this particular study, we look at the particle *imbalance* that is an experimentally accessible physical quantity and it is useful to characterized the diffusion properties of a system [19, 115, 116]. The imbalance is defined as

$$\Delta N(t) = (N_e(t) - N_o(t))/N_{tot}, \tag{5.3}$$

with $N_{e/o}(t)$ the time-dependent number of particles at the even/odd sites and N_{tot} the total number of particles in the system. In the delocalized ergodic phase, because all the particles will redistribute evenly among the different sites, the particle imbalance decays to zero $\Delta N(t) \to 0$ on a single-particle time scale ($\sim J^{-1}$). In the localized non-ergodic phase instead, this quantity reaches an asymptotic value $\Delta N(t) \to \bar{N}(\lambda, U) \neq 0$ at long times ($Jt \gg 1$). The authors of Refs. [115, 116] have shown with experiments in cold gases that this is still true in presence of interaction. Close to the critical point $\lambda = 1$, the particle imbalance decays to zero with a power-law behavior. This trend is a clear indication of a non-trivial interplay between the effect of interaction and geometry that we have further investigated in our work. In the numerical simulations that we performed for the AAM, we confirmed the dynamical features of the imbalance that we just described, namely as we increase the amplitude potential λ the time-dependent behavior of the imbalance experiences a slowing-down from an exponential to a power-law decay. In order to quantitatively assess these characteristics, we fitted the imbalance with a power-law of the form $\Delta N(t) = at^{-\beta}$. Notice that all the fits have been performed by excluding the first few tunneling times $Jt \geq 5$ as suggested in Ref. [116]. The reason for that is to avoid the initial, transient dynamics that is characterized by single-particle tunneling. The power-law exponent β is shown in Fig. 5.3 for different values of the amplitude potential λ and the interaction U. We can see that for $\lambda < 1$, $\Delta N(t) \to 0$ in a sub-ballistic/super-diffusive way with $1/2 < \beta \lesssim 1$. Moreover, as U increases the exponent β decreases, as expected for 1D systems at small interactions in the ergodic phase [19]. For $\lambda > 1$, we can distinguish two main behaviors depending on the value of the interaction. As a matter of fact, one can identify a threshold value $U_c(\lambda)$ such that: for $U < U_c(\lambda)$, the particle imbalance tends to an asymptotic value $\Delta N(t) \to \bar{N} \neq 0$ and the exponent goes to zero $\beta \approx 0$, thus pointing to a characteristic long-time localization; for interactions greater than the threshold value $U \geq U_c(\lambda)$, one finds that the imbalance decays to zero $\Delta N(t) \to 0$ as a power-law, with an exponent that is smaller than the one in the delocalized phase and with values included in the range $0 < \beta \lesssim 1/2$, which is essentially

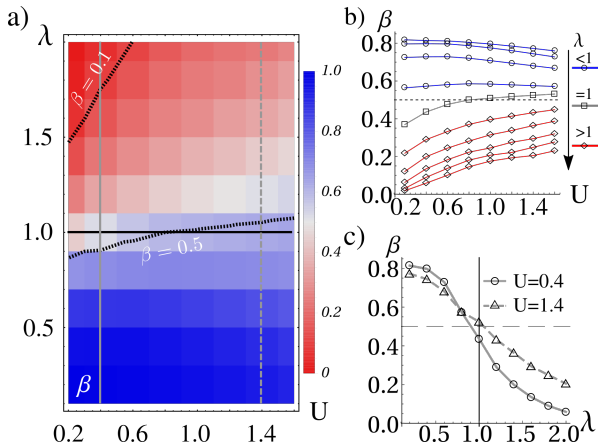

Figure 5.3: (Color online): a) Power-law exponent of imbalance decay $\Delta N(t) \propto t^{-\beta}$ in the AAM as a function of the potential strength λ and interaction U. The black dashed curves identify the region at $\beta = const$, whereas the vertical grey lines show the points of U used in panel c). b) Exponent β as a function of U for different values of λ. The horizontal grey dashed line corresponds to $\beta = 0.5$. c) Exponent β for $U = 0.4$ (solid) and $U = 1.4$ (dashed) as a function of λ.

attributed to a sub-diffusive dynamics. In this last configuration, the dynamics shows a peculiar anomalous dilation compared to the non-interacting case, that is nonetheless very different from pure localization. Furthermore, one can also appreciate that the results obtained with the numerical simulation are in quantitative agreement with the ones extracted from the experiment with ultra-cold atomic gases in Ref. [116], see Fig. 5.3 c).

In the last part of this section, we want to highlight how crucial is the fact that one has access to those dynamical quantities when dealing with small system sizes. Indeed, the characteristic equilibrium spectral properties might not be so evident unless very large system sizes are considered. To give an example, in Fig. 5.4 we plot the spectral function in frequency and momentum space $A(k,\omega) = -\pi^{-1}\mathrm{Im}\, G^R(k,\omega)$ with

$$G^R(k,\omega) = \lim_{T\to\infty} \sum_{nm\sigma} \frac{e^{-ik(n-m)}}{2\pi} \int_{-\infty}^{\infty} d\tau\, G^R_{n\sigma m\sigma}(T+\tau/2; T-\tau/2), \qquad (5.4)$$

for the Aubry-André model in different points of the phase diagram of Fig. 5.3. In the delocalized phase, corresponding to panel a) and b) one can clearly see the different sub-bands induced by the modulation of the energy landscape. Two main gaps are visible, as well as one sub-gap in the top most sub-band

and another in the bottom one. The effects related to the presence of the interaction are quantified by the broadening of the peaks along the ω direction, as well from the closure of the smaller sub-gaps. The latter observation explains how the interaction is able to make the spectrum piece-wise continuous with the closure of the smallest gaps. For higher values of the amplitude potential λ, Fig. 5.4 panels c) and d), the spectral functions shows a broadening along the momentum direction which corresponds to more localized and confined states in real space. Nonetheless, the parameters of the system in panel d) are such that the spreading is anomalous and the presence of localization is substantially reduced.

As in the case of non-interacting systems, the dynamical regimes that distinguish the phase diagram in Fig. 5.3 are emerging features that one can relate to the nature of the single-particle energy spectrum (SPES). In particular, by using arguments from the statistical analysis of time dependent signals [110, 124–127], we were able to identify the presence of an absolutely-continuous SPES in the ergodic phase for small values of the amplitude of the quasi-periodic potential, and a pure-point spectrum in the localized non-ergodic phase at large λ. Moreover, we have discovered that in between these two extreme behaviors lies a critical dynamical region that features a singular continuos SPES, where the dynamics is still ergodic, but on time scales much longer than the typical single-particle ones **II**. These results confirm that the dynamical properties of these systems are guided by the non-trivial competition that takes place between the underlying order, induced by the potential

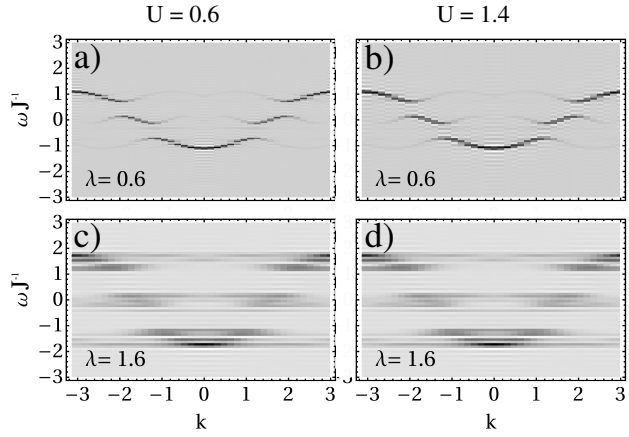

Figure 5.4: (Color online): Spectral function $A(k, \omega)$ of the interacting AAM in the delocalized (panels (a) and (b)) and localized (panels (c) and (d)) phases.

energy landscape, and the many-body interaction.

5.2 Energy variation of a single-level junction in the Kondo regime

Another meaningful example where correlations effects play a crucial role in the transport properties of a system, is given by the single-impurity Anderson model (SIAM) [128–131]. This minimalistic model describes a one-level quantum system coupled between two metallic leads at very low temperature and it can be used to study energy and charge transport in experimentally feasible configurations like quantum dot junctions [14, 15]. In the original Publication **III** included in this thesis, we have used this model to test the consequences of the expressions derived in Sec. 3.4 for the variation of energy in correlated open quantum systems. The Hamiltonian of the single-impurity Anderson model reads:

$$\hat{H} = \varepsilon \sum_{\sigma} \hat{d}_{\sigma}^{\dagger}\hat{d}_{\sigma} + U\hat{d}_{\uparrow}^{\dagger}\hat{d}_{\uparrow}\hat{d}_{\downarrow}^{\dagger}\hat{d}_{\downarrow} + \sum_{\alpha,k\sigma}(\varepsilon_{\alpha k\sigma} + \mu_{\alpha})\hat{c}_{\alpha k\sigma}^{\dagger}\hat{c}_{\alpha k\sigma} - g\sum_{\alpha,k\sigma}(\hat{c}_{\alpha k\sigma}\hat{d}_{\sigma}^{\dagger} + h.c.).$$

Here, $\hat{d}_{\sigma}^{\dagger}\left(\hat{d}_{\sigma}\right)$ are the creation (annihilation) operators of electron on the single impurity level with spin σ, the single-particle energies is denoted by ε and U represents the electronic charging energy. The operator $\hat{c}_{\alpha k\sigma}^{\dagger}$ ($\hat{c}_{\alpha k\sigma}$) creates (annihilates) an electron with state k and spin σ in the lead $\alpha = L, R$ with chemical potential μ_{α}. Finally, g is the tunneling amplitude between the electronic leads and the impurity level. We use the wide-band limit approximation as discussed in Sec. 2.2.3, thus we are left with a frequency-independent coupling $\Gamma = |g|^2$. We consider unbiased leads with their chemical potential fixed to the Fermi energy ($\mu = \mu_L = \mu_R = \varepsilon_F = 0$), and we apply a finite and symmetric thermal bias to the macroscopic reservoirs $T_L = T + \Delta T/2$, $T_R = T - \Delta T/2$, with $T = (T_L + T_R)/2 = 0.125$ the mean temperature of the two leads and $\Delta T = T_L - T_R = 0.15$ their difference. We study the dynamical quantities, in particular charge and energy current, as function of the impurity level position ε. The results are presented as a function of the shifted single-particle energies or gate-voltage $v_g = \varepsilon + U/2$, such that the particle-hole symmetric point $\varepsilon = -U/2$ coincide with $v_g = 0$.
Under particular conditions, which provide high charging energy and tunnel coupling at sufficient low temperature $U \gg \Gamma \gg T$ and $T \ll T_K$, the SIAM might unveil Kondo effects that are characterized by the formation of a correlated asymmetric resonance in the spectral structure of the system [129, 131]. The expression for the threshold temperature, the Kondo temperature, below

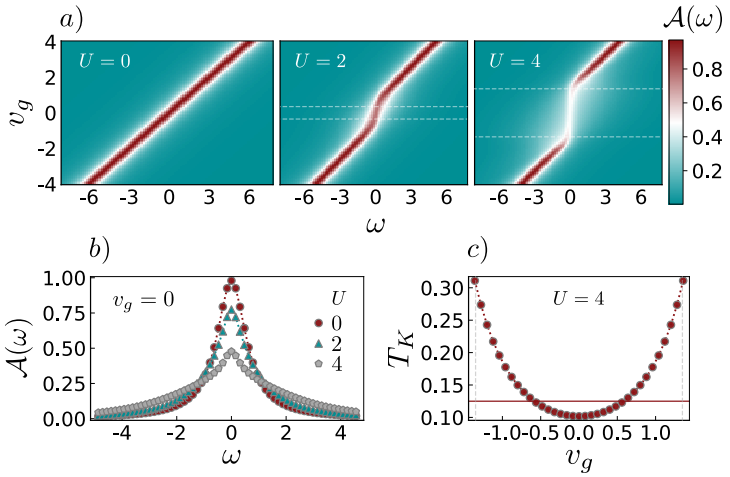

Figure 5.5: Characterization of the Kondo regime. *a*) Density plot in the strong coupling regime $\Gamma = 1.3$ and different interactions strength $U = 0, 2, 4$ of the non-equilibrium spectral function $\mathcal{A}(\omega)$ in the gate-voltage/frequency plane $v_g - \omega$. The white dashed lines represent the range of gate-voltage where the Kondo correlations are expected $-U/2 + \Gamma/2 < v_g < U/2 - \Gamma/2$ for the respective interactions strength. *b*) Corresponding non-equilibrium spectral function at the particle-hole symmetric point $v_g = 0$, $\varepsilon = -U/2$ for the different interactions considered. It is possible to appreciate how the shape of spectral function changes as the Kondo regime is reached $U/\Gamma \gg 1$. *c*) Kondo temperature T_K as a function of v_g in the range of gate-voltage where Kondo correlations occur for the charging energy $U = 4$. The red solid line represents the value of the "average" temperature of the leads $T = (T_L + T_R)/2 = 0.125$.

which these effects take place is given by:

$$T_K = \frac{1}{2}\sqrt{\Gamma U} exp\left(\pi \frac{(v_g^2 - U^2/4)}{\Gamma U}\right) \tag{5.5}$$

and is strictly valid in the Kondo regime where $-U/2 + \Gamma/2 < v_g < U/2 - \Gamma/2$ [130]. The many-body interactions in this system are treated within the self-consistent *GW* approximation (see Sec. 2.2.2 for details), which is known to be able to capture certain features of the Kondo regime [100]. To study the transport of energy in the single-level junction, we have solved the Dyson equation numerically using the method described in Chap. 4.

5.2.1 Kondo correlations

Before the systematic study of the currents, we have first characterized the regime of parameters for which the Kondo correlation effects are present. Fig. 5.5 panel *a*) shows a density plot in the gate-voltage/frequency plane of the steady-state non-equilibrium spectral function of the system $\mathcal{A}(\omega) = i[G^R(\omega) - G^A(\omega)]$ obtained from the numerical solution of the Dyson equation in a strong-coupling regime with the leads $\Gamma = 1.3$ and for different charging energies $U = 0, 2, 4$. As the value of the interaction increases, it is possible to identify a range in the gate-voltage where the spectral function is centered at the chemical-potential of the leads ($\mu = 0$). This interval in gate-voltage corresponds exactly to the range where Kondo correlations are expected $-U/2 + \Gamma/2 < v_g < U/2 - \Gamma/2$ (white dashed lines). Fig. 5.5 panel *b*) shows how the Kondo correlations are responsible for reshaping the spectral function at the charge degeneracy point $v_g = 0$. Moving from zero to large interactions, it is visible how the typical Lorentzian shape for a non-interacting system is gradually lost in favor of a pinned and asymmetric structure.
In Fig. 5.5 panel *c*) we show the Kondo temperature T_K for the charging energy $U = 4$ as a function of v_g in the range of gate-voltage where Kondo correlations take place. As one can notice the average temperature of the leads T (red solid line) lies slightly above the Kondo temperature T_K in a region close to the degeneracy point $v_g = 0$. As we mentioned before, for high average temperatures, it would not be possible to observe the formation of Kondo correlations. Nonetheless, a clear signature of the Kondo regime still remains, namely the spectral function is always pinned at the chemical potential of the macroscopic leads in the whole interval considered and its shape is very different from a Lorentzian function. The explanation for this behavior comes from the highly non-linear out-of-equilibrium scenario ($T \sim \Delta T$) that we have considered; indeed, in this framework, it is very likely that the system does not equilibrate to the average temperature of the leads T and instead reaches a lower temperature that allows the Kondo correlations to persist.

5.2.2 Energy current and virtual processes

After the characterization of the Kondo regime, we have studied the non-equilibrium steady-state properties of the particle and energy currents that flow inside the single level junction. In particular we have compared the variation of charge and energy between the macroscopic leads and the central correlated part of the system. In the case of two symmetrically coupled terminals the particle current of Eq. (3.8) can be rewritten as the Meir-Wingreen formula

$$\lim_{t\to\infty} I_\alpha(t) \equiv I_\alpha = \mathcal{I}_\alpha^{(S)} = \int d\omega \Gamma(\omega)[f_\alpha(\omega) - f_{\bar{\alpha}}(\omega)]\mathcal{A}(\omega). \tag{5.6}$$

Here $\Gamma(\omega) = \Gamma_L(\omega)\Gamma_R(\omega)/[\Gamma_L(\omega) + \Gamma_R(\omega)]$, $\bar{\alpha} \neq \alpha$, $f_\alpha(\omega) = (1 + e^{\beta_\alpha(\omega-\mu_\alpha)})^{-1}$ is the Fermi-Dirac distribution function for the electrons in the macroscopic α-lead and $\mathcal{A}(\omega)$ is the non-equilibrium spectral function of the central region. For the energy current we compare the steady-state expression of the energy variation for the central region that we have derived in Chap. 3, Eq. (3.29), $\lim_{t\to\infty} J_C^{(\alpha)}(t) \equiv \bar{\mathcal{J}}_C^{(\alpha)}$, with the energy counterpart of the Meir-Wingreen formula that properly describes how the energy runs across the non-interacting leads:

$$\lim_{t\to\infty} J_\alpha(t) \equiv J_\alpha = \mathcal{J}_\alpha^{(S)} = \int d\omega\ \omega\Gamma(\omega)[f_\alpha(\omega) - f_{\bar{\alpha}}(\omega)]\mathcal{A}(\omega). \tag{5.7}$$

Fig. 5.6 shows the agreement between the charge current in the central region due to the left electronic lead $I_C^{(L)}(t) \equiv \mathcal{I}_C^{(L)}(t)$ and the opposite of the current that flows into the same lead $-\mathcal{I}_L^{(S)}$, the results refer to both the weak coupling $\Gamma \ll \Delta T$ (panel *a*)) and the strong coupling regime $\Gamma \gg \Delta T$ (panel *b*)) for different values of the interaction strength U. As one would expect, see Sec. 3.3 for details, the two currents are equal and opposite regardless the regimes considered and the values of the parameters chosen.
In contrast to the particle current, a perfect agreement between the energy current across the interacting region due to the left reservoir $\bar{\mathcal{J}}_C^{(L)}$ and the opposite current in the same lead $-\mathcal{J}_L^{(S)}$ is found only in the weak-coupling scenario as shown in Fig. 5.6 panel *c*). In the strong coupling regime, one can notice not only a quantitative deviation between these two expressions, but rather a qualitatively different behavior due to the considerable interaction between system and environment, see Fig. 5.6 panel *d*). The many-body interactions are not responsible for this deviation as the effect is persistent, and actually more pronounced, in the non-interacting case ($U = 0$). When the system is at particle-hole symmetric point ($v_g = 0$), it is at resonance with the leads and therefore is completely transparent, so that all the energy flows from one lead to the other without affecting the energy of the central region. This explains the maximum difference between the two currents at this particular gate voltage where $\bar{\mathcal{J}}_C^{(L)}$ is zero and $\mathcal{J}_L^{(S)}$ has its maximum. The presence of Kondo correlations manifests itself as a plateau in the energy currents in the range of gate-voltage where they are predicted, namely for $-U/2 + \Gamma/2 < v_g < U/2 - \Gamma/2$. These regions are shown in Fig.5.6 as green and gray shaded areas and they corresponds to the regions in which the spectral function is pinned at the chemical potential of the leads, as shown by the horizontal dashed lines in Fig.5.5 panel a). As we noticed above, the pinning of the spectral function is an hallmark of the emergence of the Kondo bound state. Thus it is particularly significant that this feature manifests itself through relevant physical quantities like the energy current and other transport properties, since this can help envisaging experimental platforms

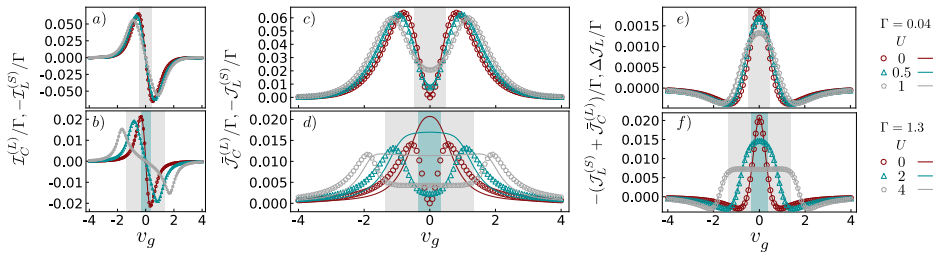

Figure 5.6: Particle and Energy currents. $(a)-(b)$ comparison of the steady-state particle currents flowing through the central region due to the left lead $\lim_{t\to\infty} \mathcal{I}_C^{(L)}(t)$ (markers) and the opposite current that runs into the same lead $-\mathcal{I}_L^{(S)}$ (solid lines) in the weak coupling $\Gamma = 0.04$ (a) and in the strong coupling regimes $\Gamma = 1.3$ (b) at the charging energy U as indicated in the legend. $(c)-(d)$ parallel between the steady-state energy currents across the interacting system from the left lead $\bar{\mathcal{J}}_C^{(L)}$ (markers) and the opposite of the energy current flowing into the corresponding lead $-\bar{\mathcal{J}}_L^{(S)}$ (solid lines) at the same couplings and charging energies as in the case of particle currents. $(e)-(f)$ comparison between (minus) the sum of the two steady state energy currents $-(\bar{\mathcal{J}}_L^{(S)}+\bar{\mathcal{J}}_C^{(L)})$ (markers) and the term $\lim_{t\to\infty} \Delta\mathcal{J}_L(t)$ (solid lines) in the region of parameters as specified before. All the quantities are normalized by their respective Γ. The shade areas in the figures correspond to the gate-potential range of the Kondo regime $-U/2 + \Gamma/2 < v_g < U/2 - \Gamma/2$ for the related couplings and charging energies.

to probe Kondo correlations [15]. Interestingly, in the case of a thermal bias in the leads the plateau induced by the Kondo cloud appears in the energy current, whereas in the case of small bias voltage it appears in the particle current as we have shown in Ref. **I**. In general, one would expect that interactions increase the change of energy in the central region with respect to the non-interacting case. We have found however that this is not always the case and, indeed it strongly depends on the relative energy position of the level junction compared to the chemical potential of the electronic leads. We do not have a physical explanation for this feature yet and we are currently planning a follow up investigation to further understand the physical origin of this effect.

We have seen that the energy variation of one electronic lead and the lead's contribution to the variation of the energy in the central correlated region differ in the strong coupling regime by an amount $\Delta J_\alpha(t)$. We have derived

this term in Sec. 3.4, see Eq. (3.35), and we have seen that it comes from a direct lead to lead coupling via second order processes through the central region. Furthermore, we have seen that this term is not vanishing in the strong coupling regime of the SIAM and also that is weakly influenced by the many-body correlations and still present in the non-interacting system. If we calculate the term $-\mathcal{J}_L^{(S)} - \mathcal{J}_C^{(L)}$ and compare it with $\Delta\mathcal{J}_L$ computed separately, see Eq. (3.37), we obtain a perfect agreement as presented in Fig. 5.6 $e) - f)$ for both the weak and the strong coupling regime respectively. It is worth to notice that, whenever the interaction is present, the energy rate contribution $\mathcal{J}_C^{(L)}(t)$ is never zero when the density of states of the dot is in the energy window of the leads. Thus, the presence of the interaction redistributes the energy within the quantum dot and forbids from a complete transparency as in the non-interacting case.

The lead-lead coupling has been already discussed in [132–134] with the noticeable difference that in these works the lead-lead interaction was already introduced in the Hamiltonian of the system. Moreover, the influence of such coupling on the energy transfer and its microscopic mechanism has not been investigated. As a concluding remark, we would like to emphasize the significance and the implications of the term $\Delta\mathcal{J}_\alpha$ whenever it is not vanishing. When probing electrical or thermal conduction properties of a system, measurements are carried out on the macroscopic leads. In the case of particle currents, the rate of change of particles in the electronic lead equals the change of particles in the central region due to that particular lead. Therefore, the measure of the charge current *into* the lead is equivalent to measuring the change in the particle currents in the central region. Hence, it is meaningful to infer the electrical conductivity of the central region from the measured current in the electronic macroscopic leads. Nonetheless, when it comes to compute the thermal conductivity of the system in the central correlated region

$$\kappa = \frac{\partial \dot{\mathcal{Q}}_L}{\partial \Delta T} \mid_{\mathcal{I}_L^{(S)}=0}, \tag{5.8}$$

with the heat current given by

$$\dot{\mathcal{Q}}_L = (\mathcal{J}_L^{(S)} - \mu_L \mathcal{I}_L^{(S)}), \tag{5.9}$$

one has to bear additional care on what is the real interpretation of what it is calculated. Indeed, according to Eq. (3.37), at the non-equilibrium steady-state and in the absence of external drive, one has

$$\kappa = -\frac{\partial}{\partial \Delta T}\left(\bar{\mathcal{J}}_C^{(L)} - \mu_L \mathcal{I}_C^L + \Delta\mathcal{J}_L\right) \mid_{\mathcal{I}_C^{(L)}=0}, \tag{5.10}$$

where we replace $\mathcal{I}_L^{(S)} \to -\mathcal{I}_C^{(L)} = -\lim_{t\to\infty} \mathcal{I}_C^{(L)}(t)$. The last equation shows that to compute the thermal conductance of the central region, the lead-lead

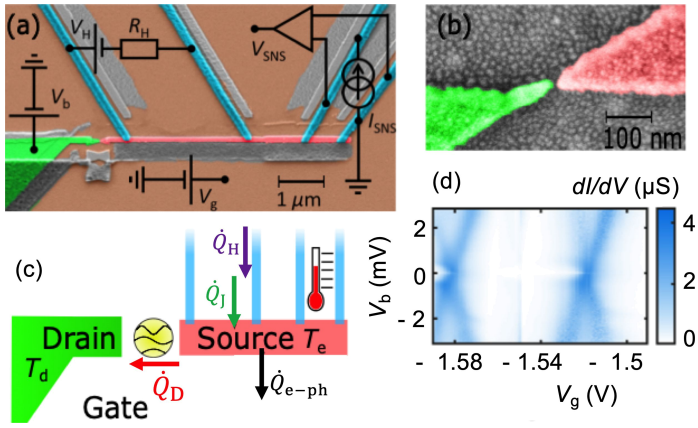

Figure 5.7: (a) False-colored scanning-electron-micrograph (SEM) image of the device. The source is colored in red, the drain in green and the superconducting leads in blue. The circuit diagram shows the heat transport set-up. The longer superconductor-normal metal-superconductor (SNS) junction is used as a heater driven by a constant d.c. battery and the shorter SNS junction is used as a thermometer. (b) Zoomed-in view of the nano-gap between the *source* and *drain* created by electromigration and the nano-particles made by Au evaporation. (c) Schematic of the device, with the different heat flows to/from the source. (d) Differential conductance map of the device measured at 70 mK against the drain-source bias voltage V_b and the gate voltage V_g with no additional heating applied.

term $\Delta\mathcal{J}_L$ has to be included. As we have investigated, this term accounts for the energy transfer through the contacts. Accordingly, in the strong coupling regime or for spatially extended couplings, what one really calculates is the interface thermal conductance between the two leads, as if the two were directly coupled via a renormalized tunneling.
We conclude this section noticing that, in the case of strong coupling and/or when the coupling of the leads are spatially extended, the common description of thermal conductance could be misleading as a figure of merit for the thermal characteristics of the central region. This is in contrast with the electrical conductance which is, instead, always consistent with the particle currents in the central region.

5.3 Quantum dot heat-valve

Due to the miniaturization of electronic components down to the nano-scale, it has become necessary to understand how heat is dissipated and redistributed

down to this scale [135–138]. Handling of heat fluxes and thermometry at nanoscale and in the milli-Kelvin regime is a very interesting and challenging problem for quantum technologies that will ultimately lead to engineering new and more efficient electronic components [132]. At the same time, new scenarios are opening, such as that of a heat-driven circuitry [139, 140]. Feasible gate-tunable single-quantum dot (QD) junctions [141] are paradigmatic test benches for quantum transport and fundamentally important in the emerging field of quantum thermodynamics to understand heat transport and dissipation effects in quantum electronic devices. In publication **IV**, included in the thesis, we demonstrate the possibility of engineering a heat-valve through a single-level quantum dot. In contrast with the common expectation that the heat conduction is zero at a degeneracy point, we observe a significant cooling over a sizable parameter range around this point, therefore making the heat-valve having a broad operational range. This experimental achievement is reached through the combination of ultra-sensitive electronic thermometry based on a hybrid Josephson junction and electro-migration in a single device, see Fig. 5.7. The experimental data are then compared with the theoretical approach based on the non-equilibrium Green's functions presented in the previous chapters that allows to extract the temperatures directly from the stationary electronic distributions of the macroscopic reservoirs, see Sec. 3.5. The agreement between the experimental data and the theory for a particular set of parameters allows us to explore the characteristics of the heat-valve in a wider range of temperatures and coupling of the quantum dot to the electronic leads.

The system used to model the experimental device is similar to the one used in the previous section with the exceptions that now we consider a non-interacting and spin-independent single-impurity Anderson model. The Hamiltonian of the total system (quantum dot plus source and drain reservoirs) is given by:

$$\hat{H} = \hat{H}_{QD} + \sum_{\alpha=S,D} \hat{H}_\alpha + \sum_{\alpha=S,D} \hat{V}_{QD}^{(\alpha)} \tag{5.11}$$

$$\hat{H}_{QD} = v_g \hat{d}^\dagger \hat{d}, \tag{5.12}$$

$$\hat{H}_\alpha = \sum_{k_\alpha} \epsilon_{k_\alpha} \hat{c}_{k_\alpha}^\dagger \hat{c}_{k_\alpha}, \tag{5.13}$$

$$\hat{V}_{QD}^{(\alpha)} = \sum_{k_\alpha} g_\alpha \left(\hat{c}_{k_\alpha}^\dagger \hat{d} + \hat{d}^\dagger \hat{c}_{k_\alpha} \right), \tag{5.14}$$

where $v_g = \alpha(V_g - V_g^0)$ is the gate voltage measured from the considered resonance and accounting for the coupling parameter [1]. $\hat{V}_{QD}^{(\alpha)}$ is the coupling Hamiltonian between the quantum dot QD, and the source and drain leads $\alpha = S, D$. Using the non-equilibrium Green's function approach presented in Chap. 2, and assuming that the whole system reaches a possibly non-equilibrium steady-state, the state of the QD is completely characterized by the retarded and lesser single-particle Green's functions Eq.s (2.74), (2.75) as explained in Sec. 2.4. The embedding self-energy approach, see Sec. 2.2.3, accounts for the effect that the leads have on the physical properties of the system, but once the numerical solution is obtained, it is possible to find the Green's functions of the leads and explore how the QD influences on the physical characteristics of the reservoirs. By introducing the inbedding self-energy (Sec. 2.2.4) and resorting to the hot-electron assumption as described in Sec. 3.5 we were able to predict the outcome of the thermometry experiment on the electronic lead temperature.

5.3.1 Electronic lead temperature

Here we report the main results that we have obtained and we refer to publication **IV** for further details on the experimental realization of the sample and the measurements implementation. In the experiment, the source lead is heated up by applying a constant heating power $\dot{Q}_H = 6fW$ to the heater junction, see Fig. 5.7. The drain is biased at a potential V_b relative to the source that is grounded via one of the superconductor-normal metal-superconductor (SNS) thermometer contacts. Figure 5.8 (a) shows the measured map of the source electronic temperature as a function of V_b and V_g. The source temperature T_e increases rapidly as the charge current raises due to the related Joule power. Right at the charge degeneracy point, the source temperature drops down to its equilibrium value and it is lower than in the rest of the map. Figure 5.8 (c) shows a simple energy diagrams representation that is used to explain the observed behavior for the cases specified by circles in the temperature $T_e(V_g)$ profiles at two different bias of Fig. 5.8 (b). At zero bias and away from the charge degeneracy point (case 1), there is neither heat flow through the QD nor Joule power due to the particle current. The source is overheated up to $T_e = 163.5$ mK due to the balance between the applied power $\dot{Q}_H$ and the main thermal leakage channel, namely the electron-phonon coupling $\dot{Q}_{e-ph}$. Still at zero bias, but near a charge degeneracy point (case 2), there is a heat flow $\dot{Q}_{QD}$ through the QD, but still no charge current. This shows up (blue curve in Fig. 5.8 (b)) as a temperature T_e drop by several

[1] Here α is an experimental parameter called coupling parameter that translates the effect of the gate voltage in terms of shift in chemical potential of the QD.

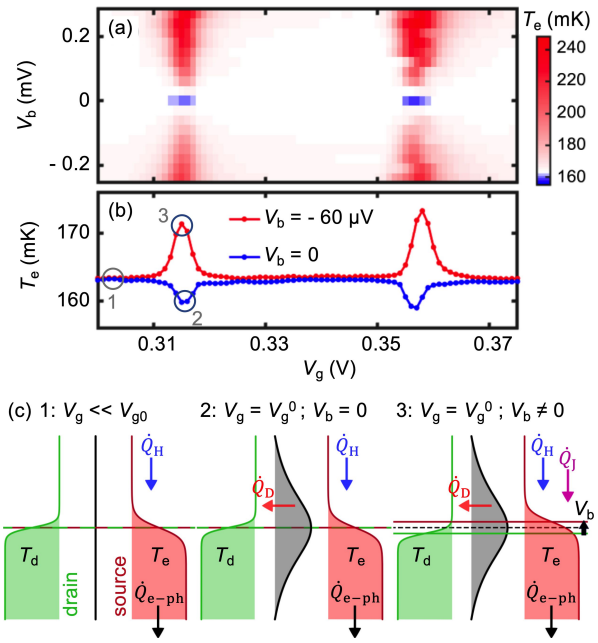

Figure 5.8: (a) Experimental map of the source electronic temperature in the $V_b - V_g$ plane. (b) Individual gate traces of the source temperature at two different bias values. (c) Schematic energy diagram of the heat flowing in/out of the electronic source in various conditions as indicated by labels in (b): (1) away from charge degeneracy and at zero bias (left), (2) at a charge degeneracy point $V_g = V_g^0$ and at zero bias (middle) or (3) at non-zero bias (right). The gray profile depicts the quantum level spectral density. The ratio between the level broadening $\hbar\Gamma$, the bias V_b and the thermal energy k_BT is in correspondence with panel (b) conditions. The arrows indicate the applied heating power $\dot{Q}_H$, the Joule power $\dot{Q}_J$, the electron-phonon coupling power $\dot{Q}_{e-ph}$ and the power flow through the QD $\dot{Q}_D$.

mK at the charge degeneracy point. Thus, the gate-controlled QD junction allows the heat to flow-out from the source lead acting as a heat-valve. At higher bias (case 3), this cooling contribution is overcome by the Joule power $\dot{Q}_J$. A maximum value of the electronic source temperature is thus observed for gate potentials close to the charge degeneracy point (red curve in Fig. 5.8 (b)). As we mentioned before, the device can be described as a non-interacting single energy level, Eq. (5.11), due to the experimental high charging energy in the proximity of a charge degeneracy point. The inbedding-technique is not based on a full heat balance model between the heat flow via phonons and the superconducting leads. Instead, it makes the assumption that the

main particle and energy redistribution processes in the lead are dominated by electron-electron interactions and not by the electron-phonon coupling. By including in the theory the measured temperature (163.5 mK) of the source when it is decoupled from the QD, we effectively take into account its thermal coupling to the phonon-bath. The high resolution theoretical temperature map around a charge degeneracy point is shown in Fig. 5.9 (b) and reveals a nice agreement with the experimental data in Fig. 5.9 (a). Here, the temperature of the drain T_{d} is set to 85 mK and the coupling of the QD to the drain is asymmetric with a coupling ratio $\Gamma_{\mathrm{L}}/\Gamma_{\mathrm{R}} = 3/17$ between left and right leads and $\Gamma = 0.25meV$. These are the best fit values that allow us to

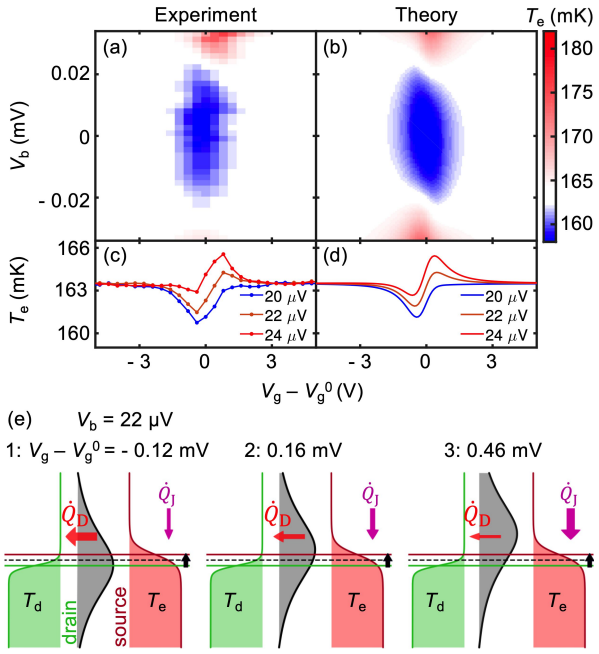

Figure 5.9: (a) A highly-resolved map of the source electronic temperature at the same experimental condition as in Fig. 5.8 and around a charge degeneracy point defined by $V_g = V_g^0$. (b) Calculated temperature map obtained with the inbedding-technique with $\Gamma = 0.25meV$, $\Gamma_L/\Gamma_R = 3/17$ and $T_d = 85mK$. (c) Experimental and (d) theoretical variation of the temperature in the region where crossing from cooling to heating is observed; each curve refers to a given applied bias V_b: (blue) $20\mu V$, (orange) $22\mu V$, (red) $24\mu V$. (e) The schematics describing the crossover between the heat flow $\dot{Q}_D$ and the Joule heat $\dot{Q}_J$ as a function of the gate potential and at fixed bias voltage. At $V_g - V_g^0 =$ - 0.12 mV (case 1, left) temperature decrease, at 0.16 mV (2, middle) the two heat flows balance each other and at 0.46 mV (3, right) temperature increase.

reproduce quantitatively the temperature profiles of the crossing region, see Fig. 5.9(c,d). It is of greatest importance to notice that the observed cooling at the charge degeneracy point is incompatible with the theoretical predictions in a weak coupling, sequential tunneling regime. Indeed, the experiment deals with a strong tunnel coupling between the QD and the leads, with a ratio of about $\hbar\Gamma/k_{\mathrm{B}}T_{\mathrm{e}} \approx 20$, that makes the weak coupling picture inapplicable.
Another important and peculiar feature that we have observed and predicted in this study is the asymmetry in gate voltage that emerges in the experimental and theoretical temperature map. For a bias voltage V_b around 22 μV, the source temperature can be tuned either below or above the reference temperature of 163.5 mK by acting on the gate voltage, see Fig. 5.9 (c). We have found, see **IV**, that this characteristic is an unambiguous signature of the QD discrete energy spectrum. At a given bias, the value of the gate potential determines the position of the broadened energy level in the QD (see the grey profile in Fig. 5.9(e)) and thus the mean energy of the tunneling electrons. This in turn affects the heat balance in the source and modifies the boundary of the cooling region in the temperature map. The extension in bias of this crossover zone, where one can switch from cooling to heating by adjusting with the gate, depends on both the coupling Γ and the temperature difference across the QD. To conclude this section, we want to highlight that this work proposes both a new technological viable route to control heat fluxes and perform less-invasive temperatures measurement, and, from the theoretical point of view, it gives a clear understanding of the manipulation of heat flow in terms of microscopic processes without relying on any phenomenological approaches.

5.4 Transport spectroscopy of correlated quantum wires and carbon nanotubes

We have seen that understanding the properties of correlated systems coupled with macroscopic reservoirs with which they can exchange energy and particles is of fundamental importance for the realization of new quantum technological devices. The field of application is broad, encompassing out-of-equilibrium phases, pump-probe experiments and time-resolved dynamical properties, transport in correlated systems, equilibration and thermalisation in strongly correlated materials. Despite such a wide range of applications, the theoretical description of out-of-equilibrium many-body systems remains a challenging task. The difficulty arises because different and relevant ingredients need to be included in the description. Some of these are many-body interactions, external time-dependent fields and the possibility of exchanging energy and matter with the environment. Among the perturbative methods, we have used the non-equilibrium Green's functions which describe the open

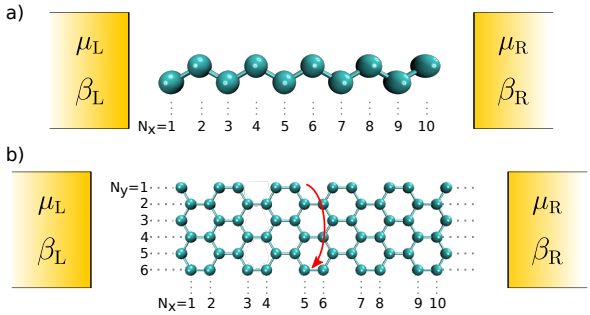

Figure 5.10: (Color online) Schematic of the transport setups considered. **a)** A quantum wire connected with two metallic leads. Only the outer-most sites are connected to the leads. **b)** A carbon nanotube connected to two metallic leads. The left-most carbon atoms are connected to the left lead, and the right-most carbon atoms are connected to the right lead (rows $N_y = \{1, 3, 5\}$). The red arrow signifies periodic boundary condition along the y-direction folding a graphene nanoribbon into a carbon nanotube.

correlated system dynamics trough the Kadanoff-Baym equations or equivalently the Dyson equation (Chap. 2).
In the original research article **V** included in this thesis, we use the Generalized Kadanoff-Baym Ansatz (GKBA), which reduces the complexity of the Kafanoff-Baym equations by lifting the two-time structure, and allows to derive a master equation for the system's density matrix, see Sec. 2.3. There, we study a transport setup where two leads, considered in the wide band limit approximation, are connected through a central region, taken to be either a one-dimensional or a two- dimensional quantum system, see Fig. 5.10. Our key result is that the GKBA is able to capture fundamental features of the spectrum of a correlated many-body system when the stationary particle current is used as a probe for such properties. For this reason, we refer to the latter technique as a transport spectroscopy technique in correlated open quantum systems.
Our work, together with the recent speed-up achieved in the computation of the collision integrals for self-energies beyond the Second-Born one [80, 81], contributes to show that the GKBA is a powerful and reliable method to study out-of-equilibrium phenomena in many-body open and closed quantum systems. In the following, since the conclusions that we have drawn are the same for both the systems considered, we report only the results for the two-dimensional system that models the transport properties of a carbon nanotube (CNT) [142, 143]. The total adimensional Hamiltonian to describe the CNT is the usual Fermi-Hubbard Hamiltonian used to model the previous systems,

with the exception of the Hamiltonian for the central system that now is defined on an honeycomb lattice:

$$\hat{H}_C = \epsilon \sum_{\mathbf{i}\sigma} \hat{n}_{\mathbf{i}\sigma} - \frac{1}{2} \sum_{\langle \mathbf{i},\mathbf{j} \rangle_y \sigma} \hat{c}^\dagger_{\mathbf{i}\sigma} \hat{c}_{\mathbf{j}\sigma} + U \sum_{\mathbf{i}} \hat{c}^\dagger_{\mathbf{i}\uparrow} \hat{c}^\dagger_{\mathbf{i}\downarrow} \hat{c}_{\mathbf{i}\downarrow} \hat{c}_{\mathbf{i}\uparrow}, \tag{5.15}$$

$$\hat{H}_\alpha = \sum_{k\sigma} \epsilon_{\alpha,k} \hat{d}^\dagger_{\alpha,k\sigma} \hat{d}_{\alpha,k\sigma}, \tag{5.16}$$

$$\hat{V}_\alpha = \sum_{\mathbf{i},k\sigma} T^\alpha_{\mathbf{i}k} \hat{c}^\dagger_{\mathbf{i}\sigma} \hat{d}_{\alpha,k\sigma} + T^{\alpha *}_{\mathbf{i}k} \hat{d}^\dagger_{\alpha,k\sigma} \hat{c}_{\mathbf{i}\sigma}, \tag{5.17}$$

where $\hat{c}^\dagger_{\mathbf{i}\sigma}, \hat{c}_{\mathbf{i}\sigma}$ are the creation (annihilation) operators of electrons in the basis labeled by $\mathbf{i}$ and spin $\sigma = \uparrow / \downarrow$, where the indexes $\mathbf{i}$ run over the points of a honeycomb lattice and $\langle \cdots \rangle_y$ stands for the sum over the vertices of the lattice. The operators $\hat{d}^\dagger_{\alpha,k\sigma}, \hat{d}_{\alpha,k\sigma}$ are the creation (annihilation) operators of the two different leads, denoted as $left$ and $right$, and labelled by $\alpha = L, R$. Once again, ϵ is the on-site potential, U is the two-body interaction between spin-up and spin-down particle on the same site and $T^\alpha_{\mathbf{i}k}$ is the tensor containing the coupling rates between the leads α and the chain. We consider periodic boundary conditions along the y direction as shown in Fig. 5.10 and therefore a zigzag nanotube. In addition, we consider the number of armchair dimer lines in the transport direction $N_y = 6$ representing a metallic character.
The two leads are kept in a thermal state at the same temperature, i.e. $\beta_L = \beta_R$, but a with different chemical potential given by $\mu_L = -\mu_R = \mu$. In particular, we have set the initial parameters as follows $T^2_L = T^2_R = 0.5$, $\mu = 0.5$ and $U = 1$. As in the previous analysis, we use the gate potential $V_g = \epsilon + U/2$ to shift the spectrum of the central region with respect to the chemical potential of the leads and we use the developed particle current through the junction to probe the spectral properties of the central region at different energies. Furthermore, we look at the differential conductance $\sigma = dI/dV$ that is able to capture more details of the spectral weights than the current that is an integrated quantity. In the previous expression V is the applied bias voltage across the central region, i.e. $V = 2\mu$. Before moving to the actual analysis of the results, we briefly justify the reasons why those two quantities are well suited for the transport spectroscopy study. The general expression for the particle current that flows into the lead α was derived in Sec. 3.3 and its non-equilibrium steady-state counterpart is written in Eq. 3.8. The latter can be rewritten as:

$$I^{(S)}_\alpha = i \int \frac{d\omega}{2\pi} \, \mathrm{Tr} \left[\Sigma^<_\alpha(\omega) \mathcal{A}(\omega) - \Gamma_\alpha(\omega) G^<(\omega) \right], \tag{5.18}$$

where $\Gamma_\alpha(\omega) = i \left(\Sigma^R_\alpha(\omega) - \Sigma^A_\alpha(\omega) \right)$ and $\mathcal{A}(\omega) = i \left(G^R(\omega) - G^A(\omega) \right)$. Here one can see explicitly the dependence of the current from the spectral function

$\mathcal{A}(\omega)$ (the long-time limit of Eq. (3.3)) and the Fourier transform of the lesser Green's function $G^<(\omega)$. Eq. (5.18) can be further rearranged in the Landauer-Büttiker form [87, 88]:

$$I_\alpha^{(S)} = \int \frac{d\omega}{2\pi} \sum_\beta T_{\alpha\beta}(\omega)(f_\alpha(\omega) - f_\beta(\omega)), \tag{5.19}$$

with $f_\alpha(\omega) = (1 + e^{\beta_\alpha(\omega-\mu_\alpha)})^{-1}$ the Fermi-Dirac distribution of the electronic lead α and $T_{\alpha\beta}(\omega) = \mathrm{Tr}\left[\Gamma_\alpha(\omega)G^R(\omega)\Gamma_\beta(\omega)G^A(\omega)\right]$ the transmission coefficient. Because of its direct dependence on the retarded propagator, this expression might suggest that the GKBA, even within the 2B approximation, is not able to go beyond the spectral features captured at the HF level, see Sec. 2.3 for details. However, it is critical to realize that the derivation of Eq. (5.19) relies heavily on the equality $G^<(\omega) = G^R(\omega)\Sigma^<(\omega)G^A(\omega)$. The latter holds at the non-equilibrium steady-state, see Sec. 2.4, and it is a direct consequence of the Dyson equation with the full retarded self-energy. Thus, it can not hold in the case of the GKBA-HF approximation. Eq. (5.18) is an exact reformulation of the expression that comes from the definition of the particle current and contains explicitly the lesser Green's function. The latter quantity in the GKBA-HF formulation carries information about higher order correlation effect through a different many-body self-energy compared to the one of the retarded propagator. Thus, we ought to rely on Eq. (5.18) to capture features beyond the mean field approximation.

First of all, we compare the results obtained with the GKBA master equation with the ones obtained with the two-times solution at the HF level. This comparison is shown in Fig. 5.11 for the case of a $N_x = 6,\ N_y = 6$ and $N_x = 10,\ N_y = 6$ CNTs. For this particular case, since the solution of the GKBA-HF master equation corresponds to the exact solution of the Dyson equation [2], we obtain a perfect agreement in both the current and the differential conductance. In the profile of the asymptotic currents, one can observe the emergence of two peaks around the energies of $V_g \approx \pm 1$ with respect to the center of the band, that are a clear signal of a high concentration of states in this energy interval. Indeed, as it is shown in Fig. 5.12 (left panel), the density of states $A(\omega) = \mathrm{Tr}\mathcal{A}(\omega)$ reveals the presence of two structures at these energies that can be identified as van Hove singularities [144]. Usually, when the gate voltage enters the window of the leads, the result is a net increase in the current flowing into or from the electronic reservoirs. Instead, as it is shown in the bottom panel of Fig. 5.11, the differential conductance is larger when the window of the leads encloses only the central part of the spectrum. This is due to the maximum variation of the injected number of particles in

[2] The many-body self-energy is treated at the same degree of approximation for both the dynamics and the spectrum.

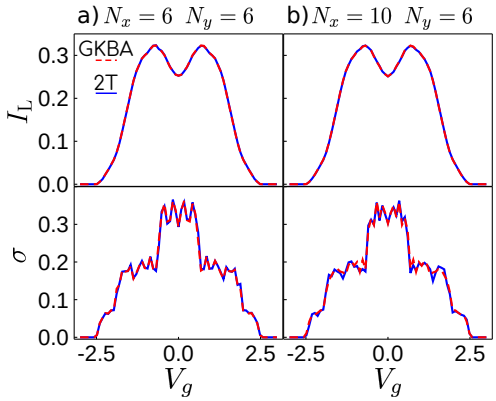

Figure 5.11: (Color online) Particle current in the left lead and conductance for a carbon nanotube with a) $N_x = 6$, $N_y = 6$, b) $N_x = 10$, $N_y = 6$ computed with the 2-times (solid blue) at stationarity and the GKBA-HF master equation (red dashed) with the exchange self-energy at the Hartee-Fock approximation.

the system at low energies. The last argument is understood from a closer inspection of the expression of the current in Eq. (5.18) together with the definition of the differential conductance. Indeed, in the formula for the current, one can recognize two terms that depend upon the bias, the lesser self-energy and the lesser Green's function of the central region. The variations of the lesser self-energy with the bias are very weak and result in a small shift of an otherwise constant function. The lesser Green's function is instead more sensible to the change in bias because it carries information on the density of particles which varies drastically as the bias is altered. Therefore, the larger broadening of the low energy states results in a considerable variation of the number of particles.

In Fig. 5.13, we show the asymptotic current and the differential conductance calculated by including the 2B self-energy for different system sizes. As we have observed in **V** for the one dimensional case, the GKBA predicts a larger resistance compare to the two-times solution. Nonetheless, both approaches agree on the reducing behavior of the current (top panels) with the length of the carbon nanotube. This fact is consistent with the common argument for which, in a non-interacting system, increasing of the characteristic length of the system reduces the scattering time and therefore brings to a reduction of the current. On the contrary, in the HF case discussed before, the current remains the same as the length of the system is increased and the transport continues to be fully ballistic. The differential conductance, displayed at the

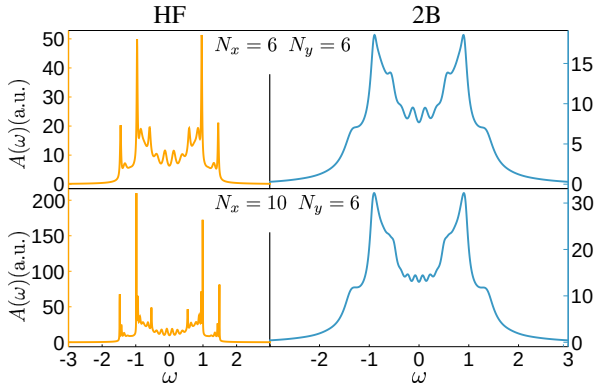

Figure 5.12: (Color online) Density of states, shifted by $U/2$, of a carbon nanotube computed with the 2-times approach at the HF level (left) and with the second-Born approximation (right). In the upper and lower panel, we display the results for $N_x = 6$, $N_y = 6$ and $N_x = 10$, $N_y = 6$ respectively.

bottom panels of Fig. 5.13, shows a much better mutual agreement between the GKBA-HF and the two-times solution, not only in a qualitative but also in a quantitative way. In particular, it is able to properly describe the interaction-induced broadening which is a consequence of the changes in the density of states of the system (shown in Fig. 5.12). Furthermore, the differential conductance decreases with the length of the CNT in agreement with the increase

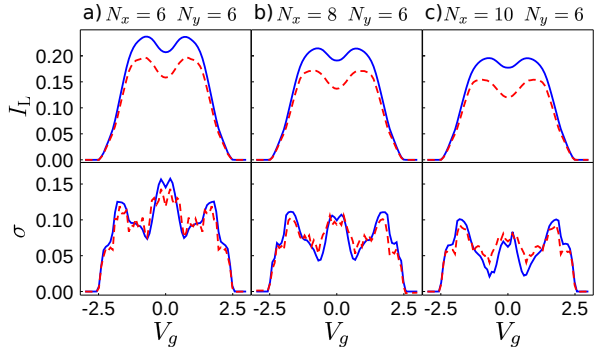

Figure 5.13: (Color online) Particle current in the left lead and conductance for a carbon nanotube with a) $N_x = 6$, $N_y = 6$, b) $N_x = 8$, $N_y = 6$, and c) $N_x = 10$, $N_y = 6$, computed with the 2-times (solid blue) at stationarity and the GKBA-HF master equation (red dashed) where the exchange self-energy is the Second Born one.

in the resistance discussed above. In addition to this, one can observe the emergence of a new interesting feature. As the length of the CNT increases, the central peak of the differential conductance decreases faster compared to the sided structures. Once again, this suggests that the main role of the observed effect is played by $G^<(\omega)$ which accounts for the change in the particle number of the system. Higher population at low energies will result in higher repulsive interactions that are responsible for the decrease of the differential conductance.
To summarize, by using the stationary current and the conductance as figures of merit, we were able to give numerical evidence that the GKBA is indeed able to capture spectral features, encoded in the lesser Green's function, that go beyond the HF propagator. This finding makes the GKBA, not only a valuable tool to describe transport phenomena in correlated many-body systems, but also a key method for the simulation and the description of ARPES and pump-probe experiments, where the central object for the reconstruction of the signal is exactly the lesser component of the Green's function. In addition it is worth to mention that, even if we have focused on the stationary state limit, the approach allows to study without difficulties also time-resolved transport in correlated quantum systems.

Concluding Remarks

In this thesis, we studied transport in correlated open quantum systems out-of-equilibrium by using many-body perturbation theory with non-equilibrium Green's functions. This approach requires a computational effort that exceeds the one of other many-body approaches. However, as proven also by the results of this thesis, it has great potential, thanks to its predictive power, and may become a broadly used tool in many fields of physics, including atomic and molecular physics, condensed-matter physics, nuclear matter, warm dense matter and cold atomic and molecular gases. Generally the use of Green's functions methods requires an in-depth understanding of the theory as well as of the different self-energy approximations used, and the development of reliable codes that efficiently solve the equations involved. My PhD research work focused on both the previous requirements with theory developments and a new numerical implementation. In Chapter 2, we introduced the transport problem in many-body systems together with a summary of the theoretical foundations of the many-body perturbation theory and Keldysh formalism. A large part of the discussion was related to the description of the characteristics of the equations of motion for the NEGF: the Keldysh–Kadanoff–Baym and Dyson equations. Moreover, there was a broad presentation of the different degrees of approximation in the theory.

We want to remind that Chapter 2 was not intended to be a complete and formal analysis of the topics presented, but rather its aim was to provide the Reader with a self-contained introduction to the basic tools necessary to better follow the rest of this doctoral work.

In Chapter 3, we presented the most useful physical quantities that the NEGF framework allows to extract for the description of the transport properties of a many-body system. Specifically, we discussed the derived time-dependent expression for the energy-current in a correlated open quantum system. The latter result is an analytical solutions that is a direct consequence of the equations of motion for the Green's function. With it we were able to predict secondary correlation effects that occur between pair of electronic reservoirs and which might influence their thermo-electric properties. This was mainly the content of publication **III** where we have also studied a simple model sys-

tem to discuss the consequences of our finding.
In Chapter 4, we focused on the details of the numerical implementation of the solution of the dynamical equations for the single-particle Green's function on the Keldysh contour. In particular, we highlighted the main steps to implement a self-consistent method based on the numerical *inversion* scheme on the full two-time plane, see publication **I**. We showed that, with a clever and well-designed layout for distributed-memory-parallel calculations, we were able to conceive a numerical code for large-scale simulations. This was possible because, during the numerical realization of the code, we took into account two key aspects: the minimization of the communication between the different processes and the significant fact that the operations needed for the self-energies calculations were sums over spatial (momentum) degrees of freedom. Furthermore, the several numerical routines that we developed, were collected into an open-source computational physics library that provides a simple and efficient framework for simulations of quantum many-body systems out-of-equilibrium, based on the Green's function formalism. As an additional comment, we want to recall that whenever a new approach is developed, it is not trivial to know a priori whether that approach is suitable for a specific problem or not. Accordingly, a large part of the implementation work was spent in testing, debugging and assessing the different type of approximations. Very often, this was done by studying very simple systems where comparisons with known results were possible. We found that such benchmarking is extremely important in this context, because it allows us to highlight the strengths and weaknesses of the implemented method.
Finally, in Chapter 5, we presented several effects and results, summarized in publications **I**−**V**, that characterize different transport setups and models including closed-interacting, open-non-interacting and open-interacting systems. We described how the time-dependent spreading of correlations in a system made of interacting particles loaded in quasi-crystalline structures is affected by a non-trivial interplay between the many-body interaction and the underlying energy landscape geometry. Then we tested the consequences of the expressions for the variation of energy in correlated open quantum systems and the effects of the second order lead-to-lead coupling that originates in an interacting single-level quantum dot junction in the Kondo regime. After that, we showed how to use the NEGF formalism to extract the electronic leads temperatures, which we have seen to match perfectly with a pioneering thermometry measurement performed on a gate-tunable single-quantum dot junction. Lastly, we presented the transport spectroscopy results that we have obtained within the stationary solution of the Generalized Kadanoff-Baym Ansatz master equation applied to a transport setup where the interacting region was taken to be either a one-dimensional quantum wire or a two-dimensional carbon nanotube. By using the stationary current and the

conductance as figures of merit, we were able to give numerical evidence that the GKBA is capable of capturing spectral features that by construction are not present in this approximate scheme of the theory.
In conclusion, we showed throughout this thesis that the non-equilibrium Green's function method offers a natural framework for the description of quantum transport. The work done constitutes developments of the time-dependent and steady-state description of many-body non-equilibrium quantum physics, with specialization to quantum transport phenomena. As future perspectives and developments, we plan to investigate the time-dependent description of physical scenarios that include electron-phonon interactions, excitonic-insulator phases and pump-probe processes. At the same time, our future motivations are guided by the will for improving the existing codes based on the NEGF formalism for a better scalability and faster computation.

Bibliography

[1] E. Schrödinger and R. Penrose, *What is Life?* (Cambridge University Press, 1992).

[2] J. K. Freericks, H. R. Krishnamurthy, and T. Pruschke, Phys. Rev. Lett. **102**, 136401 (2009).

[3] M. Eckstein and P. Werner, Phys. Rev. B **88**, 075135 (2013).

[4] M. Sentef, A. F. Kemper, B. Moritz, J. K. Freericks, Z.-X. Shen, and T. P. Devereaux, Phys. Rev. X **3**, 041033 (2013).

[5] M. Schüler, J. Berakdar, and Y. Pavlyukh, Phys. Rev. B **93**, 054303 (2016).

[6] S. Mor, M. Herzog, D. Golež, P. Werner, M. Eckstein, N. Katayama, M. Nohara, H. Takagi, T. Mizokawa, C. Monney, and J. Stähler, Phys. Rev. Lett. **119**, 086401 (2017).

[7] E. Perfetto, D. Sangalli, M. Palummo, A. Marini, and G. Stefanucci, Journal of Chemical Theory and Computation **15**, 4526 (2019).

[8] D. Fausti, R. I. Tobey, N. Dean, S. Kaiser, A. Dienst, M. C. Hoffmann, S. Pyon, T. Takayama, H. Takagi, and A. Cavalleri, Science **331**, 189 (2011).

[9] S. J. Denny, S. R. Clark, Y. Laplace, A. Cavalleri, and D. Jaksch, Phys. Rev. Lett. **114**, 137001 (2015).

[10] M. Mitrano, A. Cantaluppi, D. Nicoletti, S. Kaiser, A. Perucchi, S. Lupi, P. D. Pietro, D. Pontiroli, M. Riccò, S. R. Clark, D. Jaksch, and A. Cavalleri, Nature **530**, 461 (2016).

[11] D. Werdehausen, T. Takayama, M. Höppner, G. Albrecht, A. W. Rost, Y. Lu, D. Manske, H. Takagi, and S. Kaiser, Science Advances **4** (2018), 10.1126/sciadv.aap8652.

[12] A. Ronzani, B. Karimi, J. Senior, Y.-C. Chang, J. T. Peltonen, C. Chen, and J. P. Pekola, Nature Physics **14**, 991 (2018).

[13] B. Dutta, J. T. Peltonen, D. S. Antonenko, M. Meschke, M. A. Skvortsov, B. Kubala, J. König, C. B. Winkelmann, H. Courtois, and J. P. Pekola, Phys. Rev. Lett. **119**, 077701 (2017).

[14] B. Dutta, D. Majidi, A. García Corral, P. A. Erdman, S. Florens, T. A. Costi, H. Courtois, and C. B. Winkelmann, Nano Letters **19**, 506 (2019).

[15] A. Svilans, M. Josefsson, A. M. Burke, S. Fahlvik, C. Thelander, H. Linke, and M. Leijnse, Phys. Rev. Lett. **121**, 206801 (2018).

[16] G. Jaliel, R. K. Puddy, R. Sánchez, A. N. Jordan, B. Sothmann, I. Farrer, J. P. Griffiths, D. A. Ritchie, and C. G. Smith, Phys. Rev. Lett. **123**, 117701 (2019).

[17] M. Partanen, K. Y. Tan, S. Masuda, J. Govenius, R. E. Lake, M. Jenei, L. Grönberg, J. Hassel, S. Simbierowicz, V. Vesterinen, J. Tuorila, T. Ala-Nissila, and M. Möttönen, Scientific Reports **8** (2018), 10.1038/s41598-018-24449-1.

[18] F. Giazotto, T. T. Heikkilä, A. Luukanen, A. M. Savin, and J. P. Pekola, Rev. Mod. Phys. **78**, 217 (2006).

[19] J. P. Ronzheimer, M. Schreiber, S. Braun, S. S. Hodgman, S. Langer, I. P. McCulloch, F. Heidrich-Meisner, I. Bloch, and U. Schneider, Phys. Rev. Lett. **110**, 205301 (2013).

[20] U. Schneider, L. Hackermüller, J. P. Ronzheimer, S. Will, S. Braun, T. Best, I. Bloch, E. Demler, S. Mandt, D. Rasch, and A. Rosch, Nature Physics **8**, 213 (2012).

[21] A. Dirks, K. Mikelsons, H. R. Krishnamurthy, and J. K. Freericks, Phys. Rev. A **89**, 021602 (2014).

[22] D. Greif, L. Tarruell, T. Uehlinger, R. Jördens, and T. Esslinger, Phys. Rev. Lett. **106**, 145302 (2011).

[23] R. M. Noack, S. R. Manmana, A. Avella, and F. Mancini, AIP Conference Proceedings **789**, 93 (2005).

[24] P. Prelovšek and J. Bonča, in *Springer Series in Solid-State Sciences* (Springer Berlin Heidelberg, 2013) pp. 1–30.

[25] M. Rigol, V. Dunjko, and M. Olshanii, Nature **452**, 854 (2008).

[26] A. J. Daley, C. Kollath, U. Schollwöck, and G. Vidal, Journal of Statistical Mechanics: Theory and Experiment **2004**, P04005 (2004).

[27] G. Vidal, Phys. Rev. Lett. **93**, 040502 (2004).

[28] S. R. White and A. E. Feiguin, Phys. Rev. Lett. **93**, 076401 (2004).

[29] N. V. Prokof'ev and B. V. Svistunov, Phys. Rev. Lett. **81**, 2514 (1998).

[30] P. Werner, T. Oka, and A. J. Millis, Phys. Rev. B **79**, 035320 (2009).

[31] E. Kozik, K. V. Houcke, E. Gull, L. Pollet, N. Prokof'ev, B. Svistunov, and M. Troyer, EPL (Europhysics Letters) **90**, 10004 (2010).

[32] A. N. Rubtsov, V. V. Savkin, and A. I. Lichtenstein, Phys. Rev. B **72**, 035122 (2005).

[33] E. Gull, A. J. Millis, A. I. Lichtenstein, A. N. Rubtsov, M. Troyer, and P. Werner, Rev. Mod. Phys. **83**, 349 (2011).

[34] A. Akbari, M. J. Hashemi, A. Rubio, R. M. Nieminen, and R. van Leeuwen, Phys. Rev. B **85**, 235121 (2012).

[35] D. Lacroix, S. Hermanns, C. M. Hinz, and M. Bonitz, Phys. Rev. B **90**, 125112 (2014).

[36] S. Krönke and P. Schmelcher, Phys. Rev. A **98**, 013629 (2018).

[37] E. Runge and E. K. U. Gross, Phys. Rev. Lett. **52**, 997 (1984).

[38] M. Marques and E. Gross, Annual Review of Physical Chemistry **55**, 427 (2004), pMID: 15117259.

[39] G. Onida, L. Reining, and A. Rubio, Rev. Mod. Phys. **74**, 601 (2002).

[40] C. Verdozzi, D. Karlsson, M. P. von Friesen, C.-O. Almbladh, and U. von Barth, Chemical Physics **391**, 37 (2011).

[41] L. V. Keldysh, Sov. Phys. JETP **20**, 1018 (1965).

[42] L. Kadanoff and G. Baym, *Quantum statistical mechanics Green's function methods in equilibrium and nonequilibrium problems* (W.A. Benjamin, 1962).

[43] A. Stan, N. E. Dahlen, and R. van Leeuwen, The Journal of Chemical Physics **130**, 224101 (2009).

[44] K. Balzer, S. Bauch, and M. Bonitz, Phys. Rev. A **81**, 022510 (2010).

[45] H. S. Köhler, Phys. Rev. C **51**, 3232 (1995).

[46] H. S. Köhler, Journal of Physics: Conference Series **35**, 384 (2006).

[47] A. Rios, B. Barker, M. Buchler, and P. Danielewicz, Annals of Physics **326**, 1274 (2011).

[48] M. Garny and M. M. Müller, Phys. Rev. D **80**, 085011 (2009).

[49] M. Garny, A. Kartavtsev, and A. Hohenegger, Annals of Physics **328**, 26 (2013).

[50] M. Herranen, K. Kainulainen, and P. M. Rahkila, Journal of Physics: Conference Series **220**, 012007 (2010).

[51] M. Bonit, T. Bornath, D. Kremp, M. Schlanges, and W. D. Kraeft, Contributions to Plasma Physics **39**, 329 (1999).

[52] D. Kremp, T. Bornath, M. Bonitz, and M. Schlanges, Phys. Rev. E **60**, 4725 (1999).

[53] M. Lorke, T. R. Nielsen, J. Seebeck, P. Gartner, and F. Jahnke, Journal of Physics: Conference Series **35**, 182 (2006).

[54] H. Haug and A.-P. Jauho, *Quantum Kinetics in Transport and Optics of Semiconductors* (Springer, 2008).

[55] J. Rammer and H. Smith, Rev. Mod. Phys. **58**, 323 (1986).

[56] Y. Meir and N. S. Wingreen, Phys. Rev. Lett. **68**, 2512 (1992).

[57] G. Stefanucci and C.-O. Almbladh, Phys. Rev. B **69**, 195318 (2004).

[58] A.-P. Jauho, N. S. Wingreen, and Y. Meir, Phys. Rev. B **50**, 5528 (1994).

[59] K. Balzer and M. Bonitz, *Nonequilibrium Green's Functions Approach to Inhomogeneous Systems* (Springer, 2013).

[60] G. Stefanucci and R. van Leeuwen, *Nonequilibrium Many-Body Theory of Quantum Systems: A Modern Introduction* (Cambridge University Press, 2013).

[61] A. Fetter, J. Walecka, B. Banes, and M. Eakens, *Quantum Theory of Many-particle Systems* (McGraw-Hill, 1971).

[62] R. Mattuck, *A guide to Feynman diagrams in the many-body problem* (McGraw-Hill, 1976).

[63] G. Mahan, *Many-Particle Physics* (Springer US, 1990).

[64] E. Schrödinger, Phys. Rev. **28**, 1049 (1926).

[65] D. Griffiths and P. Griffiths, *Introduction to Quantum Mechanics* (Pearson Prentice Hall, 2005).

[66] P. A. M. Dirac, Proc. R. Soc. Lond. A **114**, 243–265 (1927).

[67] I. Bloch, J. Dalibard, and W. Zwerger, Rev. Mod. Phys. **80**, 885 (2008).

[68] D. C. Langreth, *Linear and Nonlinear Electron Transport in Solids*, edited by J. T. Devreese and V. E. van Doren (Springer US, Boston, MA, 1976) pp. 3–32.

[69] G. Baym and L. P. Kadanoff, Phys. Rev. **124**, 287 (1961).

[70] J. M. Luttinger and J. C. Ward, Phys. Rev. **118**, 1417 (1960).

[71] G. Baym, Phys. Rev. **127**, 1391 (1962).

[72] N. Schlünzen, S. Hermanns, M. Scharnke, and M. Bonitz, Journal of Physics: Condensed Matter **32**, 103001 (2019).

[73] P. Myöhänen, A. Stan, G. Stefanucci, and R. van Leeuwen, Phys. Rev. B **80**, 115107 (2009).

[74] P. Myöhänen, R. Tuovinen, T. Korhonen, G. Stefanucci, and R. van Leeuwen, Phys. Rev. B **85**, 075105 (2012).

[75] P. Lipavský, V. Špička, and B. Velický, Phys. Rev. B **34**, 6933 (1986).

[76] V. Špička, B. Velický, and A. Kalvová, Physica E: Low-dimensional Systems and Nanostructures **29**, 154 (2005), frontiers of Quantum.

[77] S. Hermanns, K. Balzer, and M. Bonitz, Physica Scripta **T151**, 014036 (2012).

[78] S. Hermanns, K. Balzer, and M. Bonitz, Journal of Physics: Conference Series **427**, 012008 (2013).

[79] K. Balzer, S. Hermanns, and M. Bonitz, Journal of Physics: Conference Series **427**, 012006 (2013).

[80] N. Schlünzen, J.-P. Joost, and M. Bonitz, Phys. Rev. Lett. **124**, 076601 (2020).

[81] J.-P. Joost, N. Schlünzen, and M. Bonitz, Phys. Rev. B **101**, 245101 (2020).

[82] D. Karlsson, R. van Leeuwen, Y. Pavlyukh, E. Perfetto, and G. Stefanucci, "Efficient non-equilibrium green's function simulations of correlated electron-boson systems," (2020), arXiv:2006.14965 [cond-mat.str-el] .

[83] D. Karlsson, R. van Leeuwen, E. Perfetto, and G. Stefanucci, Phys. Rev. B **98**, 115148 (2018).

[84] R. Tuovinen, D. Golež, M. Schüler, P. Werner, M. Eckstein, and M. A. Sentef, physica status solidi (b) **256**, 1800469 (2019).

[85] M. Hopjan and C. Verdozzi, The European Physical Journal Special Topics **227**, 1939 (2019).

[86] R. Tuovinen, R. van Leeuwen, E. Perfetto, and G. Stefanucci, Journal of Physics: Conference Series **427**, 012014 (2013).

[87] R. Landauer, IBM Journal of Research and Development **1**, 223 (1957).

[88] M. Büttiker, Phys. Rev. Lett. **57**, 1761 (1986).

[89] M. Galperin, A. Nitzan, and M. A. Ratner, Phys. Rev. B **75**, 155312 (2007).

[90] T. A. Costi and V. Zlatić, Phys. Rev. B **81**, 235127 (2010).

[91] T.-S. Kim and S. Hershfield, Phys. Rev. Lett. **88**, 136601 (2002).

[92] B. Dong and X. L. Lei, Journal of Physics: Condensed Matter **14**, 11747 (2002).

[93] Y. Gao and M. Galperin, The Journal of Chemical Physics **144**, 174113 (2016).

[94] S. Mukamel and M. Galperin, The Journal of Physical Chemistry C **123**, 29015–29023 (2019).

[95] M. F. Ludovico, L. Arrachea, M. Moskalets, and D. Sánchez, Entropy **18** (2016), 10.3390/e18110419.

[96] N. Lo Gullo and N. W. Talarico, GitLab repository (2019).

[97] N. Lo Gullo and N. W. Talarico, GitLab repository (2019).

[98] W. Press, S. Teukolsky, W. Vetterling, and B. Flannery, *Numerical Recipes 3rd Edition: The Art of Scientific Computing* (Cambridge University Press, 2007).

[99] P. Pulay, Chemical Physics Letters **73**, 393 (1980).

[100] K. S. Thygesen and A. Rubio, Phys. Rev. B **77**, 115333 (2008).

[101] D. Karlsson, *Analytical and Numerical Developments in Strongly Correlated Systems: Perspectives from TDDFT and Green's Functions*, Ph.D. thesis, Lund University (2014).

[102] N. Lo Gullo and L. Dell'Anna, Phys. Rev. B **94**, 184308 (2016).

[103] D. Shechtman, I. Blech, D. Gratias, and J. W. Cahn, Phys. Rev. Lett. **53**, 1951 (1984).

[104] A.-P. Tsai, A. Inoue, and T. Masumoto, Japanese Journal of Applied Physics **26**, L1505 (1987).

[105] J.-M. Dubois, *Useful Quasicrystals* (WORLD SCIENTIFIC, 2005).

[106] P. Steinhardt, Rend. Fis. Acc. Lincei **24**, 85–91 (2013).

[107] J. X. Zhong and R. Mosseri, Journal of Physics: Condensed Matter **7**, 8383 (1995).

[108] S. Roche, G. Trambly de Laissardière, and D. Mayou, Journal of Mathematical Physics **38**, 1794 (1997).

[109] R. Ketzmerick, G. Petschel, and T. Geisel, Phys. Rev. Lett. **69**, 695 (1992).

[110] N. Lo Gullo, C. V. Ambarish, T. Busch, L. Dell'Anna, and C. M. Chandrashekar, Phys. Rev. E **96**, 012111 (2017).

[111] S. Y. Jitomirskaya, Annals of Mathematics **150**, 1159 (1999).

[112] A. Avila and S. Jitomirskaya, Lecture Notes in Physics , 5–16 (2006).

[113] A. Avila and S. Jitomirskaya, Annals of Mathematics **170**, 303 (2009).

[114] L. Tanzi, E. Lucioni, S. Chaudhuri, L. Gori, A. Kumar, C. D'Errico, M. Inguscio, and G. Modugno, Phys. Rev. Lett. **111**, 115301 (2013).

[115] M. Schreiber, S. S. Hodgman, P. Bordia, H. P. Lüschen, M. H. Fischer, R. Vosk, E. Altman, U. Schneider, and I. Bloch, Science **349**, 842 (2015).

[116] H. P. Lüschen, P. Bordia, S. Scherg, F. Alet, E. Altman, U. Schneider, and I. Bloch, Phys. Rev. Lett. **119**, 260401 (2017).

[117] H. HIRAMOTO and M. KOHMOTO, International Journal of Modern Physics B **06**, 281 (1992).

[118] E. H. Lieb and D. W. Robinson, Commun. Math. Phys **28**, 251–257 (1972).

[119] A. Sütő, J. Stat. Phys. **56**, 525–531 (1989).

[120] N. Lo Gullo, L. Vittadello, M. Bazzan, and L. Dell'Anna, Phys. Rev. A **94**, 023846 (2016).

[121] N. L. Gullo, L. Vittadello, L. Dell'Anna, M. Merano, N. Rossetto, and M. Bazzan, Journal of Optics **19**, 055613 (2017).

[122] J. M. Luck, Phys. Rev. B **39**, 5834 (1989).

[123] M. Queffélec, *Substitution Dynamical Systems - Spectral Analysis* (Springer-Verlag Berlin Heidelberg, 2010).

[124] M. Reed and B. Simon, *III: Scattering Theory*, Methods of Modern Mathematical Physics (Elsevier Science, 1979).

[125] W. Amrein, *Non-Relativistic Quantum Dynamics*, Mathematical Physics Studies (Springer Netherlands, 1981).

[126] A. S. Pikovsky, M. A. Zaks, U. Feudel, and J. Kurths, Phys. Rev. E **52**, 285 (1995).

[127] Y. Last, Journal of Functional Analysis **142**, 406 (1996).

[128] P. W. Anderson, Phys. Rev. **124**, 41 (1961).

[129] F. D. M. Haldane, Phys. Rev. Lett. **40**, 416 (1978).

[130] A. C. Hewson, *The Kondo Problem to Heavy Fermions*, Cambridge Studies in Magnetism (Cambridge University Press, 1993).

[131] L. Kouwenhoven and L. Glazman, Physics World **14**, 33 (2001).

[132] H. Li, B. K. Agarwalla, and J.-S. Wang, Phys. Rev. E **86**, 011141 (2012).

[133] A. Levy, L. Kidon, J. Bätge, J. Okamoto, M. Thoss, D. T. Limmer, and E. Rabani, The Journal of Physical Chemistry C **123**, 13538 (2019).

[134] J.-S. Wang, B. K. Agarwalla, H. Li, and J. Thingna, Frontiers of Physics **9**, 673–697 (2014).

[135] L. A. Zotti, M. Bürkle, F. Pauly, W. Lee, K. Kim, W. Jeong, Y. Asai, P. Reddy, and J. C. Cuevas, New Journal of Physics **16**, 015004 (2014).

[136] E. Pop, Nano Research **3**, 147 (2010).

[137] W. Lee, K. Kim, W. Jeong, L. A. Zotti, F. Pauly, J. C. Cuevas, and P. Reddy, Nature **498**, 209 (2013).

[138] Y. Dubi and M. Di Ventra, Rev. Mod. Phys. **83**, 131 (2011).

[139] L. Wang and B. Li, Phys. Rev. Lett. **99**, 177208 (2007).

[140] C. Kathmann, M. Reina, R. Messina, P. Ben-Abdallah, and S.-A. Biehs, Scientific Reports **10** (2020), 10.1038/s41598-020-60603-4.

[141] L. P. Kouwenhoven, D. G. Austing, and S. Tarucha, Reports on Progress in Physics **64**, 701 (2001).

[142] S. Iijima, Nature **354**, 56 (1991).

[143] K. S. Novoselov, A. K. Geim, S. V. Morozov, D. Jiang, M. I. Katsnelson, I. V. Grigorieva, S. V. Dubonos, and A. A. Firsov, Nature **438**, 197 (2005).

[144] A. H. Castro Neto, F. Guinea, N. M. R. Peres, K. S. Novoselov, and A. K. Geim, Rev. Mod. Phys. **81**, 109 (2009).

UNIVERSITY OF TURKU

Painosalama Oy, Turku, Finland 2021

ISBN 978-951-29-8313-1 (PRINT)
ISBN 978-951-29-8313-1 (PDF)
ISSN 0082-7002 (Print)
ISSN 2343-3175 (Online)